5-12-2024

Investigating Holography using Classical and Quantum Simulations

Goksu Can Toga
Syracuse University

Abstract

In this thesis, we aim to develop classical and quantum simulations to test holography. Holography can be thought of in its most basic form as a duality that relates a $d+1$ dimensional theory to a d dimensional one and the most famous holographic correspondence is the AdS/CFT duality where $d+1$ dimensional weakly coupled gravity theory is related to a d dimensional CFT.

We start by developing lattice simulations for the $\mathcal{N}=4$ super Yang-Mills model and explore an improved supersymmetric lattice action showing that it is free of the lattice artifacts that plagued earlier lattice theories. We use it to calculate supersymmetric Wilson loops and the non-Abelian Coulomb potential using Polyakov line correlators. For both of these observables, we demonstrate the excellent agreement between lattice results and analytical results obtained from the holographic dual. This constitutes a very non-trivial check for the AdS/CFT correspondence using non-perturbative classical simulation methods.

In the latter part of this thesis, we extend these ideas to quantum simulations for a simpler class of model the transverse Ising Model living in an AdS_2 space. We obtain the ground state of this model and explore the phase structure of the theory using the Density Matrix Renormalization Group (DMRG) . We then obtain the time-evolution of this system using both classical methods such as Time Evolving Block Decimation (TEBD) and usual quantum simulation techniques. The most interesting aspects of this model appear when we calculate the out-of-time-ordered correlators (OTOCs) to investigate the information propagation and scrambling in this model. We find a region where these OTOCs have a logarithmic dependence on the number of degrees of freedom of the system. This behavior has only been seen previously for models that are all to all or have infinite or long-range interactions. Yet our simple model with only nearest-neighbor interactions manages to capture this behavior.

This makes this model a very interesting candidate to study information propagation and scrambling using quantum simulations.

Investigating Holography using Classical and Quantum Simulations

by

Goksu Can Toga

B.Sc., Middle East Technical University, 2015

M.Sc., Middle East Technical University, 2018

DISSERTATION

Submitted in partial fulfillment of the requirements for the degree of

Doctor of Philosophy in Physics

Syracuse University

May 2024

To my family

Acknowledgements

I am deeply grateful to my advisor, Simon Catterall, whose unwavering support, invaluable guidance, and mentorship have been pivotal throughout the course of this thesis. His profound expertise, encouragement, and insightful feedback have not only shaped the trajectory of this work but also steered me through the complexities of research and taught me how the become a better researcher.

I'd also like to thank, Yannick Meurice, whose profound knowledge in physics and quantum computing, coupled with his mentorship, significantly contributed to the completion of this thesis. His unwavering support has been indispensable and greatly appreciated.

I extend my sincere thanks to the members of my thesis committee, William Wylie, Jay Hubisz, and Jack Laiho, for their invaluable insights and constructive feedback, which have enriched the quality of this research.

To my friends, both within and beyond the physics department – Maxx, Tianna, Louis, Bharath, Julia, Pat, Chaitanya, Asad, Brad, Joe, Alex, and Jake – I owe a debt of gratitude for their unwavering encouragement, support, and camaraderie throughout this journey.

Lastly, I am profoundly indebted to my family for their unconditional love, encouragement, and understanding. To my parents, Necla and Huseyin, whose unwavering support sustained me through the challenges of my PhD journey, even amidst their own difficulties – I am forever grateful. To my grandparents, Esef and Zehra, whose wisdom and guidance have been foundational to my upbringing, I owe a debt of gratitude that words cannot express. My brother, Gokay, deserves special mention for his unwavering belief in me and constant motivation. And to my partner, Georgia, whose unwavering support and understanding have been my anchor through every storm.

List of Papers

Chapters 2, 3, 4 of the dissertation are comprised of the work carried out in the following papers.

1. **Lattice $\mathcal{N} = 4$ super Yang-Mills at strong coupling**; Simon Catterall, Joel Giedt, Goksu Can Toga ; JHEP 12 (2020) 140
   https://link.springer.com/article/10.1007/JHEP12(2020)140

2. **Holography from lattice $\mathcal{N} = 4$ super Yang-Mills;** Simon Catterall, Joel Giedt, Goksu Can Toga; JHEP 08 (2023) 084
   https://link.springer.com/article/10.1007/JHEP08(2023)084

3. **Quantum Ising model on two dimensional anti-de Sitter space;** Muhammad Asaduzzaman, Simon Catterall, Yannick Meurice, Goksu Can Toga; Phys.Rev.D. 109 (2024) 5, 054513
   https://link.aps.org/doi/10.1103/PhysRevD.109.054513

The following research publications have not been included in the thesis due to their disjoint research field to the main theme of the dissertation work:

1. **Simulating Field Theories with Quantum Computers ;** Muhammad Asaduzzaman, Simon Catterall, Yannick Meurice, Goksu Can Toga; ArXiv: 2401.01962 [quant-ph] (PoS Lattice 2023)
   https://arxiv.org/abs/2401.01962
2. **Tensor network representation of non-abelian gauge theory coupled to reduced staggered fermions** Muhammad Asaduzzaman; Simon Catterall; Goksu Can Toga; Yannick Meurice; Ryo Sakai; arXiv:2312.16167 [hep-lat] (2023)
   https://arxiv.org/abs/2312.16167

3. **Improved coarse-graining methods for two dimensional tensor networks including fermions** Muhammad Asaduzzaman, Simon Catterall, Goksu Can Toga, Yannick Meurice, Ryo Sakai; JHEP 01 (2023) 024
   https://link.springer.com/article/10.1007/JHEP01(2023)024
4. **Quantum Simulation of the N flavor Gross-Neveu Model** Muhammad Asaduzzaman, Simon Catterall, Yannick Meurice, Goksu Can Toga, Ryo Sakai; Phys.Rev.D. 106 (2022) 11, 114515
   https://journals.aps.org/prd/abstract/10.1103/PhysRevD.106.114515
5. **Symmetric Mass Generation in Lattice Gauge Theory;** Nouman Butt, Simon Catterall, Goksu Can Toga; Symmetry 13 (2021) 12, 2276
   https://www.mdpi.com/2073-8994/13/12/2276
6. **Anomalies and symmetric mass generation for Kähler-Dirac fermions;** Nouman Butt, Simon Catterall, Arnab Pradhan, Goksu Can Toga; Phys.Rev.D. 104 (2021) 9, 094504
   https://journals.aps.org/prd/abstract/10.1103/PhysRevD.104.094504

Contents

List of Figures

List of Tables

Chapter 1

Introduction

Holography and the AdS/CFT correspondence have been one of the most attractive and well-studied topic in high-energy physics in the last couple of decades.[1–3] This correspondence in its most basic form relates a strongly coupled critical system that lives in d-dimensions to a gravitational theory that lives in $d+1$-dimensions. This very powerful duality has allowed us to calculate observables in these theories that were previously inaccessible by relating the strongly coupled gauge theory to a weakly interacting essentially classical gravity theory where the calculations are tractable. However, one big caveat of AdS/CFT is that it has only been tested and used in the large N, strong coupling limit where the dual theory is a classical gravitational system. This hinders our ability to deeply understand the nature of this duality and use it to predict quantum gravity effects. So the question is, is there a way to understand this duality outside of this regime? One of the classical approaches to understanding nonperturbative regimes of high-energy physics models is to develop lattice-regularized versions of these models and study them via lattice simulations [4]. This approach has been very successful in probing the phase diagram of many gauge theories including QCD [5–8]. And naturally many lattice gauge theorists have tried to implement a similar approach to study holography and AdS/CFT [9–11]. However, there were major obstacles mainly because lattice discretization breaks Poincare invariance which is essential to preserve

supersymmetry. There have been many attempts to solve these problems but we will focus on the approach of using twisted symmetries or orbifolding which has been developed by Simon Catterall, David Kaplan, and Mithat Unsal [12] in this thesis. This approach made the lattice simulation of supersymmetric models possible. However, there were still considerable obstacles to connecting with the holographic results specifically those that have been derived for $\mathcal{N} = 4$ SYM model which is dual to a $AdS_5 \times S_5$ gravitational theory. In this thesis, we will show how these problems are solved with the inclusion of a new term in the action [13, 14].

Another way one could use to study non-perturbative physics is to use a Hamiltonian approach instead of an Euclidean lattice regularization. One main advantage of this approach is that it makes it possible to use tensor network and quantum computing approaches to study these models. Also, using tensor network and quantum computing methods makes real time dynamical simulations of these models possible. Which then can be used to study the time dependent properties of these models. [15–20]

In this thesis, we will use both of these approaches to study holography using simulations. First, we will start with investigating one of the most famous models that exhibit AdS/CFT duality which is the $\mathcal{N} = 4$ super Yang-Mills (SYM) model using lattice simulations. We will show that with the inclusion of a new term in the lattice action we were successful in simulating the theory up to arbitrarily large values of its coupling. We then show the excellent agreement between analytical calculations that were done for supersymmetric Wilson Loops and the non-Abelian coulomb potential of the $\mathcal{N} = 4$ SYM model and the lattice results. These results constitute a very non-trivial check of holography obtained through nonperturbative methods.

In the latter part of this thesis, we will focus on the Hamiltonian simulation of an Ising chain that lives in the discretization of an AdS_2 space using Tensor Network methods and quantum computers. This Ising model is another model that exhibits holographic duality. We will obtain the ground state and do dynamical simulations to investigate the information

propagation and scrambling in the context of this model. We will show that this model can propagate information in a time that depends only logarithmically on the number of degrees of freedom which puts it in a class of models that are called fast scramblers. The most interesting aspect of this classification is that all the other models that exhibit such properties are either all-to-all models like the SYK model or models that have infinite or very long-range interactions. Our simple model with only nearest-neighbor interactions captures that behavior which makes this a very interesting model to study further.

Before moving on with discussing our results, we will introduce the major concepts and techniques that establish the basis of this thesis.

1.1 AdS/CFT Correspondence

AdS/CFT correspondence or the gauge/gravity duality was conjectured by Maldacena in 1997 [21]. Ever since then, it has had a great impact on various fields of physics including condensed matter, nuclear physics, and quantum information theory. In this section, we will introduce the basic concepts of this duality.

While Maldacana's initial conjecture was rooted in string theory however it's also possible to motivate this duality independent of string theory. After a brief review of Maldacana's original construction, we will also motivate this duality independent of the string theory. The starting point of this duality from the string theory perspective was to develop a description of D1-D5 brane unraveling in terms of D3-branes. D-branes are extended objects in string theory where strings have their end points. The development of D-branes played a crucial role in many of the successes of string theory. One can start by considering N coincident D3-branes which have two distinct asymptotic regions, first at weak coupling $g_s N \ll 1$ these branes exists on a flat 10-dimensional space-time, secondly in the strong coupling limit of this system where $g_s N \gg 1$ these branes describe a highly curved spacetime [22]. Maldacena's brilliant insight was to consider a theory where the gravity is decoupled on the branes which

can be achieved by taking a low-energy limit. This results in the following, a 4-dimensional $SU(N)$ super Yang-Mills (SYM) model that describes the dynamics of the branes and a near horizon geometry that is described by an $AdS_5 \times S^5$ for the 10-dimensional models.

Then the low energy sector of the initial D3 brane construction can be described by the 4-dimensional $SU(N)$ SYM model for weak coupling and the 10-dimensional string theory in $AdS_5 \times S^5$. And by using the fact that gauge theories are well-defined for any value of the coupling one can generalize this correspondence even for the strong coupling limit. This leads to the famous conjecture that is known as the AdS/CFT duality,

$$\text{String theory on } AdS_5 \times S^5 \simeq \mathcal{N} = 4 \ SU(N) \text{ gauge theory in } 4D \tag{1.1}$$

This correspondence also established how to relate the parameters on both sides of this duality. For the gauge theory side, we have the following couplings, the Yang-Mills coupling g_{ym} and the rank of the gauge group N and on the string theory side, we have the curvature scale ℓ/ℓ_s and the string coupling g_s. These couplings can be related in the following way,

$$4\pi g_s = g_{ym}^2 \sim \frac{\lambda}{N} \tag{1.2}$$

$$\frac{\ell}{\ell_s} = (4\pi g_s N)^{\frac{1}{4}} \sim \lambda^{\frac{1}{4}} \tag{1.3}$$

An alternative way to establish this correspondence one can start by thinking about relating a gauge theory to a gravitational theory through their matter content. Such a relation can be obtained by considering the spin two graviton that arises as a composite of two spin one gauge bosons. Usually, this would be impossible due to the famous no-go theorem of Weinberg and Witten [23], however, one can get around that by using the holographic principle and allowing the graviton to propagate in higher dimensions. Then this gauge theory consists of a graviton in addition to an extra dimension.

The next step in our construction for the gauge/gravity duality is to ensure that this extra

dimension can be macroscopic. To achieve that we start by noticing the complete dissimilarity between a perturbative gauge theory and classical gravity which forces us to consider that the gauge theory should be strongly coupled to reproduce gravity. This naturally leads us to consider a gauge theory where we can have a coupling that remains strong over various ranges of energies and a natural candidate for such a gauge theory is to consider a conformal field theory where the coupling doesn't run. However, there is still a discrepancy between the number of degrees of freedom between the two sides of this correspondence. To solve this one can consider a gauge theory that consists of a large number of degrees of freedom meaning a large gauge group like $SU(N)$ where $N \to \infty$.

Then we can introduce supersymmetry in this strongly coupled gauge theory to keep it under control. The natural choice for the set of supersymmetric operators is to use $\mathcal{N} = 4$ which is the most supersymmetric case and it also ensures that the theory is invariant under confromal transformations. Imposing these choices leads us to the 4-dimensional $\mathcal{N} = 4$ $SU(N)$ SYM theory. This theory has the following symmetries when formulated on a Minkowski space. First, the vacuum is invariant under Poincare transformations, specifically, it is invariant under rigid scale transformations $x^\mu \to \alpha x^\mu$. This transformation also rescales the energy as $E \to E/\alpha$. Then one can identify the extra dimension by the inverse energy and write down the most general metric that is consistent with the symmetries identified above which results in the 5-dimensional metric of AdS_5,

$$ds^2 = \frac{\ell^2}{z^2}(\eta_{\mu\nu}dx^\mu dx^\nu + dz^2) \tag{1.4}$$

where z is the extra dimension that was identified with the inverse energy. This shows us that we can relate a 4-dimensional $\mathcal{N} = 4$ $SU(N)$ SYM theory to a theory of gravity on 5-dimensional AdS provided that the number of colors N related to the size of AdS ℓ. However, it is also possible to take this relation even further by matching the supersymmetric content of the gauge theory to the gravity side by extending the gravity to a supergravity theory. This extension to the supergravity is naturally formulated in 10-dimensions with

$AdS_5 \times S^5$ as its solution. Then the additional extra dimensions can be identified with the scalars of the SYM model. This brings us into a full circle where we identify the $\mathcal{N} = 4$ $SU(N)$ model with a gravity theory on $AdS_5 \times S^5$ [24, 25] .

We will conclude this section by pointing out some key properties of the AdS/CFT duality,

1. AdS/CFT duality is a duality between a strong and a weak coupling. This allows us to study gauge theories in the strong coupling limit even though perturbation theory fails by employing the fact that it is dual to a weakly coupled gravitational theory.
2. AdS/CFT has a holographic nature. This means that it relates a theory that lives in higher dimensions to a lower one.
3. Finally, AdS/CFT duality is a mapping between a regular quantum field theory to a quantum theory of gravity.

With this we conclude our brief introduction into AdS/CFT correspondence in the next two sections we will introduce the two sides of this duality namely the $\mathcal{N} = 4$ SYM model and the AdS space further.

1.2 Brief introduction to $\mathcal{N} = 4$ SYM

In this section, we will introduce the $\mathcal{N} = 4$ super Yang-Mills model further.

$\mathcal{N} = 4$ SYM theory in 4 dimensions is one of the most well-studied supersymmetric models in physics. It can be obtained through dimensional reduction of $d = 10$ $\mathcal{N} = 1$ SYM model to 4 dimensions [26]. One of the most interesting and useful properties of this model is that it possesses a coupling constant that doesn't run. It is conformal. And finally, it has maximal symmetry in four dimensions.

The field content of this model consists of 16 fermions that live in the adjoint representation of the $SU(N)$ gauge group and 6 scalars. It also possesses a $SO(6)$ R-symmetry. The symmetry group of this model which includes supersymmetry and conformal transformations

can be denoted as the $SU(2,2|4)$ and is known as the superconformal group.

Now let's investigate the dimensional reduction from $d = 10$ back to $d = 4$ a little bit more in detail. The $\mathcal{N} = 1, d = 10$ theory has the following action,

$$S_{\mathcal{N}=1} = \frac{1}{g^2} \int d^{10}x \, \mathrm{Tr} \left(-\frac{1}{4} F_{MN} F^{MN} + \frac{i}{2} \Psi \not{D} \Psi \right) \tag{1.5}$$

Where the Ψ_b are the Majorana-Weyl spinors and b ranges between $1 - 16$. And F_{MN} denotes the usual field strength tensor. They are both valued in the adjoint representation of the gauge group. Finally, $\not{D} = \Gamma D$ is the Dirac operator, and its action on fermions can be given as,

$$(D_\mu \Psi)^a = \partial_\mu \Psi^a + g f^a_{bc} A^b_\mu \Psi^c \tag{1.6}$$

The set of supersymmetric transformations that leave the action 1.5 invariant can be given by,

$$\delta_\epsilon \Psi^a = -\epsilon \frac{1}{4} F^a_{\mu\nu} \Gamma^{\mu\nu} \tag{1.7}$$

$$\delta_\epsilon \Psi^a = \bar{\epsilon} \frac{1}{4} F^a_{\mu\nu} \Gamma^{\mu\nu} \tag{1.8}$$

$$\delta_\epsilon A^a_\mu = \bar{\epsilon} \frac{i}{2} \Gamma_\mu \Psi^a \tag{1.9}$$

The fact that the bosonic and fermionic degrees of freedom match can be realized by observing that in dimensions d where $d \bmod 8 = 2$ it is possible to have a Majorana-Weyl representation for the fermions by imposing the Majorana-Weyl condition which reduces the 32 complex components of fermions to 16 components which matches the number of degrees of freedom of the bosonic sector.

We can dimensionally reduce this theory from ten dimensions to four by compactifying the 6 extra dimensions. Then the gauge degrees of freedom from these compactified directions

behaves as scalars X_i where i ranges between 1 to 6. Using these scalars we can write the new field strength tensor that can be decomposed as

$$F_{AB} = -i\,[X_A, X_B] \tag{1.10}$$

$$F_{\mu A} = \partial_\mu X_A - i\,[A_\mu, X_A] = D_\mu X_A \tag{1.11}$$

$$F_{\mu\nu} = \partial_\mu A_\nu - \partial_\nu A_\mu - i\,[A_\mu, A_\nu] \tag{1.12}$$

Following the same fashion we can write the kinetic term in this dimensionally reduced space as

$$-\frac{1}{4}F_{MN}F^{MN} = \frac{-1}{4}F_{\mu\nu}F^{\mu\nu} + \frac{1}{2}\sum_I (D_\mu X_I)^2 - \frac{1}{4}\sum_{A.B}[X_A, X_B]^2 \tag{1.13}$$

and the fermionic content of the action can be written as

$$\frac{i}{2}\Psi^m \not{D}\Psi_m = \frac{i}{2}\Psi^\mu \not{D}\Psi_\mu + \frac{1}{2}\Psi\Gamma^A\,[X_A, \Psi] \tag{1.14}$$

This concludes the field content of the dimensionally reduced action to 4 dimensions.

We should also mention one of the properties of $\mathcal{N} = 4$ SYM model explicitly. Due to the commutation relations of the scalars X_i where $[X_i, X_j] = 0$, $\mathcal{N} = 4$ SYM model has flat directions which leads to a moduli space of vacuum solutions. This leads to only the adjoint scalars of $\mathcal{N} = 4$ getting a vacuum expectation value (vev) while breaking the gauge symmetry to $U(1)$. We will show in the following sections that controlling these flat directions is essential in obtaining reliable simulations of this model on the lattice.

1.3 Review of Anti-de Sitter Spaces

Anti-de Sitter (AdS) spacetimes are the maximally symmetric solutions of the Einstein equations with a negative cosmological constant [27, 28].

$$S = \frac{1}{16\pi G} \int d^d x \sqrt{-g}(R - 2\Lambda) \tag{1.15}$$

For different choices of Λ, we can obtain different asymptotic characteristics for the solutions of this model.

- $\Lambda = 0$ gives asymptotically flat solutions
- $\Lambda > 0$ gives asymptotically de-Sitter(dS) solutions
- $\Lambda < 0$ gives the desired AdS solution.

After varying this equation with respect to the metric we get the following solution

$$\mathcal{R}_{\mu\nu} - \frac{g_{\mu\nu}}{2}\mathcal{R} = -\frac{\Lambda}{2} g_{\mu\nu} \tag{1.16}$$

For $d = 5$ Ricci Tensor $\mathcal{R} = \frac{5}{3}\Lambda$ is proportional to the metric and can be given as,

$$\mathcal{R}_{\mu\nu} = \frac{\Lambda}{3} g_{\mu\nu} \tag{1.17}$$

If we impose a further restriction in the form of

$$\mathcal{R}_{\mu\nu\tau\rho} = \frac{\Lambda}{12} \left(g_{\mu\tau} g_{\hat{\rho}} - g_{\mu\rho} g_{\nu\tau} \right) \tag{1.18}$$

We can obtain a maximally symmetric space as the solution for these equations. For the Minkowski signature corresponds to AdS_5 and for the Euclidean signature this gives a Hyperbolic space H^5 given that $\Lambda < 0$.

Then these can be embedded in a flat space to further investigate their properties,

$$X_A X^A \equiv X_0^2 + X_{d+1}^2 - \sum_{i=1}^{d} X_i^2 = R^2 \tag{1.19}$$

A very useful set of coordinates for this embedding can be given for the case of AdS_5 as,

$$x_i = R\sinh(\rho)\hat{x}_i, \sum_{i=1}^{4}\hat{x}_i^2 = 1 \tag{1.20}$$

$$x_0 = R\cosh(\rho)\cos(\tau) \tag{1.21}$$

$$x_5 = R\cosh(\rho)\sin(\tau) \tag{1.22}$$

The metric that corresponds to this choice of coordinates is given as

$$ds^2 = R^2\left(-\cosh^2(\rho)d\tau^2 + d\rho^2 + \sinh^2(\rho)d\Omega_3\right) \tag{1.23}$$

Following the same procedure above for AdS_3 we can also obtain the metric that is of interest in Chapter 4 which has a very similar form to Eq. 1.23.

Before concluding the section we want to point out some of the symmetry properties of the AdS_5 the isometry group of AdS_5 is $SO(2,4)$ which is the conformal group in four dimensions which was a cornerstone in the AdS/CFT correspondence.

1.4 Lattice Construction of $\mathcal{N} = 4$ SYM

In this section, we will review the lattice construction of the $\mathcal{N} = 4$ SYM model [12]. As we have stated in the introduction many attempts at constructing the lattice formulation of supersymmetric theories have run into the problem that naive discretization of spacetime doesn't preserve Poincare algebra. So let's start our discussion by explicitly writing the Poincare transformations.

The Poincare transformations can be thought of as the combination of Lorentz transformations and translations. Its algebra can be given by the following,

$$[P^\mu, P^\nu] = 0, \tag{1.24}$$

$$[M^{\mu\nu}, P^\rho] = i\left(P^\mu \eta^{\nu\rho} - P^\nu \eta^{\mu\rho}\right) \tag{1.25}$$

$$[M^{\mu\nu}, M^{\rho\sigma}] = i\left(M^{\mu\sigma}\eta^{\nu\rho} + M^{\nu\rho}\eta^{\mu\sigma} - M^{\mu\rho}\eta^{\nu\sigma} - M^{\nu\sigma}\eta^{\mu\rho}\right) \tag{1.26}$$

Where P denotes the generators for the translations and M are the anti-symmetric generators for the Lorentz group. Further, if we impose supersymmetry in our model the Poincare generators P and M become bosonic generators of the new supersymmetry algebra with the inclusion of new fermionic generators Q and $\bar{Q}$ then the new commutation relations for the susy algebra can be given as

$$[P, Q] = 0 \tag{1.27}$$

$$\left\{Q^L_\alpha, Q^M_\beta\right\} = \epsilon_{\alpha\beta} Z^{LM} \tag{1.28}$$

$$\left[Q^L_\alpha, M_{\mu\nu}\right] = \frac{1}{2}(\sigma_{\mu\nu})^\beta_\alpha Q^L_\beta \tag{1.29}$$

$$\left\{Q^L_\alpha, \bar{Q}^M_\beta\right\} = \delta^{LM}\sigma^\mu_{\alpha\beta} P_\mu \tag{1.30}$$

Where the new indices L, M denotes the number of supercharges $\mathcal{N}$ and they range from $L, M = 1, 2, \ldots \mathcal{N}$. Let's focus on the last commutation relation of two supersymmetry transformations looking at this anti-commutation relation it's easy to see that the combination of these two transformations corresponds to an infinitesimal space-time translation. Which is broken under lattice discretization meaning that any naive discretization will not preserve the supersymmetry algebra.

The first step in getting around this major obstacle in obtaining a discretization of $\mathcal{N} = 4$ SYM model is to start with a twisted version of the theory instead of the usual version. The initial idea of twisted models was proposed by Witten in the 1980s and it has very close

connections to topology [29]. The main idea is to relate a topological field theory to a supersymmetric one. This twisting procedure can be viewed as the combination of the Lorentz symmetry with the R-symmetry of the model.

For the case of $\mathcal{N} = 4$ SYM model, there are three different twisting procedures but the one we'll be interested in is the Marcus or GL twist of this model [30]. This procedure combines the global $SO(4)_E \sim SU(2) \times SU(2)$ symmetry with the $SO(4)_R \times U(1)$ subgroup global $SO(6)$ R-symmetry to obtain a new rotational group that can be given as the diagonal subgroup of $SO(4)_E \times SO(4)_R$. After this twisting procedure bosons and fermions of the theory become integer spin representations of the new rotation group which can be thought of as p-form tensors of the new rotation group.

This brings us to the second crucial part of the lattice construction for the $\mathcal{N} = 4$ SYM model which is to find representations for fermions and bosons where they can be naturally represented as p-form fields.

Let's start with the fermions. To express fermions as p-form fields, we will use what is known as Kähler-Dirac fermions [31]. This construction by Kähler provides a geometric interpretation for the fermions in which it is natural for them to be valued as p-form fields. The Kähler-Dirac equation can be written as

$$(\partial - \delta + m)\,\Phi = 0 \tag{1.31}$$

Where δ denotes the co-boundary operator and ∂ is the boundary operator both satisfy $\delta^2 = \partial^2 = 0$. For $d = 4$, the Kähler-Dirac equation describes 16 fermions which matches the number of bosonic degrees of freedom. Another property of Kähler-Dirac fermions is that in flat space they are equivalent to the staggered fermion construction that is used in QCD calculations. We have demonstrated that Kähler-Dirac fermions are also very useful in investigating symmetric mass generation, anomaly cancellation, and constructing chiral fermion models in lattice gauge theories but since these works don't fit with the general theme of the thesis we will not include them in our discussion [32–36].

To preserve the symmetry between fermions and bosons while retaining supersymmetry the next step is to choose a lattice structure that would be able to contain all these degrees of freedom in it. This can be achieved by using an unusual lattice called A_4^* lattice which includes a diagonal link in addition to the hypercubic links. These links can be given as

$$\hat{\mu}_1 = (1,0,0,0) \tag{1.32}$$

$$\hat{\mu}_2 = (0,1,0,0) \tag{1.33}$$

$$\hat{\mu}_3 = (0,0,1,0) \tag{1.34}$$

$$\hat{\mu}_4 = (0,0,0,1) \tag{1.35}$$

$$\hat{\mu}_5 = (-1,-1,-1,-1) \tag{1.36}$$

As can be seen from the above equations this lattice construction has 5 links which can also be related to the 5 complex gauge fields of the SYM model which are obtained through the combination of 6 scalars and 4 gauge fields. Also choosing such a lattice that treats all 5 links equally and preserves the S_5 symmetry which provides us a set of irreducible representations to match the twisted $SO(4)$ group of the SYM model.

With the two main ingredients of the lattice construction in hand, we are ready to explicitly discretize the $\mathcal{N} = 4$ SYM theory. We start with the supersymmetric lattice action from [13].

$$S = \frac{N}{4\lambda}\mathcal{Q}\sum_x \mathrm{Tr}\left[\chi_{ab}\mathcal{F}_{ab} + \eta\left(\overline{\mathcal{D}}_a\mathcal{U}_a + \kappa\left(\mathrm{Re}\det\mathcal{U}_a(x) - 1\right)I_N\right) + \frac{1}{2}\eta d\right] + S_{\text{closed}} \tag{1.37}$$

where the lattice field strength in terms of complexified gauge fields $\mathcal{U}_a(x)$ is given as

$$\mathcal{F}_{ab}(x) = \mathcal{U}_a(x)\mathcal{U}_b(x+\hat{a}) - \mathcal{U}_b(x)\mathcal{U}_a(x+\hat{b}) \tag{1.38}$$

These complexified gauge fields live on the lattice link running from $x \to x + \hat{a}$ and $\hat{a}$ denotes one of the five basis vectors of an underlying A_4^* lattice. As we mentioned before the

basis vectors for the A_4^* lattice constitute a set of five unit vectors that are proportional to the vectors drawn from the center of an equilateral 4-simplex to its 5 vertices.

Then the action of the covariant difference operator on the complexified gauge fields can be given as,

$$\overline{\mathcal{D}}_a \mathcal{U}_a = \mathcal{U}_a(x)\overline{\mathcal{U}}_a(x) - \overline{\mathcal{U}}_a(x-\hat{a})\mathcal{U}_a(x-\hat{a}). \tag{1.39}$$

Now we can focus on the fermionic field content. Starting with the scalar fermion $\eta(x)$ lives on the lattice site x and is associated with a conserved supercharge $\mathcal{Q}$. Then we have five fermion fields ψ_a, that are superpartners of the (complex) gauge fields. Which live on the corresponding links $x \to x + \hat{a}$ Finally, the ten fermion fields $\chi_{ab}(x)$ are associated with new face links running from $x + \hat{a} + \hat{b} \to x$.

The action of the supercharge $\mathcal{Q}$ on the field content can be given as,

$$\mathcal{Q}\,\mathcal{U}_a \to \psi_a \tag{1.40}$$

$$\mathcal{Q}\,\psi_a \to 0 \tag{1.41}$$

$$\mathcal{Q}\,\eta \to d \tag{1.42}$$

$$\mathcal{Q}\,d \to 0 \tag{1.43}$$

$$\mathcal{Q}\,\chi_{ab} \to \overline{\mathcal{F}}_{ab} \tag{1.44}$$

$$\mathcal{Q}\,\overline{\mathcal{U}}_a \to 0 \tag{1.45}$$

Notice that the idempotent nature of the supercharge $\mathcal{Q}^2 = 0$ guarantees the supersymmetric invariance of the first part of the lattice action. We include the auxiliary site field $d(x)$ which is needed for satisfying the nilpotency of $\mathcal{Q}$ offshell.

The second term in our action S_{closed} is given by

$$S_{\text{closed}} = -\frac{N}{16\lambda}\sum_x \text{Tr}\,\epsilon_{abcde}\chi_{ab}\overline{\mathcal{D}}_c\chi_{de} \tag{1.46}$$

which contains the action of the covariant difference operator on the fermion field χ_{de} which can be given as the following,

$$\overline{\mathcal{D}}_c\chi_{de}(x) = \overline{\mathcal{U}}_c(x-\hat{c})\chi_{de}(x+\hat{a}+\hat{b}) - \chi_{de}(x-\hat{d}-\hat{e})\overline{\mathcal{U}}_c(x+\hat{a}+\hat{b}) \tag{1.47}$$

The invariance of this term under the supersymmetry transformations can be shown with the use of an exact lattice Bianchi identity $\epsilon_{abcde}\overline{\mathcal{D}}_c\overline{\mathcal{F}}_{de} = 0$.

Now we can carry out the $\mathcal{Q}$ variation and integrate out the auxiliary field d. And obtain the final supersymmetric lattice action that's decomposed in terms of its bosonic and fermionic part $S = S_b + S_f$. The bosonic part takes the following form,

$$S_b = \frac{N}{4\lambda}\sum_x \mathrm{Tr}\left(\mathcal{F}_{ab}\overline{\mathcal{F}}_{ab}\right) + \frac{1}{2}\mathrm{Tr}\big(\overline{\mathcal{D}}_a\mathcal{U}_a + \kappa(\mathrm{Re}\det\mathcal{U}_a - 1)I_N\big)^2 \tag{1.48}$$

and the fermionic part is given as follows,

$$S_f = -\frac{N}{4\lambda}\sum_x \left(\mathrm{Tr}\,\chi_{ab}\mathcal{D}_{[a}\psi_{b]} + \mathrm{Tr}\,\eta\overline{\mathcal{D}}_a\psi_a + \frac{1}{4}\mathrm{Tr}\,\epsilon_{abcde}\chi_{ab}\overline{\mathcal{D}}_c\chi_{de}\right) - \tag{1.49}$$

$$\frac{\kappa N}{8\lambda}\sum_{x,a}\mathrm{Tr}(\eta)\det\mathcal{U}_a(x)\,\mathrm{Tr}\big(\mathcal{U}_a^{-1}(x)\psi_a(x)\big) \tag{1.50}$$

By taking the naive continuum limit as $\mathcal{U}_a = I + \mathcal{A}_a + \ldots$ one can show that this action is equivalent to the discretization of the Marcus or GL twist of $\mathcal{N} = 4$ Yang-Mills in flat space [37, 38]. In the continuum, this twisted formulation is used to construct a topological field theory but here the twisted construction is used as just a change of variables that allows for discretization while preserving the single exact supersymmetry $\mathcal{Q}$.

The fact that A_4^* lattice has a larger set of discrete rotational symmetries which corresponds to the S^5 can be used to control the renormalization of the theory [39]. By using this property it has been shown that the combination of gauge symmetry, $\mathcal{Q}$ supersymmetry and S^5 invariance ensures that the only relevant counterterms that can appear via quantum

corrections correspond to operators that are already contained within the classical lattice action together with a single new marginal operator of the form $\alpha \sum_{x,a} \mathrm{Tr}\,(\eta \mathcal{U}_a \overline{\mathcal{U}}_a)$. Then it's possible that one can add such a term to the lattice action and tune its coupling logarithmically with the lattice spacing to achieve a continuum limit with full supersymmetry but we have not investigated this in detail and set the coefficient equal to zero - its classical value in all our simulations.

Another interesting property of this construction arises when we impose the exact supersymmetry, all fields must reside in the algebra of the gauge group while being valued in the adjoint representation of $U(N)$: $f(x) = \sum_{A=1}^{N^2} T^A f^A(x)$ with $\mathrm{Tr}\big(T^A T^B\big) = -\delta^{AB}$.

Usually, this would be incompatible with lattice gauge invariance due to the measure not being gauge invariant for link-based fields. However, in this $\mathcal{N} = 4$ construction, the problem is not an issue since the fields are complexified which ensures that the Jacobians that arise after gauge transformation of $\mathcal{U}$ and $\overline{\mathcal{U}}$ cancel.

Finally, we can focus on the term involving the coupling κ which suppresses the troublesome $U(1)$ modes while leaving the important $SU(N)$ gauge symmetry intact. On top of that, another advantage of this term is it selects out gauge fields with unit determinants and it ensures that the gauge field has the expansion $\mathcal{U}_a(x) = I + \mathcal{A}_a(x) + \ldots$ where $\mathcal{A}_a$ are traceless complex fields. Which ensures the correct naive continuum limit.

The resultant action still possesses a degeneracy for the scalars which needs to be lifted by giving masses to the scalars this is achieved by the inclusion of the following term in the action,

$$S_{\mathrm{mass}} = \mu^2 \sum_x \mathrm{Tr}\,\big(\overline{\mathcal{U}}_a(x)\mathcal{U}_a(x) - I\big)^2 \tag{1.51}$$

While this breaks the exact supersymmetry softly all counter terms induced by this breaking will have couplings that are multiplicative in μ^2 and hence vanishing as $\mu^2 \to 0$.

We also still have a set of flat directions corresponding to constant gauge fields that are valued in the Cartan subalgebra which is a known issue for $\mathcal{N} = 4$ SYM model. We will

show in the next chapters that the inclusion of the new link determinant term will regulate these flat directions as well.

1.5 Review of Quantum Computing and Tensor Network Methods

In this final section of this chapter, we will diverge from our discussion on holography and super Yang-Mills models and review the simulation techniques and approaches we used in Chapter 4 of this thesis. Starting with introducing the circuit-based approach to quantum computing.

1.5.1 Circuit Based Quantum Computing

Circuit based quantum computing is a model of quantum simulation that has similar characteristics to classical circuits [40]. Computations in this model are carried out by application of a sequence of quantum gates together with measurements and initialization of qubits to the desired state. These crucial components of the circuit quantum model can be summarized as,

- State preparation: Initializing the qubits to the needed input state to start the computation.
- Quantum bit: These represent the data for the computation.
- Quantum gates: Acts on quantum bits to manipulate the data as desired
- Measurements: To read out the final result after the application of quantum gates.

The most basic unit of information on a quantum computer is a quantum bit which is also known as a qubit. A qubit describes a two-level quantum system where one of these levels is usually a ground state that's represented as $|0\rangle$ and an excited state $|1\rangle$. Unlike the classical bit which can only be in a 0 or 1 state quantum bit lives in a superposition state of both $|0\rangle$ and $|1\rangle$,

$$|\psi\rangle = \alpha\,|0\rangle + \beta\,|1\rangle \tag{1.52}$$

where α and β are complex numbers and they satisfy $|\alpha|^{+}|\beta|^{2} = 1$. Then if we measure this qubit in the basis of $|0\rangle$ and $|1\rangle$ we will find that it gives the 1 state with a probability of $|\beta|^{2}$ and a 0 state with a probability $|\alpha|^{2}$. A very useful way of visualizing a qubit is to use what is known as a Bloch sphere which can be seen in Fig. 1.1. Here the qubit is represented as a point on the surface of this sphere and $|0\rangle, |1\rangle$ corresponds to north and south poles. Operations on the $|\psi\rangle$ can be thought of as modifications of this vector on the Bloch sphere.

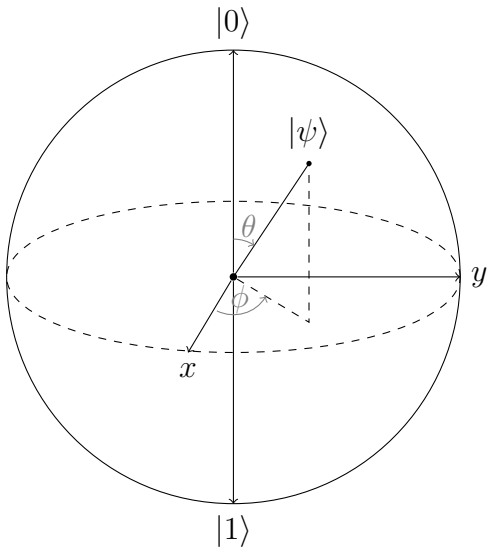

Figure 1.1: Bloch Sphere representation of a qubit

The basic ingredient of operations on a qubit is the use of single-qubit gates which changes the state of the qubit from $|\psi\rangle = \alpha\,|0\rangle + \beta\,|1\rangle$ to $|\psi'\rangle = \alpha'\,|0\rangle + \beta'\,|1\rangle$ while preserving the norm. These single qubit operations are described by 2×2 unitary matrices. Some examples of the single qubit gates are the Pauli matrices which are used to generate rotations around their corresponding axes on the Bloch sphere after exponentiation. For example, a rotation around the x-axis can be achieved as

$$R_x(\phi) = \exp(-i\phi Z/2) = \begin{pmatrix} \cos(\phi/2) & -i\sin(\phi/2) \\ -\sin(\phi/2) & \cos(\phi/2) \end{pmatrix} \tag{1.53}$$

Another example of a highly used single qubit operator is the Hadamard gate which is used to transform the qubit state from the $|0/1\rangle$ basis to a $|+/-\rangle$ basis, the quantum version of the classical NOT gate that is denoted as an X and the phase gate T. These are also defined as 2×2 unitary matrices and can be seen from below equations.

$$H = \sqrt{2} \begin{pmatrix} 1 & 1 \\ 1 & -1 \end{pmatrix} \tag{1.54}$$

$$X = \begin{pmatrix} 0 & 1 \\ 1 & 0 \end{pmatrix} \tag{1.55}$$

$$T = \begin{pmatrix} 1 & 0 \\ 0 & \exp(i\pi/4) \end{pmatrix} \tag{1.56}$$

However single-qubit gates by themselves are not enough to realize useful quantum algorithms without the use of multi-qubit gates. These are used to make two or more qubits interact with each other. The total state of two qubits can be given by taking the tensor product of their individual states

$$|\psi\rangle \otimes |\phi\rangle = \begin{pmatrix} a_\psi \\ a_\phi \end{pmatrix} \otimes \begin{pmatrix} b_\psi \\ b_\phi \end{pmatrix} = a_\psi b_\psi |00\rangle + a_\psi b_\phi |01\rangle + a_\phi b_\psi |10\rangle + a_\phi b_\phi |11\rangle \tag{1.57}$$

Then multiqubit or 2 qubit gates can be defined as operations acting on this product state. Now we'll give some examples for the most commonly used 2 qubit gates. Our first 2 qubit gate is the controlled-NOT (CNOT) gate where one of the qubits controls if the single qubit gate is applied to the other qubit. It can be given as

$$\text{CNOT} = \begin{pmatrix} 1 & 0 & 0 & 0 \\ 0 & 1 & 0 & 0 \\ 1 & 0 & 0 & 0 \\ 0 & 0 & 0 & 1 \\ 0 & 0 & 1 & 0 \end{pmatrix} \tag{1.58}$$

The action of this CNOT gate can be summarized as doing nothing if the first qubit is in state $|0\rangle$ and applying the NOT gate if the first qubit is in state $|1\rangle$. This control procedure can be applied to any single qubit unitary U where the application of operator U depends on the state of the first qubit.

A second example of a heavily used 2 qubit gate is the SWAP gate which swaps the $|01\rangle, |10\rangle$ to $|10\rangle, |01\rangle$ and its matrix form can be given as

$$\text{SWAP} = \begin{pmatrix} 1 & 0 & 0 & 0 \\ 0 & 0 & 1 & 0 \\ 1 & 0 & 0 & 0 \\ 0 & 1 & 0 & 0 \\ 0 & 0 & 0 & 1 \end{pmatrix} \tag{1.59}$$

Through combining two and single-qubit gates we can define a Universal gate set $\{\text{CNOT}, \text{H}, \text{T}\}$ that can implement any unitary operation on a given number of qubits [41].

We can use this machinery to simulate quantum systems via Hamiltonian simulation where the basic idea is to get the time-evolved state $|\psi(t)\rangle$ by the application of the time-evolution operator e^{-iHt} on the initial state where H is a time-independent Hamiltonian [42, 43]

$$|\psi(t)\rangle = e^{-iHt} |\psi(0)\rangle \tag{1.60}$$

Then we can use the fact that any unitary operator can be applied to a quantum state via

the use of the Universal gate set to simulate this model on quantum computers. However, the operator H is usually very hard to exponentiate so we employ an approximate technique to achieve this time-evolution. This approximate method is known as Suzuki-Trotter decomposition and it relies on the fact that for most physical systems the Hamiltonian can be written as a sum over local interactions

$$H = \sum_{i=1}^{L} H_i \tag{1.61}$$

where H_i only acts on a certain number of degrees of freedom. Since H_i acts on a much smaller subset than the full Hamiltonian it can be easily exponentiated to use in the quantum circuit. But a major obstacle in obtaining the full time evolution operator through this way is that for $[H_i, H_j] \neq 0$ which holds in general $e^{-iHt} \neq \prod_i e^{-iH_i t}$. However, we can use the Suzuki-Trotter formula to solve this issue.

$$e^{-iHt} = \left(e^{-iH_1 t/n} e^{-iH_2 t/n} \dots e^{-iH_L t/n}\right)^n + O(L^2 t^2/n) \tag{1.62}$$

which gives a good approximation when $n \gg Lt$. We will use this approach to obtain a quantum simulation of an Ising model that lives in an AdS_2 space in Chapter 4.

1.5.2 Quantum Inspired Tensor Networks

Even though quantum computers have come a very long way in the last couple of years. We're still currently in the Noisy Intermediate Scale Quantum (NISQ) era of quantum computation. Which makes it very hard to access regimes with interesting physics by just using quantum computers. Instead what we can do is while demonstrating quantum simulations on small system sizes using quantum computers, carry out larger simulations of these systems using Quantum Inspired Tensor Networks and simulate these quantum circuits classically. This approach allows us to probe system sizes and simulation times that are inaccessible with today's quantum computers. [44, 45]

The main building block of this approach is to approximate a quantum state $|\psi\rangle$ as a Matrix Product State(MPS). This is achieved by noticing that we can describe a general quantum state as

$$|\psi\rangle = \sum_{s_i} T_{s_1 s_2 \ldots s_L} |s_1 s_2 \ldots s_L\rangle \tag{1.63}$$

Where T is a tensor with L indices. Then by consecutive applications of singular value decompositions and reshapings, this tensor can be approximated by a product of matrices with a given bond dimension.

$$|\psi\rangle = \sum_{s_i} M^{s_1} M^{s_2} \ldots M^{s_L} |s_1 s_2 \ldots s_L\rangle \tag{1.64}$$

Where M's are now describing matrices. The biggest advantage of this decomposition is that it brings down the number of parameters needed to describe a tensor with L indices from d^L to dLm^2 where d denotes the dimension and m is the bond dimension. This reduces the number of parameters from an exponential to just a polynomial dependence. This scaling is crucial for the remarkable success these algorithms have achieved in simulating $1d$ systems. It is also very useful to visualize these tensor network formulations and the decomposition of a general tensor into an MPS can be visualized in Fig. 1.2

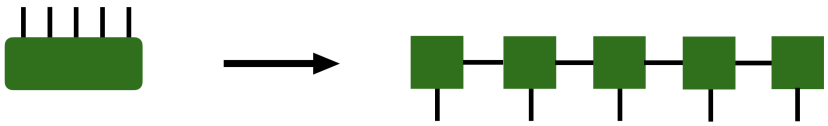

Figure 1.2: Decomposition of a Tensor into an MPS

Using the MPS description for the quantum state we can do any of the usual operations one would do to a quantum state. Starting with taking an inner product which can be written as

$$\langle\phi|\psi\rangle = \sum_{\vec{s}} \tilde{M}^{s_L\dagger} \dots \tilde{M}^{s_1\dagger} M^{s_1} \dots M^{s_L} \tag{1.65}$$

and can visualized as in Fig. 1.3

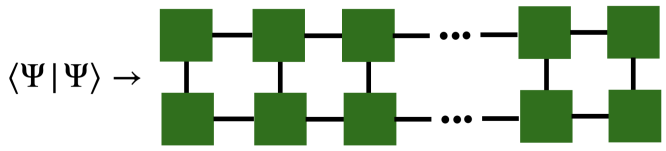

Figure 1.3: Inner Product of two MPS

We can also calculate expectation values for a general operator σ located in a site i

$$\langle\Psi|\,\sigma_i\,|\Psi\rangle = \sum_{s_i,s_i'} \hat{\sigma}^{s_i,s_i'} M^{s_i\dagger} M^{s_i'} \tag{1.66}$$

Again this process can be visualized as in Fig. 1.4

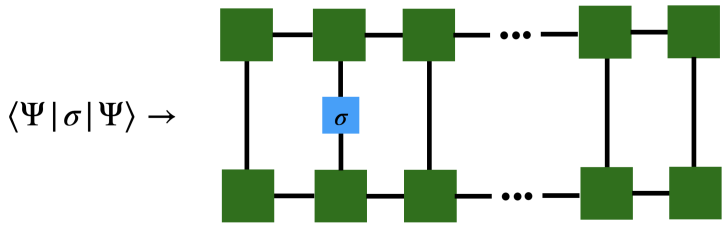

Figure 1.4: Calculating expectation values using MPS

The second main ingredient of this construction is to describe operators like the Hamiltonian in this formalism. That is achieved by representing them as Matrix Product Operators (MPO). To obtain this representation we start with a general operator acting on the L-site system and then follow the same procedure we did in obtaining the MPS where s, s' corresponds to the physical indices.

$$\hat{H} = \sum_{s,s'} c_{s,s'} \,|s\rangle\,\langle s'| \tag{1.67}$$

Then following the same procedure we did in obtaining the MPS

$$\hat{H} = \sum_{s,s'} H^{s_1,s'_1} \dots {}^{s_L,s'_L} |s\rangle \langle s'| \tag{1.68}$$

Where $H^{s_i s'_i}$ are a set of d^2 matrices. And this operator can be visualized as in Fig. 1.5

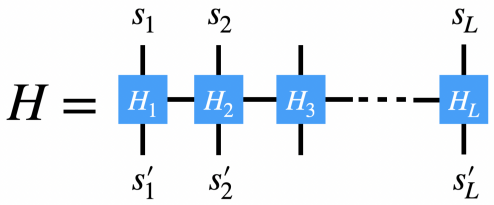

Figure 1.5: MPO representation of an operator H

Now that we have a description for a quantum state and a Hamiltonian H in terms of MPS and MPO. We are ready to find the ground state of our system. To find the ground state of a system that's described by an MPS we use a very powerful algorithm that is called Density Matrix Renormalization Group(DMRG). This is a variational algorithm that has been developed independently from the MPS techniques as a generalization of renormalization group to density matrices by S. White [46]. However, the inclusion of MPS in the context of DMRG simplified this algorithm considerably [45]. The basic idea behind the DMRG algorithm is to reduce the problem of minimizing ground state energy to a local minimization problem which can be done effectively this corresponds to solving the following equation one site at a time

$$\langle \psi_i | \hat{H} | \psi_i \rangle - \lambda \langle \psi_i | \psi_i \rangle \tag{1.69}$$

Where λ is a Lagrange multiplier. This minimization procedure corresponds to solving a generalized eigenvalue problem where the entries of the matrices M that describe our quantum state is minimized with respect to this equation which minimizes the energy. This minimization can be done one site at a time and sweeping across the chain multiple times until we reach the desired convergence for the approximate ground state energy. When the

desired convergence is reached the resulting MPS will give an approximation for the ground state of the model. Once we obtain the ground state of the system in terms of a MPS then it's possible to perform measurements by following the operations we described above.

This brings us to the question. Is it possible to achieve an efficient simulation of time evolution within this construction to investigate the dynamical properties of our system? The answer to that is yes and many different algorithms have been developed to achieve the time evolution of MPSs. [47, 48]

The algorithm we will use in our work is known as the Time Evolving Block Decimation (TEBD) algorithm. [47, 49] This algorithm can be thought of as a generalization of the usual Suzuki-Trotter decomposition for the MPS/MPO states. The time evolution is achieved by representing the Trotterized version of the time evolution operator $e^{-iH\delta t}$ in terms of an MPO and then successively applying this operator till we reach the desired t. This procedure can be visualized as in Fig. 1.6

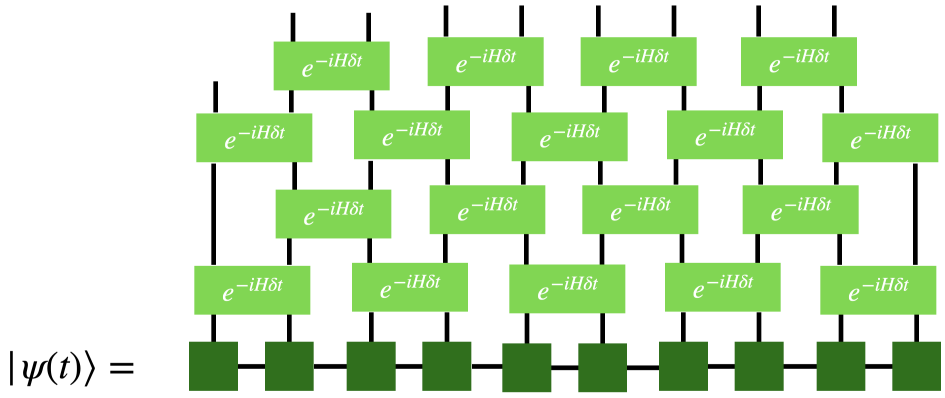

Figure 1.6: TEBD algorithm

All our discussions on tensor networks so far have been focused on quantum-inspired tensor networks to simulate quantum circuits on large scales. However, there are also Euclidean approaches to tensor networks mainly tensor network renormalization group (TRG) for bosonic theories and Grassmann TRG with the fermions included. We have also investigated these approaches in the context of lattice gauge theories but we will not include them

in our main discussion since they fall outside of the main scope of this thesis. [32, 33]

Chapter 2

Lattice $\mathcal{N} = 4$ super Yang-Mills at Strong Coupling

2.1 Introduction

In this chapter we use numerical simulation to explore the phase structure and Wilson loops of a lattice formulation of $\mathcal{N} = 4$ super Yang-Mills. The lattice action is a generalization of the formulation described in [12]. The theory preserves both $SU(N)$ gauge invariance, a S^4 point group symmetry associated with the underlying A_4^* lattice and most importantly a single exact supersymmetry.

The original supersymmetric lattice formulation of $\mathcal{N} = 4$ SYM has been the subject of a great deal of both numerical and analytical work [39, 50–52]. General arguments have been put forward that the theory should approach the continuum $\mathcal{N} = 4$ theory after tuning a single marginal operator. However, after some initial successes the numerical work has been handicapped by two problems: the existence of a chirally broken phase for 't Hooft couplings $\lambda > 4$ and the observation of a sign problem which develops in a similar region of coupling [53]. While these problems are not present in dimensionally reduced versions of the theory [54–62], they have prevented the systematic investigation of the four dimensional theory.

The chirally broken phase has been linked to the condensation of monopoles associated with the $U(1)$ sector of the theory [63]. We will show that the situation is markedly improved if one adds a new operator to the lattice action which preserves the S^4 symmetry and exact supersymmetry but explicitly breaks the $U(N)$ gauge symmetry down to $SU(N)$.

2.2 The new action

It has been observed that for couplings $\lambda > 2$ the action described in the previous section undergoes a phase transition to a regime in which both the Polyakov line and the Wilson loop fall abruptly toward zero. Associated with this is a growth in the density of lattice $U(1)$ monopoles [52]. These features are inconsistent with the expected superconformal phase of $\mathcal{N} = 4$ Yang-Mills. Actually, in pure compact QED in four dimensions, this monopole transition is a well known lattice artifact. Various efforts have been made over the intervening years to remove this monopole phase - typically this has been done by adding supersymmetric or non-supersymmetric terms to the action that force the determinant of the plaquette operator to unity. Such a procedure retains the full $U(N)$ gauge symmetry but restricts the fluctuations of the field strength in the $U(1)$ directions. The supersymmetric plaquette term introduced in [64] represents the best of these approaches but can only allow simulation up to $\lambda \sim 6.0$. It also suffers from a sign problem for $\lambda > 4$ [53] - that is, the Pfaffian arising after fermion integration, exhibits strong phase fluctuations which prohibit Monte Carlo sampling.

Here we explore an approach in which a new supersymmetric term is introduced which drives the determinant of each individual gauge link to unity. The new term takes the form

$$\frac{N}{4\lambda}\kappa\mathcal{Q}\sum_{x,a}\mathrm{Tr}(\eta)\left(\mathrm{Re}\det\left(U_a(x)-1\right)\right) \tag{2.1}$$

After $\mathcal{Q}$ variation and integration over d this modifies the second term in the bosonic action

S_b to:

$$\frac{N}{4\lambda}\sum_{x,a}\frac{1}{2}\,\mathrm{Tr}\left(\overline{\mathcal{D}}_a\mathcal{U}_a(x)+\kappa\mathrm{Re}\det(U_a(x))I_n\right)^2 \tag{2.2}$$

where I_N denotes the $N\times N$ unit matrix. A corresponding new fermion term is generated

$$\delta S_f=-\frac{N}{8\lambda}\kappa\sum_{x,a}\mathrm{Tr}(\eta)\det\left(U_a(x)\right)\mathrm{Tr}\big(U_a^{-1}(x)\psi_a(x)\big) \tag{2.3}$$

The new term has the effect of suppressing the $U(1)$ phase fluctuations of the complex gauge links that were the origin of the monopole problem. Of course this term explicitly breaks the $U(1)$ gauge symmetry. However since the $U(1)$ is simply a decoupled free theory in the continuum limit this should cause no real harm since $SU(N)$ gauge invariance is preserved. Indeed, close to the continuum limit, it should be apparent that the new terms merely generate mass terms for the trace components of the fields.

In the original theory the gauge links were valued in $GL(N,C)$. After this term is added the moduli space of the theory is reduced to $SL(N,C)$. Notice that since any matrix in $SL(N,C)$ can be written as the exponential of a traceless matrix the presence of this term *guarantees* that gauge links can be expanded about the unit matrix for vanishing values of the lattice spacing. In this light the remaining rationale for keeping S_{mass} is simply to lift the usual $SU(N)$ flat directions. Indeed, as the reader will see, for most of our results μ^2 is taken very small.

The breaking of $U(1)$ gauge invariance also clarifies a delicate issue concerning the invariance of the fermion measure in the original formulation. Consider the integration measure for the five link fermions $\prod_{x,a}d\psi_a(x)$ in the $U(N)$ theory. Under a gauge transformation $\psi_a(x)\to G(x)\psi_a(x)G^\dagger(x+\hat{a})$ this measure transforms by a non-trivial Jacobian corresponding to the product of the determinants of the gauge factors $G(x)$ and $G^\dagger(x+\hat{a})$. On the torus one can arrange an ordering of the fermion fields in the path integral measure such that these factors will cancel out along closed loops but this will not be possible for all lattice topologies. Thus the question of the invariance of the measure under the full $U(N)$ group

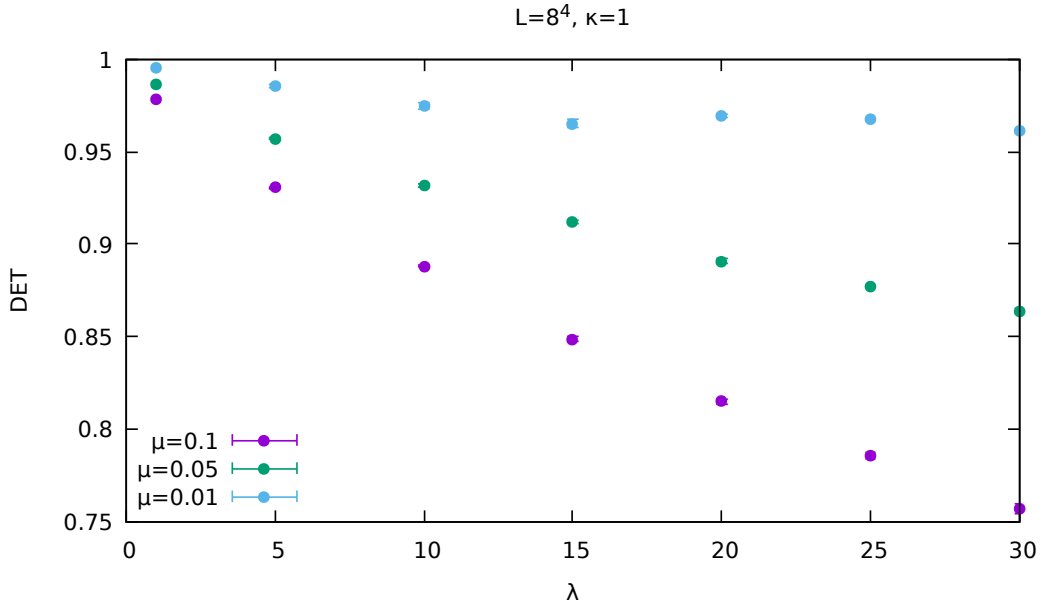

Figure 2.1: Expectation value of the determinant vs λ for 8^4 lattices at $\mu = 0.1, 0.05, 0.01$

is a delicate one. However these problems are completely avoided if G is restricted to lie in just $SU(N)$ as in the new action and the fermion measure is then unambiguously defined for an arbitrary lattice.

Of course the main question is whether such a term is effective at eliminating the monopole phase seen at strong coupling. In the next section we shall show evidence that this is true and at least in the case of 2 colors we see no sign of phase transitions out to arbitrarily large 't Hooft coupling.

2.3 Phase structure

Our simulations utilize the rational hybrid Monte Carlo (HMC) algorithm where the Pfaffian resulting from the fermion integration is replaced by

$$\mathrm{Pf}\,(M) = \left(\det M^\dagger M\right)^{\frac{1}{4}} \tag{2.4}$$

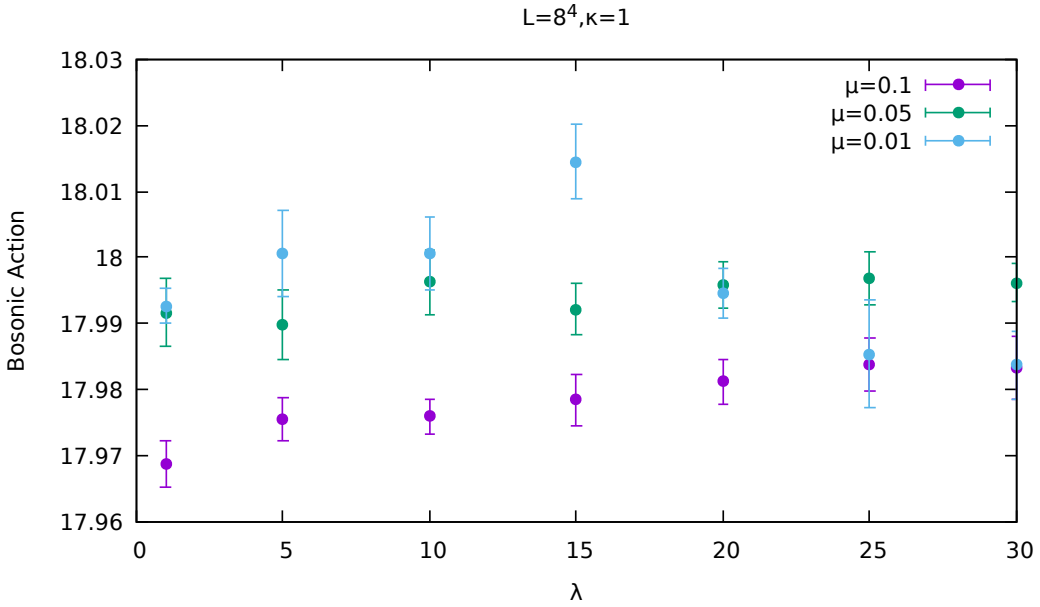

Figure 2.2: Expectation value of the bosonic action vs λ for 8^4 lattices at $\mu = 0.1, 0.05, 0.01$

where M is the fermion operator. Notice that this representation neglects any Pfaffian phase which is a key issue which we will return to later. Typical ensembles used in our analysis consist of 5000 HMC trajectories with $1000 - 2000$ discarded for thermalization. Errors are assessed using a jackknife procedure using $20 - 40$ bins.

As a test of the new action we first plot the expectation value of the link determinant as a function of 't Hooft coupling. We show results in Fig. 2.1 for 8^4 lattices at $\mu = 0.1, 0.05, 0.01$. Clearly the expectation value is close to unity out to very large λ provided μ^2 is small enough confirming that we have effectively reduced the gauge fields to $SU(2)$. We note that we scan out to $\lambda = 30$ in order to go beyond the self-dual point $\lambda_{\rm SD} = 4\pi N = 8\pi$.

In Fig. 2.2 we plot the expectation value of the bosonic action as a function of λ for 8^4 lattices at $\mu = 0.1, 0.05, 0.01$. This expectation value can be calculated exactly by exploiting the (almost) $\mathcal{Q}$-exact nature of the lattice action and yields $\frac{1}{V} < S_b >= \frac{9N^2}{2}$ for an N color theory on a system with (lattice) volume V *independent* of coupling λ. For $SU(2)$ this implies $S_B = 18.0$ for all λ. The results are clearly consistent with this prediction to a fraction of a percent as $\mu^2 \to 0$ even for very large values of the coupling confirming the presence of

an exact supersymmetry. Even more important there is no sign of the phase transition that had been seen before in the $U(2)$ theory. Indeed all the observables we have looked at show smooth dependence on λ providing evidence that the lattice theory possesses only a single phase out to arbitrarily arbitrarily strong coupling. It is interesting to note that the bosonic action is proportional to N^2 and not N^2-1 even though we suppress the $U(1)$ modes. That is because they are still present in this formulation; rather than being removed, they are being tamed. The new terms added to the action mostly affect the vacuum of these fields—which is why they still contribute to the counting of degrees of freedom.

Further confidence in this finding comes from studying a simple bilinear Ward identity given by $\left\langle \mathcal{Q}\,\mathrm{Tr}\big(\eta\mathcal{U}_a\overline{\mathcal{U}}_a\big)\right\rangle = 0$. Fig. 2.3 shows this quantity as a function of λ for several μ at $L = 8$. It falls slowly with λ and decreases more quickly with decreasing μ. To clarify its dependence on lattice size we plot the Ward identity for $\lambda = 10.0$ vs L for two values of μ in Fig. 2.4. This plot makes it clear that the Ward identity decreases with increasing L. Indeed comparing $L = 6$ at $\mu = 0.025$ with $L = 12$ at $\mu = 0.005$ suggests a roughly $1/L^2$ dependence on lattice size. Notice that to see this scaling requires decreasing μ with increasing L. But this is to be expected if the main purpose of this term is to lift the bosonic flat directions. The normalization of these bosonic zero modes brings in a factor of $1/V$ corresponding to a scaling of $1/\sqrt{V}$ in μ. This is roughly consistent with the data in this plot.

2.4 Absence of a sign problem

Of course these results are derived from simulations of a model in which the phase of the Pfaffian that results from fermion integration is neglected. To check for the presence of such a phase we have computed it using the ensemble of configurations generated in our phase quenched Monte Carlo. Writing the Pfaffian phase as $e^{i\alpha(\lambda,U)}$ we plot the quantity $1-\cos\alpha$ as a function of μ at $\lambda = 10.0$ and $\kappa = 1.0$ in Fig. 2.5. The different data points correspond to lattices of size 2^4, $3^2\times 4^2$, $3^3\times 4$ and 3×4^3 respectively. When measuring the phase of the

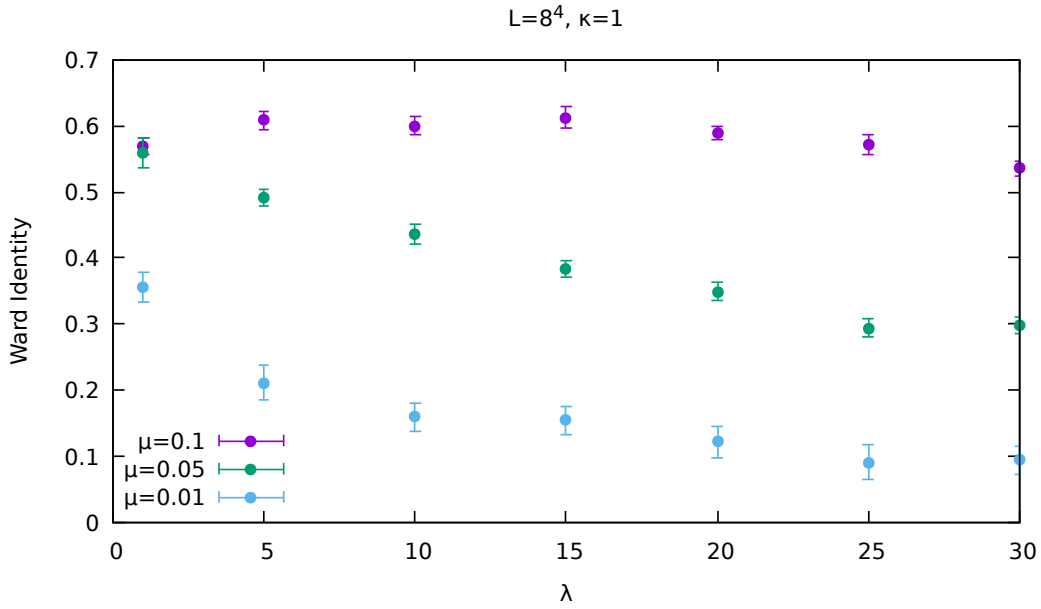

Figure 2.3: Bilinear $\mathcal{Q}$-susy ward identity vs λ for 8^4 lattices for $\mu = 0.1, 0.05, 0.01$

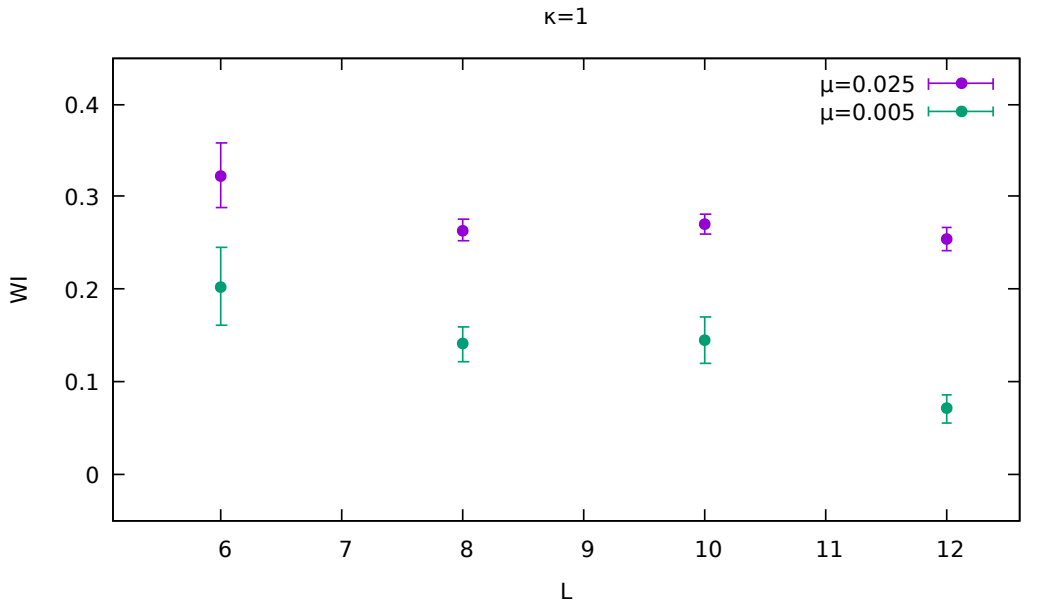

Figure 2.4: Bilinear $\mathcal{Q}$-susy ward identity vs L for $\mu = 0.025, 0.005$

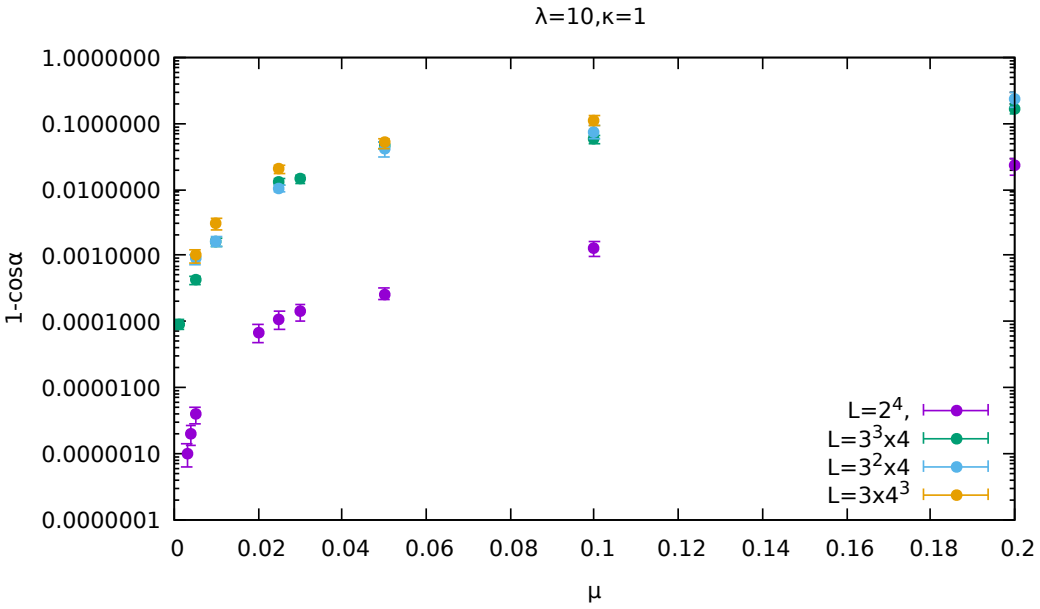

Figure 2.5: Pfaffian phase vs μ at $\lambda = 10.0$

Pfaffian we set $\kappa = 0$ in the fermion operator. Clearly the phase angle is driven towards very small values for small enough μ. We have observed this for all values of λ – the analogous plot fig. 2.11 for $\lambda = 30$ is shown in the appendix. Of course the lattices used in these tests are quite small and one should worry whether the sign problem returns on larger volumes. Our results suggest that this is not the case – the average phase appears to saturate as the volume increases. Systems with sign problems typically exhibit phase fluctuations that increase exponentially with volume. This lattice model seems very different in this regard.

Retaining the new $U(1)$ breaking fermion term in the evolution but neglecting it when measuring the phase is clearly a questionable procedure. However, the modification that is neglected relates to the trace modes, which decouple from the $SU(N)$ theory in the continuum in any case. So, in some sense we are discarding an irrelevant piece. Nevertheless, we have also generated ensembles in which the new fermion term is dropped from the fermion action in both the evolution and the measurement of the phase. A typical plot of the resultant phase versus for μ at $\lambda = 10.0$ is shown in Fig. 2.6 for several lattice volumes. The observed behavior is very similar to that seen in Fig. 2.5 and lends confidence to the assertion that

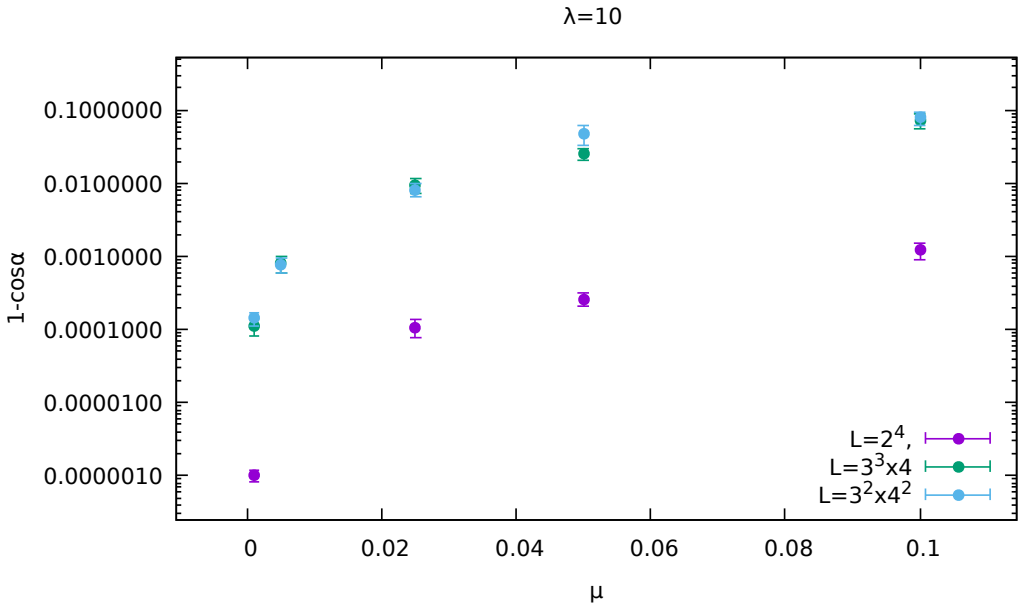

Figure 2.6: Pfaffian phase vs μ at $\lambda = 10.0$. Ensembles were generated without including the new fermionic term

the system does not suffer from a sign problem. Since this procedure breaks $\mathcal{Q}$-symmetry softly (proportional to κ) it leads to larger deviations in the Ward identities and so we have reinstated the new fermion term in our later simulations used for studying Wilson loops. The fact that eliminating the new fermion term from both the Pfaffian measurement and the simulation still preserves the good behavior can be understood as the new bosonic term accomplishing the most important task: stabilizing and suppressing the $U(1)$ modes of the link fields in a $\mathcal{Q}$-symmetric way that is only softly broken.

It is interesting to try and understand theoretically why the observed phase fluctuations are so small. We start by writing the expectation value of the phase measured in the phase quenched ensemble as

$$< e^{i\alpha(\lambda,\kappa,U)} >_{\text{phase quenched}} = \int D\mathcal{U} D\overline{\mathcal{U}}\, e^{i\alpha(\kappa,\lambda,\mathcal{U})} |\text{Pf}(\mathcal{U})| e^{-S_B(\lambda,\kappa,\mathcal{U})} = 1 \tag{2.5}$$

where we have chosen the normalization of the measure so that the full partition with susy preserving periodic boundary conditions (the Witten index) is unity. Furthermore,

$\mathcal{Q}$-invariance ensures that this expectation value of the phase factor is independent of κ and can be computed for $\kappa \to \infty$ where the partition function is saturated by configurations with unit determinant - the $SU(2)$ theory. Finally, the topological character of this partition function can be exploited to localize the integral to configurations which are constant over the lattice – the integral reducing to a Yang-Mills matrix model integral. The resultant Pfaffian for the $SU(2)$ matrix model is known to be real, positive definite [65]. Of course our simulations are performed at finite κ, and use a thermal boundary condition, but the numerical results strongly suggest that as a practical matter the phase fluctuations are small for the relevant range of parameters.

The encouraging results for the phase of the Pfaffian may also be related to the fact that out to very large λ the center symmetry is unbroken, so that Eguchi-Kawai reduction [66] may be valid. In that case the theory is equivalent to a single-site lattice, where the gauge theory is in fact just the matrix model that has been indicated in the previous paragraph. This may also explain why we are able to obtain results consistent with large N predictions (below), since the fact that we are in volumes larger than a single site may in fact translate into larger N in the reduced model.

2.5 Supersymmetric Wilson loops

The previous results provide strong evidence that the lattice theory exists in a single phase with unbroken supersymmetry out to very large values of the gauge coupling and that the model can be simulated with a Monte Carlo algorithm without encountering a sign problem. With this in hand we turn to whether the lattice simulations can provide confirmation of known results for $\mathcal{N} = 4$ Yang-Mills at strong coupling. Most of these analytic results were obtained by exploiting the AdS/CFT correspondence which allows strong coupling results in the gauge theory to be obtained by solving a classical gravity problem in anti-de Sitter space. Using this duality a variety of results for *supersymmetric* Wilson loops have been

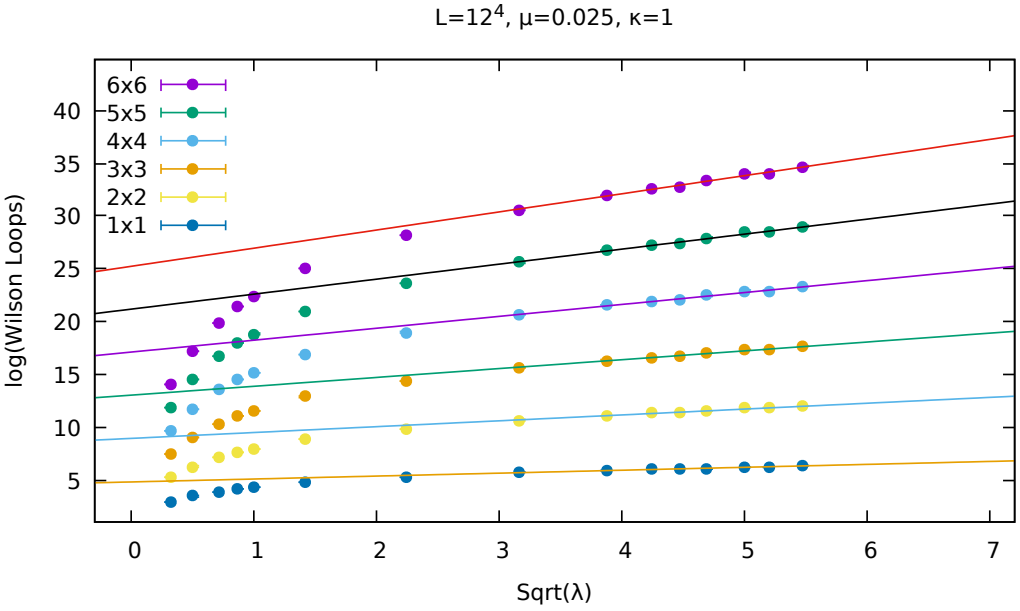

Figure 2.7: Supersymmetric $n \times n$ Wilson loops on 12^4 lattice at $\mu = 0.025$

obtained over the last twenty years. Such Wilson loops generalize the usual Wilson loops by including contributions from the scalars and are realized in the twisted construction by forming path ordered products of the *complexified* lattice gauge fields $\mathcal{U}_a$. In the continuum the generic feature of such Wilson loops is that for strong coupling they depend not on λ as one would expect from perturbation theory but instead vary like $\sqrt{\lambda}$. In Fig. 2.7 we show the logarithm of the $n \times n$ supersymmetric Wilson loops $W(n, n)$ for a 12^4 lattice at $\kappa = 1.0$ plotted as a function of $\sqrt{\lambda}$. The straight lines correspond to fits with $\sqrt{\lambda} \geq 3$. It is clear that all the loops show a $\sqrt{\lambda}$ dependence at strong coupling in agreement with the holographic prediction. This is encouraging. It is also clear that the fits show a linear dependence on the length of the perimeter of the loop. If we parametrize the static potential defined by $W(R, T) = e^{-V(R)T}$ in the form

$$V(R) = \sigma(\lambda)R + \alpha(\lambda)/R + M(\lambda) \tag{2.6}$$

The presence of the constant term $M(\lambda)$ will yield the observed perimeter scaling provided the string tension is small or zero. Such a perimeter term also occurs in continuum treatments

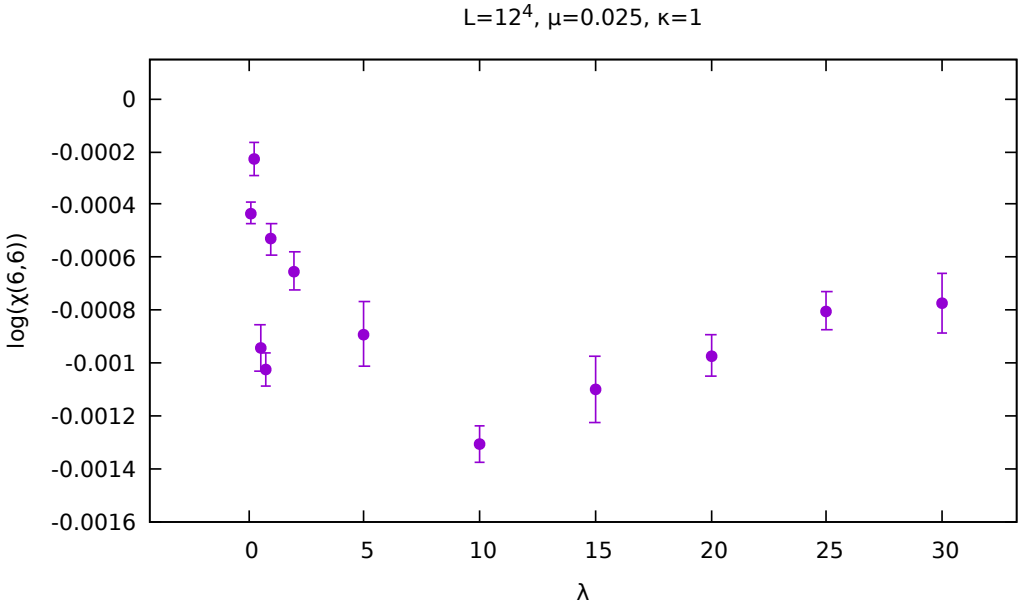

Figure 2.8: Estimated string tension vs λ for 12^4 lattice at $\mu = 0.025$ using $\chi(6,6)$

where it corresponds to the energy of a static probe source in the fundamental representation and has to be explicitly subtracted out to see the non-abelian Coulomb behavior hidden in $\alpha(\lambda)$ [67].

One way to remove the perimeter dependence is to consider Creutz ratios defined by

$$\chi(R,T) = \frac{W(R,T)W(R-1,T-1)}{W(R,T-1)W(R-1,T)} \tag{2.7}$$

For a theory with Wilson loops containing both perimeter, area and Coulomb behaviors one finds

$$\ln \chi(R,R) \sim -\sigma(\lambda) + \alpha(\lambda)/R^2 \tag{2.8}$$

Thus we can read of the string tension by examining the large R behavior of $\ln \chi(R,R)$. In Fig. 2.8 we plot $\ln \chi(6,6) = -\sigma$ versus λ for a 12^4 lattice at $\lambda = 10.0$ and $\mu = 0.025$.

Clearly, the string tension is very small even at strong coupling which is consistent with the existence of a single superconformal phase in the theory in the IR. Of course the most interesting question is whether we can see evidence for a non-abelian Coulomb potential at

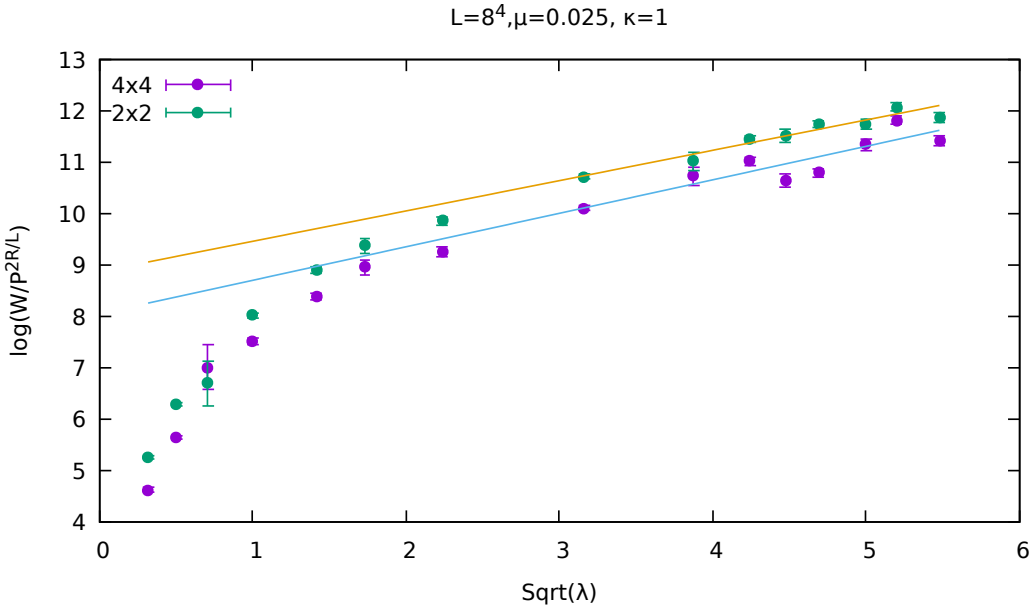

Figure 2.9: Renormalized supersymmetric 4×4 and 2×2 Wilson loops on 8^4 lattice at $\mu = 0.025$

small R. Direct fits to the Creutz ratio are consistent with the presence of such a term but the errors in $\alpha(\lambda)$ are large.

An alternative way to probe for this is is to divide the original Wilson loops by an appropriate power of the measured Polyakov line P which is given by product of gauge links along a thermal cycle. The (logarithm of the) Polyakov line also picks up a term linear in the length of the lattice due to a massive source and hence can used to subtract the linear divergence in the rectangular Wilson loop. We thus define a renormalized Wilson loop on a L^4 lattice of the form

$$W^R(R,R) = \frac{W(R,R)}{P^{\frac{2R}{L}}} \tag{2.9}$$

These are shown in Fig. 2.9 for a 8^4 lattice. Notice that the 2×2 and 4×4 loops now lie near to each other which is consistent with conformal invariance and the presence of a non-abelian Coulomb term while the strong coupling behavior still exhibits a dependence on $\sqrt{\lambda}$. This result can also be seen on the larger 12^4 lattice shown in Fig. 2.10. Notice that the average slope in this case is somewhat larger than the data on 8^4. This presumably

reflects the residual breaking of conformal invariance due to finite volume as well as finite lattice spacing. However it may also indicate that our definition of a renormalized Wilson loop does not do a perfect job of subtracting all the linear divergences needed to reveal an underlying Coulombic term. Further work is needed on larger lattices to clarify this issue.

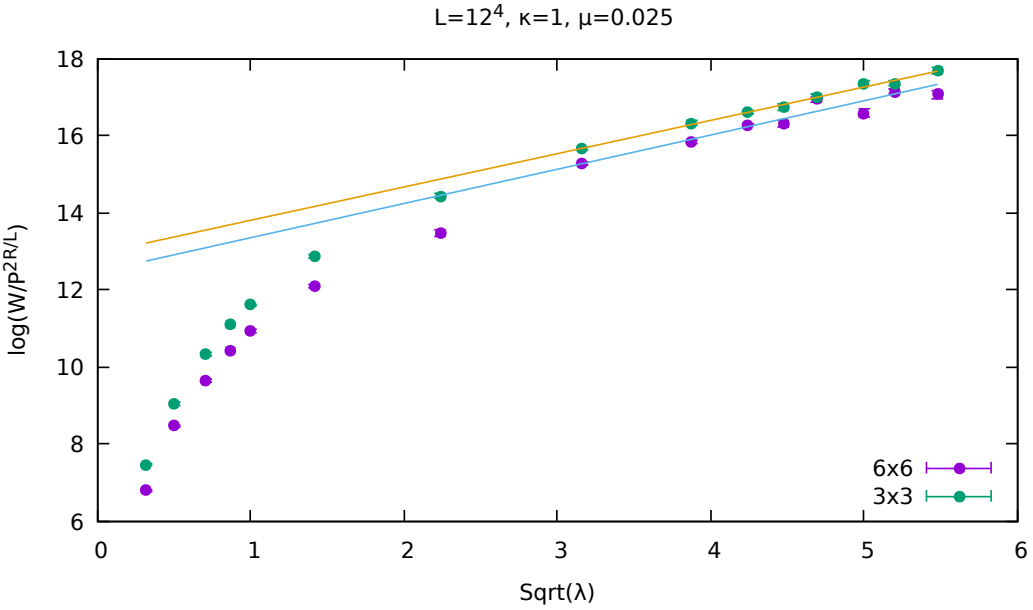

Figure 2.10: Renormalized supersymmetric 6×6 and 3×3 Wilson loops on 12^4 lattice at $\mu = 0.025$

Details of the fits for the different Wilson loops and lattice are shown in tables 2.1,2.2.

The square root behavior at large λ is consistent with the result for circular Wilson loops in $\mathcal{N} = 4$ SYM derived by Gross and Drukker [68] and Maldacena's holographic argument [69]. There are also explicit calculations using holography for the rectangular Wilson loop in [67]. The strange $\sqrt{\lambda}$ dependence *cannot* be seen in perturbation theory and this (admittedly) very preliminary result is a very non-trivial test of the correctness of the lattice approach in a non-perturbative regime.

Loop Size	a$\sqrt{\lambda}$+b	Reduced-χ^2
4×4	$0.6(1)\sqrt{\lambda} + 8.0(4)$	8.11
2×2	$0.59(4)\sqrt{\lambda} + 8.8(2)$	2.25

Table 2.1: Normalized Supersymmetric Wilson loop fits on 8^4 lattice at $\mu = 0.025$ for $f(\lambda) = a\sqrt{\lambda} + b$

Loop Size	a$\sqrt{\lambda}$+b	Reduced-χ^2
6×6	$0.88(7)\sqrt{\lambda} + 12.4(3)$	6.58
3×3	$0.86(2)\sqrt{\lambda} + 12.94(9)$	0.90

Table 2.2: Normalized Supersymmetric Wilson loop fits on 12^4 lattice at $\mu = 0.025$ for $f(\lambda) = a\sqrt{\lambda} + b$

2.6 Conclusions

We have found that a supersymmetric modification of the lattice action enables us to extend our simulations to what seem to be arbitrarily large values of the 't Hooft coupling without encountering difficulties that had previously limited our studies to modest λ. This seems to be attributable to stabilizing the potential for the $U(1)$ modes in a way that preserves the essential $\mathcal{Q}$ supersymmetry of the construction. The current study has been limited to gauge group $SU(2)$. It is natural to inquire what occurs for this construction for other $SU(N)$. We will investigate this in future studies; however, we expect that a sign problem will reemerge since in the zero-dimensional matrix models for $N > 2$ the Pfaffian is no longer strictly positive.

2.7 Appendix

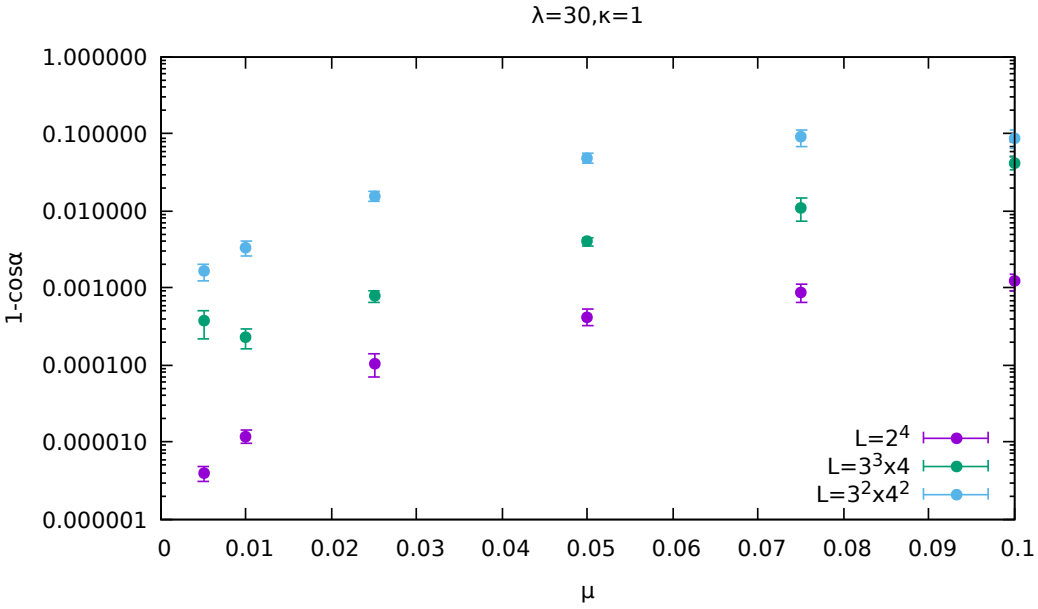

Figure 2.11: Pfaffian phase vs μ at $\lambda = 30.0$

Chapter 3

Holography from lattice $\mathcal{N} = 4$ super Yang-Mills

3.1 Introduction

$\mathcal{N} = 4$ super Yang-Mills is both a fascinating and non-trivial quantum field theory. It possesses a line of conformal fixed points, is conjectured to be invariant under a strong-weak coupling duality, and most importantly, furnishes the original example of holographic duality by providing a description of type IIb string theory on five dimensional anti-de Sitter space. The holographic description is most easily understood in the planar $N_c \to \infty$ strong coupling limit where the five dimensional theory reduces to classical supergravity. However, string loop corrections arise at $O(\frac{1}{N_c})$ and are difficult to access analytically. This provides motivation to study the theory using numerical simulation.

Naive approaches to constructing a lattice theory break supersymmetry completely and lead to a large number of relevant supersymmetry breaking counterterms whose couplings would need to be tuned to take a continuum limit. This stymied progress for many years until models were constructed that preserved one or more supercharges at non-zero lattice spacing - see the review [12] and references therein. The key idea underlying these constructions

is to find linear combinations of the continuum supercharges that are nilpotent and hence compatible with finite lattice translations. This may be accomplished either by discretization of a topologically twisted version of the supersymmetric theory [70] or by building a lattice theory from a matrix model using orbifolding and deconstruction techniques [71–73].

While these developments have led to many numerical studies providing evidence supporting holography for dimensional reductions of $\mathcal{N} = 4$ Yang-Mills [54–62, 74] it has proven difficult until recently to test holography directly in four dimensions. The original supersymmetric construction in four dimensions produced lattice artifacts in the form of $U(1)$ monopoles that condense and lead to a chirally broken phase for 't Hooft couplings $\lambda > 4$ [51, 52]. Recently we have constructed a new lattice action that appears to avoid these problems [13]. It differs from both the original and improved [64] actions for $\mathcal{N} = 4$ SYM by the addition of a new supersymmetric term that breaks the gauge symmetry from $U(N)$ to $SU(N)$. This removes the monopoles completely and, as we will show in this paper, yields a single non-Abelian Coulomb phase.

3.2 Testing Holography with $SU(3)$ SYM)

Our simulations utilize the rational hybrid Monte Carlo (HMC) algorithm where the Pfaffian resulting from the fermion integration is replaced by

$$\mathrm{Pf}\,(M) = \det\left[\left(M^\dagger M\right)^{\frac{1}{4}}\right] \tag{3.1}$$

where M is the fermion operator and the fractional power is replaced by a rational fraction approximation [75]. In principle this throws away any phase in the fermion operator. In the appendix of this chapter (Fig. 3.6) we show that this phase is always small even at strong coupling for sufficiently small μ^2. Typical ensembles used in our analysis consist of $3500-4000$ HMC trajectories with $750-800$ discarded for thermalization. Errors are assessed using a jackknife procedure using $20-40$ bins. We also fix $\kappa = 1$ for all our simulations.

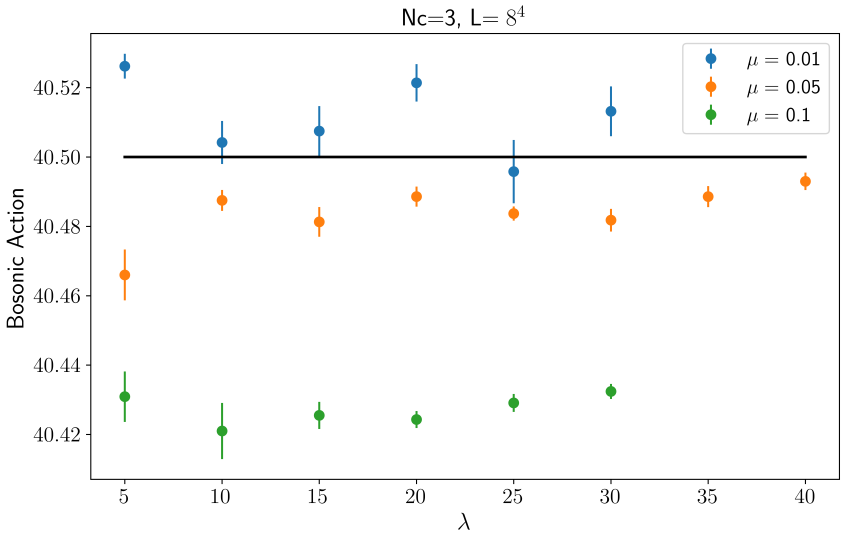

Figure 3.1: Bosonic Action vs λ for 8^4 lattice at $\kappa = 1.0$ for various values of μ

One of the simplest observables that can be measured is the expectation value of the bosonic action. This can be calculated exactly at any coupling by exploiting the exact lattice supersymmetry. We start by rescaling the fermions to remove the dependence of the $\mathcal{Q}$-closed term on $\beta = \frac{N}{4\lambda}$ so that the partition function Z is given by

$$Z = \beta^{\frac{-6N^2V}{2}} \int D\eta D\psi D\chi DU D\overline{\mathcal{U}} Dd \, e^{-\beta\mathcal{Q}\Lambda - \chi\overline{\mathcal{D}}\chi} \tag{3.2}$$

where Λ generates the $\mathcal{Q}$-exact terms in the action and V is the number of lattice points. After integrating over the auxiliary field d one finds that the coefficient $-\frac{6}{2}N^2V$ is shifted to $-\frac{7}{2}N^2V$. But

$$-\frac{\partial \ln Z}{\partial \beta} = < S_B > - < S_F > = -\frac{7N^2V}{2\beta} + < \mathcal{Q}\Lambda > \tag{3.3}$$

Using the $\mathcal{Q}$ Ward identity $< \mathcal{Q}\Lambda >= 0$ and the fact that the expectation value of the fermion action can be trivially found by a scaling argument since the fermion fields appear only quadratically one finds the final result

$$\frac{1}{V}\beta S_B = \frac{9N^2}{2} \tag{3.4}$$

Fig.3.1 shows the bosonic action density as a function of λ for several values of the susy breaking mass μ. It should be clear that the measured values approach the exact result $< \beta\frac{S_B}{V} >= 40.5$ independent of λ as $\mu \to 0$.

To check that we have indeed suppressed the $U(1)$ modes we plot the expectation value of the link determinant in Fig. 3.2. Clearly the observed value of the link determinant lies close to unity for all 't Hooft couplings provided that μ is small enough. Notice that both the bosonic action and the link determinant show no sign of a phase transition over the range $0 < \lambda < 40$. This is consistent with the continuum expectation that the $\mathcal{N} = 4$ SYM theory exists in a single phase out to arbitrarily strong coupling.

The conclusion is strengthened further by examining a variety of supersymmetric Wilson

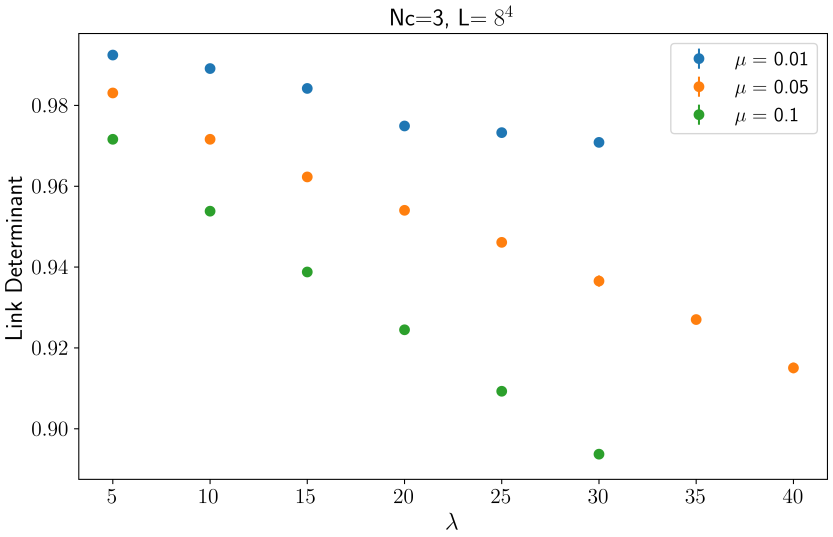

Figure 3.2: Link Determinant vs λ for 8^4 lattice and $\kappa = 1.0$

loop corresponding to the product of complexified lattice gauge fields around a closed loop on the lattice. We have plotted the logarithm of such Wilson loops as a function of $\sqrt{\lambda}$ in Fig. 3.3. Clearly the behavior is smooth as λ varies and again there is no sign of any phase transition. Furthermore the linear dependence of W seen for large λ is consistent with holography. Indeed, both square and circular Wilson loops can be computed in the strong coupling planar limit and show a $\sqrt{\lambda}$ dependence on the 't Hooft coupling [68, 69]. It should

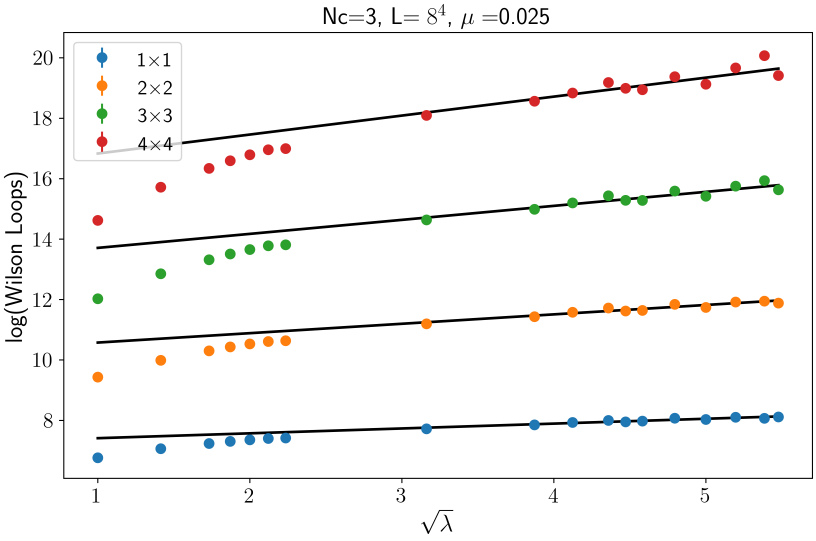

Figure 3.3: $R \times R$ Wilson Loops vs $\sqrt{\lambda}$ for 8^4 lattices at $\mu = 0.025$ and $\kappa = 1.0$

be noted that this λ dependence *cannot* be seen in perturbation theory and constitutes a non-trivial test that the lattice model is able to reproduce the non-perturbative physics of the continuum theory.

However Fig. 3.3 makes it clear that there is also a perimeter dependence to the Wilson loop. This is not unexpected and arises also in the continuum calculations as a regulator term associated with a bare quark mass. In general the Wilson loop arises as the amplitude

for the propagation of heavy fundamental sources that interact via a static potential of the form

$$V(r) = -\frac{\alpha}{r} + M \tag{3.5}$$

where M represents the static quark mass. To subtract the perimeter term from our analysis and look for the presence of an underlying non-abelian Coulomb term in the static potential we have turned to another related observable – the correlation function of two Polyakov lines. These are just Wilson lines that close via the toroidal boundary conditions. The measured correlator is defined by

$$P(r) = \sum_{x,y} \left[< P(x)P^{\dagger}(y) > - < P(x) >< P^{\dagger}(y) > \delta(r, |x-y|) \right] \tag{3.6}$$

where $|x-y|$ is the distance in the A_4^* lattice. As for the Wilson loop it is expected to vary like

$$P(r) \sim e^{-V(r)t} \tag{3.7}$$

with $V(r)$ the static potential. In practice we have computed this correlator on ensembles of

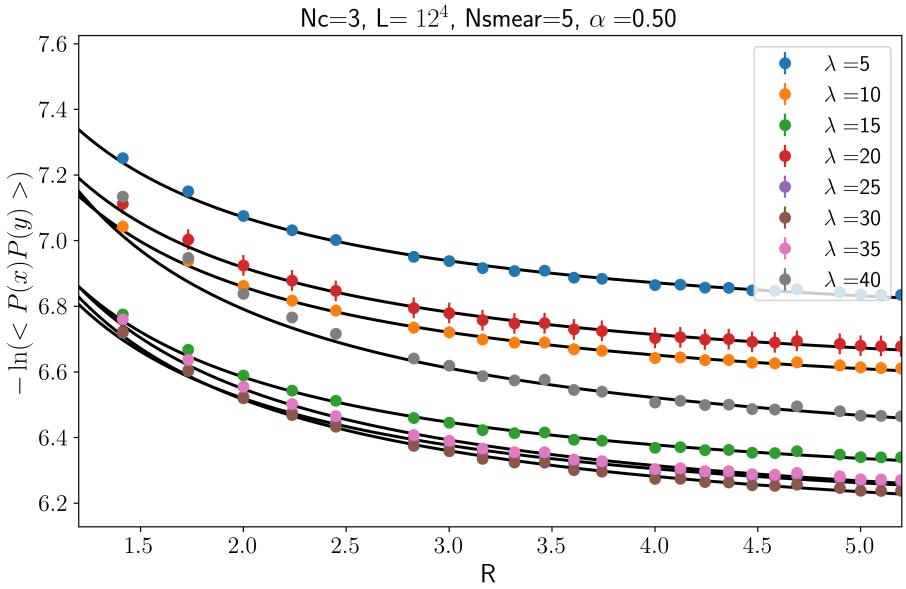

Figure 3.4: $-\ln < P(x)P(y) >$ vs R for 12^4 lattices at $\mu = 0.05$ and $\kappa = 1.0$

smeared Polyakov lines. Smearing the lattice gauge fields is a procedure for replacing each of the lattice gauge links by an average over neighboring link paths or staples. This smearing procedure has the effect of reducing U.V effects and increasing the signal to noise ratio in observables that depend on the gauge field. It also suppresses the contribution of any bare quark mass. We have used the APE smearing procedure which replaces the link fields $\mathcal{U}$ in the following way

$$\mathcal{U}_a(x)^{(N_{smear})} = (1-\alpha)\mathcal{U}_a(x)^{(N_{smear}-1)} + \frac{\alpha}{8(1-\alpha)}\mathcal{S}_a(x)^{(N_{smear}-1)} \tag{3.8}$$

where $\mathcal{S}$ denotes the sum over directional staples, N_{smear} denotes the number of iterative smearing steps and α is the smearing coefficient [76].

We have fitted the correlator for a range of smearing parameters at each value of λ assuming a non-abelian Coulomb form for $V(r)$ – see the tables 3.1-3.3 in the appendix. In practice we find that $N_{smear} = 5$ and $0.45 \leq \alpha \leq 0.55$ yields good, robust fits to the data over the range $2 < r < 5$ on a 12^4 lattice. Fig. 3.4 shows the logarithm of this correlator for a lattice of size $L = 12^4$ with $\mu = 0.05$ with $N_{smear} = 5, \alpha = 0.50$.

Taking the coefficients from these Coulomb fits and plotting them as a function of $\sqrt{\lambda}$ we again see a linear dependence on $\sqrt{\lambda}$ which is consistent with the holographic expectation [77] . Indeed, even the numerical coefficient in the fit lies within 10% or so of the holographic prediction which can be seen in Fig. 3.5. Note that the holographic prediction has been expressed in terms of the lattice coupling λ and not the continuum coupling. In the appendix 3.5 we include equivalent fits (Figs. 3.9 and 3.10) for a range of different smearing parameters thereby verifying that the agreement with the holographic prediction is robust.

3.3 Conclusions

We have studied a new supersymmetric lattice action for $\mathcal{N} = 4$ super Yang-Mills in four dimensions at strong 't Hooft coupling. We have focused on the case of three colors $\mathcal{N} = 3$

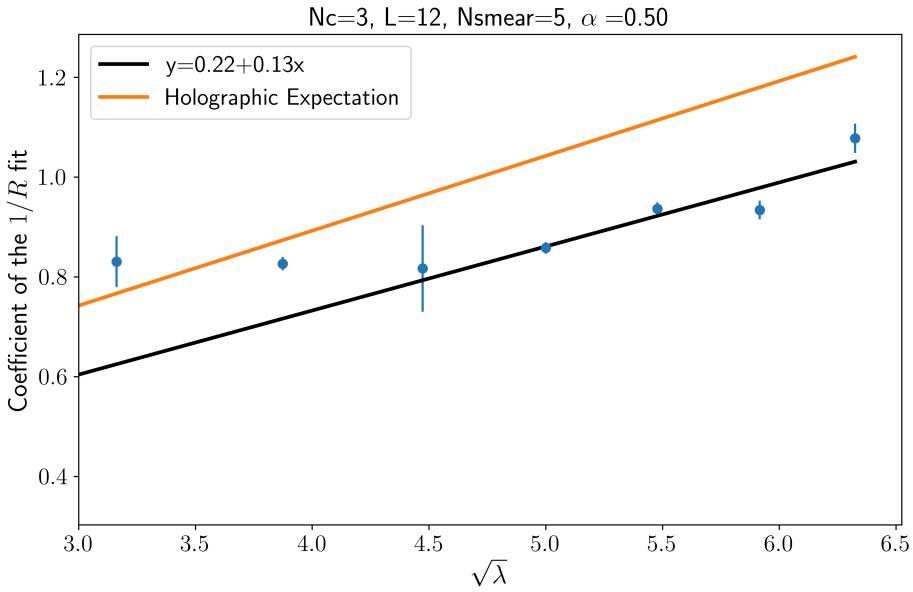

Figure 3.5: Coefficient of the $1/r$ vs $\sqrt{\lambda}$ for 12^4 lattices at $\mu = 0.05$

and utilized lattices as large as 12^4. Our results provide strong evidence for the existence of a single deconfined phase for all 't Hooft couplings consistent with the expected conformal phase of $\mathcal{N} = 4$ super Yang-Mills. In particular the new action shows no sign of lattice monopole condensation at strong coupling which plagued earlier actions with exact supersymmetry. The way is now open for using numerical simulation to explore a wide set of non-perturbative features of $\mathcal{N} = 4$ super Yang-Mills such as anomalous dimensions, S-duality and the computation of stringy corrections to holography.

As a first step in these directions we have computed correlators of (smeared) Polyakov lines that can be used to extract the static potential. We find that it exhibits the expected non-Abelian Coulomb form $V(r) = \frac{\alpha\sqrt{\lambda}}{r}$ where the value of α and the square root dependence on the 't Hooft coupling match expectations from holography.

3.4 Appendix - Phase of the Pfaffian

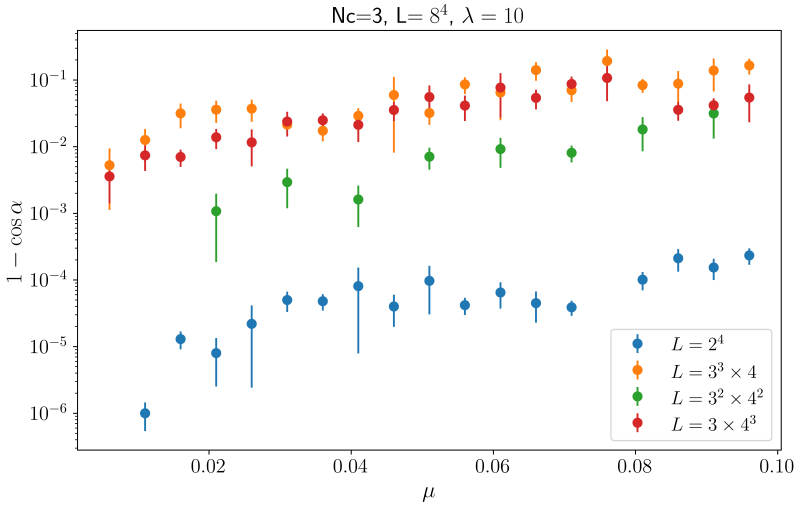

Figure 3.6: $1 - cos(\alpha)$ vs μ for $L = 2^4, 3^3 \times 4, 3^2 \times 4^2, 4^3 \times 3$

3.5 Appendix – Dependence of the fits on smearing parameters

λ	$a + b/R$	Reduced-χ^2
5	$6.51(1) + 0.76(3)/R$	0.18
10	$6.29(1) + 0.78(5)/R$	0.085
15	$6.03(4) + 0.79(1)/R$	1.6
20	$6.06(1) + 0.80(5)/R$	0.13
25	$5.92(1) + 0.81(2)/R$	1.4
30	$5.91(1) + 0.92(1)/R$	1.8
35	$5.96(1) + 0.93(2)/R$	1.2
40	$6.22(2) + 0.97(1)/R$ $(3.5 < R < 5.0)$	2.3

Table 3.1: $1/R$ Fitting results for $L = 12^4, \mu = 0.05, N_{smear} = 5, \alpha = 0.45$

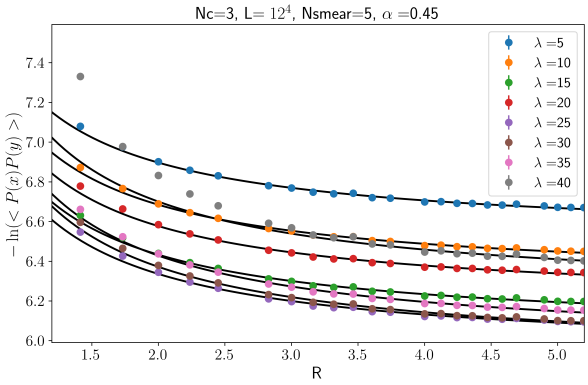

Figure 3.7: $-\ln < P(x)P(y) >$ for $\alpha = 0.45$

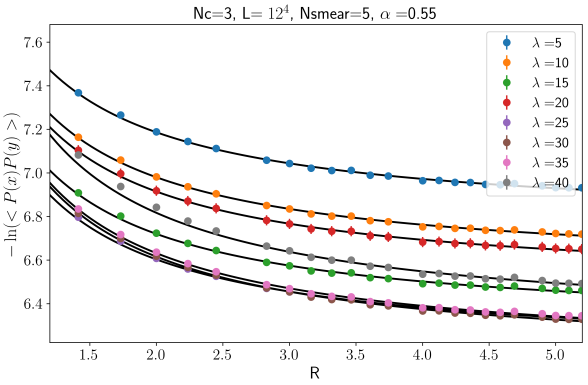

Figure 3.8: $-\ln < P(x)P(y) >$ for $\alpha = 0.55$

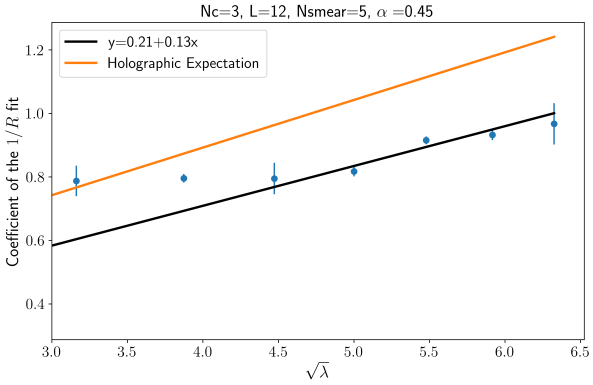

Figure 3.9: Coefficient of the $1/r$ vs $\sqrt{\lambda}$ for $\alpha = 0.45$

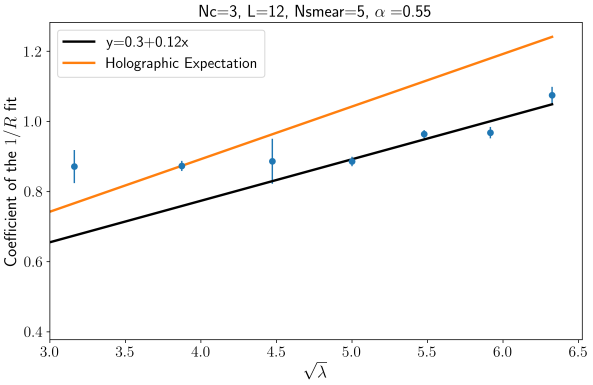

Figure 3.10: Coefficient of the $1/r$ vs $\sqrt{\lambda}$ for $\alpha = 0.55$

λ	$a + b/R$	Reduced-χ^2
5	$6.67(1) + 0.79(4)/R$	0.16
10	$6.44(2) + 0.83(5)/R$	0.07
15	$6.17(1) + 0.82(1)/R$	1.50
20	$6.51(3) + 0.81(8)/R$	0.04
25	$6.09(1) + 0.86(2)/R$	2.10
30	$6.09(1) + 0.937(1)/R$	1.34
35	$6.05(1) + 0.934(2)/R$	0.92
40	$6.25(1) + 1.07(2)/R$ $(3.0 < R < 5.0)$	3.03

Table 3.2: $1/R$ Fitting results for $L = 12^4, \mu = 0.05, N_{smear} = 5, \alpha = 0.50$

λ	$a + b/R$	Reduced-χ^2
5	$6.76(1) + 0.85(3)/R$	0.17
10	$6.54(1) + 0.87(5)/R$	0.09
15	$6.28(1) + 0.87(1)/R$	1.23
20	$6.47(2) + 0.88(6)/R$	0.06
25	$6.09(1) + 0.88(1)/R$	1.53
30	$6.13(1) + 0.96(1)/R$	1.47
35	$6.14(1) + 0.97(2)/R$	0.90
40	$6.28(1) + 1.07(2)/R$ $(2.5 < R < 5.0)$	2.48

Table 3.3: $1/R$ Fitting results for $L = 12^4, \mu = 0.05, N_{smear} = 5, \alpha = 0.55$

Chapter 4

Simulations of Quantum Ising Model on AdS_2

4.1 Introduction

One of the most fruitful ideas in theoretical physics developed over the last twenty-five years has been the concept of holographic duality – that the physical content of a gravitational theory in anti-de Sitter space can be captured by a non-gravitational conformal field theory (CFT) living on the boundary of that space. Since the duality maps strong coupling to weak coupling, it has frequently been used to probe the strong coupling dynamics of a CFT living at the boundary by solving a classical gravity problem in the bulk [78, 79]. To gain insight into quantum gravity, one would like to invert the direction of this logic and use the non-perturbative quantum dynamics of the CFT to infer aspects of bulk quantum gravity.

As a first step in this direction, one performs a Wick rotation on anti-de Sitter space to obtain hyperbolic space, followed by a discretization of the latter to obtain a lattice theory.

There have been recent efforts to perform classical simulations of such theories using Monte Carlo methods [80–83], tensor network methods [84–87] and other numerical techniques [88]. However such studies cannot probe the real-time dynamics of such systems, and

in this manuscript, we return to a simple toy model that can be *quantum* simulated directly in anti-de Sitter space – the transverse Ising model formulated in two-dimensional anti-de Sitter space (AdS_2).

In this chapter we will study this model using exact diagonalization, tensor network methods, noiseless quantum simulators, and simulation on superconducting quantum devices. Since the boundary theory is conformal quantum mechanics, a prime focus of our work will be time-dependent correlation functions and, in particular, so-called "out-of-time-ordered" correlators (OTOCs). These provide information on how fast quantum information can propagate through the lattice and how long thermalization takes in such an interacting quantum system.

Contrary to naive expectation it is possible for a quantum mechanical system to undergo thermalization *locally* [89, 90]. Indeed such thermalization has also been observed experimentally [91].

The key idea is that one needs to focus on a subset A of the composite system comprising A and its environment B. If A is entangled with B then one naturally obtains a density matrix for A by tracing out the degrees of freedom in the Hilbert space of B. If $|\psi\rangle\langle\psi|$ denotes a pure state of the combined system, the density matrix of A is given by

$$\rho_A = \mathrm{Tr}_{\mathcal{H}_B} |\psi\rangle\langle\psi| . \tag{4.1}$$

This density matrix corresponds to a mixed state if there is entanglement between A and B, and this is manifested by a non-zero entanglement entropy given by the von Neumann formula:

$$S = -\mathrm{Tr}_{\mathcal{H}_A} \rho_A \ln \rho_A. \tag{4.2}$$

In this paper, we are particularly interested in mixed states corresponding to thermal systems. One simple way to construct a thermal density matrix for A is to start from a

composite system comprising two identical copies of A

$$|\Psi\rangle = \frac{1}{Z^{\frac{1}{2}}} \sum_n e^{-\frac{\beta}{2}E_n} |n_A\rangle |n_B\rangle . \tag{4.3}$$

In this case, tracing out B yields

$$\rho_A = \frac{1}{Z} \sum_n e^{-\beta E_n} |n\rangle \langle n| , \tag{4.4}$$

in the case where the quantum mechanical system corresponds to a conformal field theory there is a holographic interpretation of the density matrix as describing a black hole in a dual geometry which contains the CFT on its boundary. Indeed the entanglement entropy in this case can then be shown to correspond to the Bekenstein-Hawking entropy associated with the area of the event horizon of the black hole [92–95].

The next most obvious question that arises is how long it takes to realize this density matrix under Hamiltonian evolution starting from some pure non-generic state $|\psi\rangle$. In general, this process resembles classical chaotic dynamics with initial states that differ only by small perturbations yielding radically different states at large times. This thermalization process is called scrambling and has been the focus of many previous studies [96–106]. The scrambling time τ_S is determined by the speed at which information can propagate across the system under time evolution and is related to the dimensionality of the system and the locality of the Hamiltonian. There are theoretical bounds on the scrambling time τ_S which is bounded from below by

$$\tau_S \sim \beta \ln V,$$

where, V counts the number of microscopic degrees of freedom. Attaining this bound depends on an exponentially fast spread of information through the system [107–111].

It has been conjectured that CFTs with black hole duals provide one example of a system capable of such “fast scrambling" [112, 113]. Systems that show fast scrambling typically

involve non-local Hamiltonians and all-to-all interactions such as the SYK model [114–118]. In this paper we will show that in certain regions of the parameter space the transverse quantum Ising model with nearest neighbor interactions living on a discretization of two dimensional anti-de Sitter space appears to exhibit similar behavior. However one should be careful with this interpretation – the spatial boundary of our system is just two points and our quantum spins populate the bulk space as well as the boundary. So we are primarily looking at information spread in the bulk. To understand the thermalization properties better one would need to extend the model to three dimensional anti-de Sitter space which possesses a non-trivial spatial boundary.

We have performed both classical and quantum simulations of this system. In Sec. 4.2, we find the ground state of this model using the density matrix renormalization (DMRG) algorithm [119–121] and time-evolve it with the time evolving block decimation (TEBD) algorithm using the ITensor library [122–125]. In Sec. 4.3, real time evolution of the magnetization is discussed and implemented for a thirteen qubit system and compared to the tensor method results. We discuss the information propagation in this model in Sec. 4.4. To study the scrambling properties of the model we have used matrix product operator (MPO) methods to calculate the OTOCs [126, 127] in Sec. 4.4.1. In the next subsection 4.4.2, the computation of OTOCS using a protocol developed by Vermersch et al. [128] is discussed and implemented for a model with seven qubits. Successful implementation of the model on quantum devices required applying some additional error mitigation techniques. We discuss the influence of the mitigation techniques on the results and other numerical aspects of the digital quantum simulation in Appendix 4.6. We also sketch out how to implement this Hamiltonian via analog quantum devices like Rydberg arrays and perform simulations of the system on the Bloqade simulator developed by QuEra in Sec. 4.3.2. In Appendix 4.7, we include some details of the protocol used for the computation of the OTOC using a quantum computer.

4.2 Transverse Ising Model on a Hyperbolic Space

In this section, we describe the Transverse Field Ising (TFI) model formulated on a one dimensional hyperbolic space. The model is an analogue of the classical Ising model on a two dimensional tessellation of hyperbolic space [129, 130]. The Hamiltonian that describes this Ising chain can be represented as a sum of local terms [131–133]

$$\hat{H} = \frac{-J}{4} \sum_i \frac{\cosh(l_i) + \cosh(l_{i+1})}{2} \sigma_i^z \sigma_{i+1}^z + \frac{h}{2} \sum_i \cosh(l_i) \sigma_i^x + \frac{m}{2} \sum_i \cosh(l_i) \sigma_i^z. \tag{4.5}$$

Here, σ_i^p is a local Pauli operator at site i with $p = \{x, y, z\}$. The first term corresponds to a nearest neighbour interaction term coupling neighboring sites. The deformation factors $\eta_i = \cosh l_i$ arise from the metric of Euclidean AdS_2 given in Eq. (4.6) and give rise to a site-dependent coupling for the Ising chain

$$ds^2 = \ell^2(\cosh^2(\rho) dt^2 + d\rho^2). \tag{4.6}$$

For an N site lattice the site-dependent deformation scale l_i is given by

$$l_i = -l_{\max} + i \frac{2 l_{\max}}{N-1}, \tag{4.7}$$

where $l_{\max}$ denotes a length scale that determines the degree of deformation. In the limit of $l_{\max} \to 0$, the planar transverse Ising model is recovered. In the rest of the paper we will be using system sizes where N is a odd number. This ensures that there is a true middle point where the coupling is symmetrical which ensures the dynamics of propagation are same towards to the left and right of this middle point. Obviously, for infinite chain limit $N \to \infty$, the distinction between choosing odd or even number of site will disappear.

We start the discussion of our numerical results with the von Neumann entropy Eq. (4.2) calculated from the reduced density matrix obtained by dividing the spin chain in two and tracing out one half. Fig. 4.1 shows a plot of the half chain entropy and Fig. 4.2 shows the magnetic susceptibility at $l_{\max} = 3.0$ $h = 3.0$ and $m = 0.25$ using $N = 37$ spins as a function of J.

For our DMRG calculation we used 50 sweeps of the chain with a cutoff of order $\epsilon = 10^{-12}$ which resulted in a bond dimension of order $\chi = 10$ on average. We see that there are peaks in the entropy and the susceptibility signaling a possible phase transition in the model. In our later work on OTOCs we will always tune our couplings to be close to their critical values.

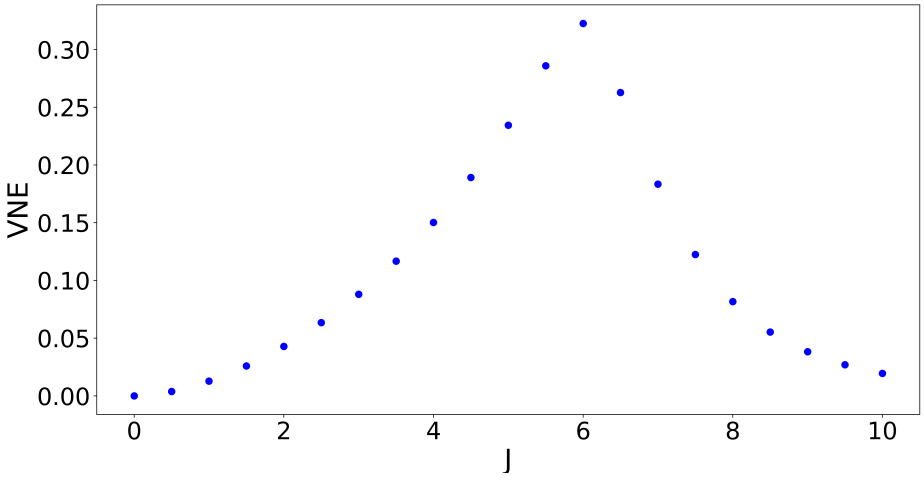

Figure 4.1: von Neumann Entropy versus J for $N = 37$, $l_{\max} = 3.0, h = 3.0, m = 0.25$.

4.3 Time evolution of the magnetization

In this section, we show results on the time evolution of the magnetization $\langle S^z \rangle = \frac{1}{2}\langle \sigma^z \rangle$ computed using tensor methods compared with simulation on quantum devices.

We start by time evolving the system using the Time Evolving Blocked Decimation (TEBD) algorithm [134]. Historically, TEBD was adapted from the Suzuki-Trotter approx-

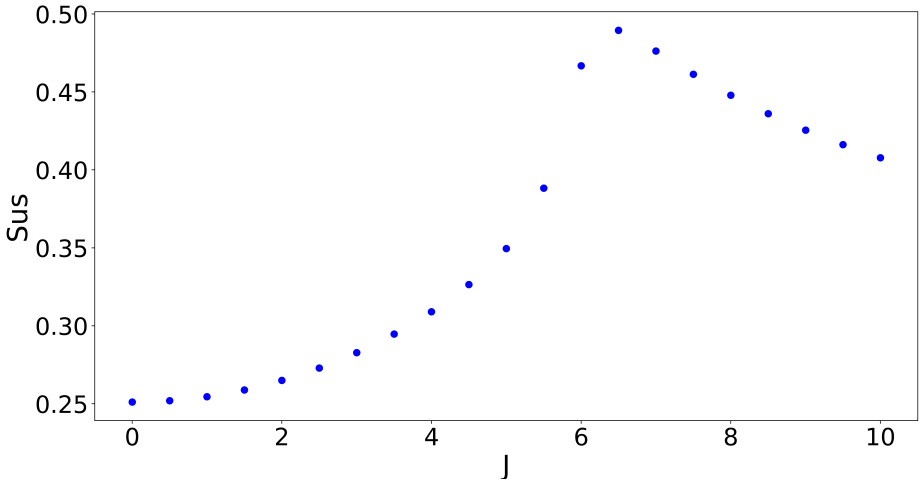

Figure 4.2: Magnetic susceptibility versus J for $N = 37$, $l_{\max} = 3.0, h = 3.0, m = 0.25$.

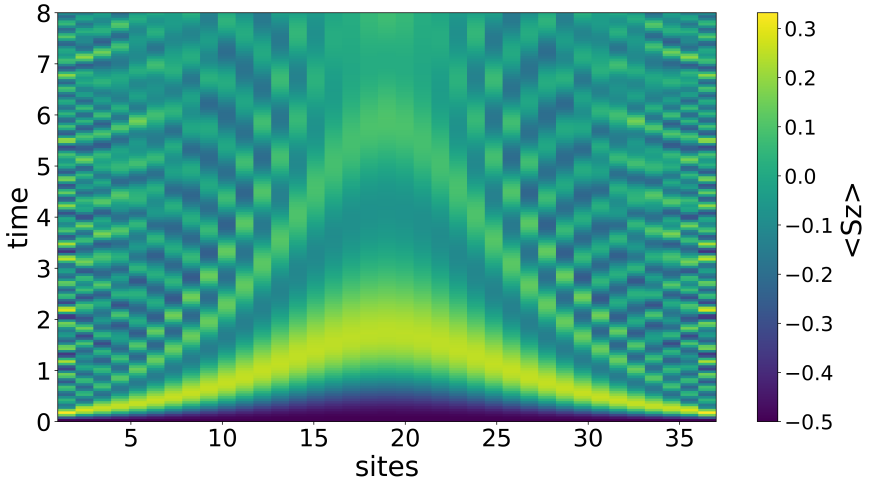

Figure 4.3: $\langle S^z \rangle$ for a lattice with $N = 37$ spins and parameters set at $J = 2.0, h = 2.0, m = 0.25, l_{\max} = 3.0$.

imation for the Matrix Product State (MPS) [135]. In Fig. 4.3, the Trotter evolution of the magnetization $\langle S_i^z(t) \rangle$ is plotted at each lattice site i for a lattice chain with $N = 37$ sites, and $l_{\max} = 3.0$, $h = 2.0$, $J = 2.0$, and $m = 0.25$ starting with all spins in the down state. Clearly, the dynamics of the magnetization shows warping effects in the bulk due to the curved background. One can think of this warping effect as due to time dilation effects in the bulk.

4.3.1 Time evolution of Magnetization with Universal Quantum Computers

Next, we attempt to investigate the model using a quantum platform – namely the IBM Guadalupe machine. Currently, quantum devices experience both large coherent and incoherent noise in any given computation. Thus, we have attempted to investigate a system with modest system size of $N = 13$ spins where there is limited device noise and the warping effects can be observed*. We have computed the time-dependent expectation value of the magnetization $\langle S_i^z(t)\rangle = \langle \mathbf{0}|U^\dagger(t)S_i^z U(t)|\mathbf{0}\rangle$, in the massless limit $m = 0$, using a first order Trotter approximation for the time evolution operator

$$U(t) = \exp(-iHt) \simeq \left(\prod_{i=0}^{N-1} R_x^i(\theta_i) \prod_{j=0}^{N-2} R_{zz}^j(\phi_j)\right)^n . \tag{4.8}$$

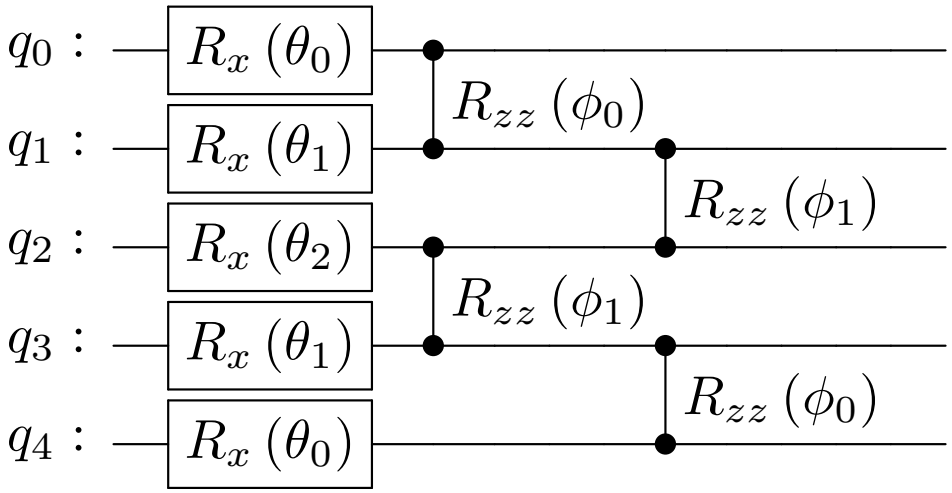

Figure 4.4: Trotter evolution circuit for the first Trotter step for a 5-Qubit spin chain in the hyperbolic lattice. Here, $\theta_i = -\frac{J\delta t}{4}(\eta_i + \eta_{i+1})$ and $\phi_i = h\delta t\eta_i$.

Using first order trotter evolution we can measure observables at discrete steps δt of time.

*IBM Guadalupe is a 16 qubit machine, where the longest possible chain of Ising spin that can be constructed without additional SWAP gates is of 13 qubits due to the connectivity constraints.

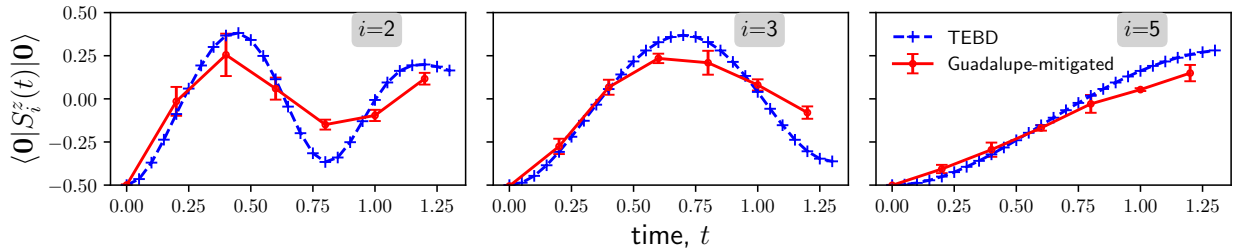

Figure 4.5: Local magnetization $\langle S_z^i(t)\rangle$ at site i for TFI model on hyperbolic lattice chain with 13 lattice sites. Parameters: $J = 2.0$, $h = 1.05$, $l_{\max} = 3.0$. We took advantage of the symmetry of the lattice Hamiltonian to find the average magnetization: $\langle S_i^z\rangle \to (\langle S_i^z\rangle + \langle S_{N-i}^z\rangle)/2$. This played an important role since some of the physical qubits of the Guadalupe machine have smaller energy relaxation ($T1$) and dephasing($T2$) times.

The quantum circuit representation for the time-evolution operator for one Trotter step is shown in Fig. 4.4. We need to repeat the circuit n times to obtain time evolution operator at time $t = n\delta t$. Thus, n denotes the number of Trotter steps in the calculation. In general, the quantum circuit representation for the computation of observables involves initial state preparation, time-evolution, and measurement. Due to our choice of a simple initial state (vacuum state $|\mathbf{0}\rangle = |0\rangle^{\otimes N}$) and simple operator $S_z = \frac{\sigma_z}{2}$ we do not need any additional quantum operations for the initial state preparation and the measurements.

Different orderings of the operators can be used for this approximation, see the discussion in the Appendix 4.6.2. In this section, all the results presented use what we denote as 'odd-even' ordering in the Appendix.

Local magnetization results are shown for three different sites in the Fig. 4.5 and compared against classical simulation results obtained from TEBD. The parameters used were $J = 2.0$, $h = 1.05$ and $l_{\max} = 3.0$. The gate cost of such a circuit is similar to that of the Ising spin chain on a flat lattice [136]. The difference in our Trotter evolution of the deformed Hamiltonian lies in the site dependent phase factors of the rotation and entangling gates. This brings an inherent complication to the problem of selecting the optimal Trotter step δt. Previous studies have shown that theoretical bounds of the first-order Trotter approximation can be relaxed for observing time evolution with current NISQ-era machines [136–138]. The phases (θ_i, ϕ_i) of the rotation and entangling gates are of the form $C_i \times \delta t$ and the optimal

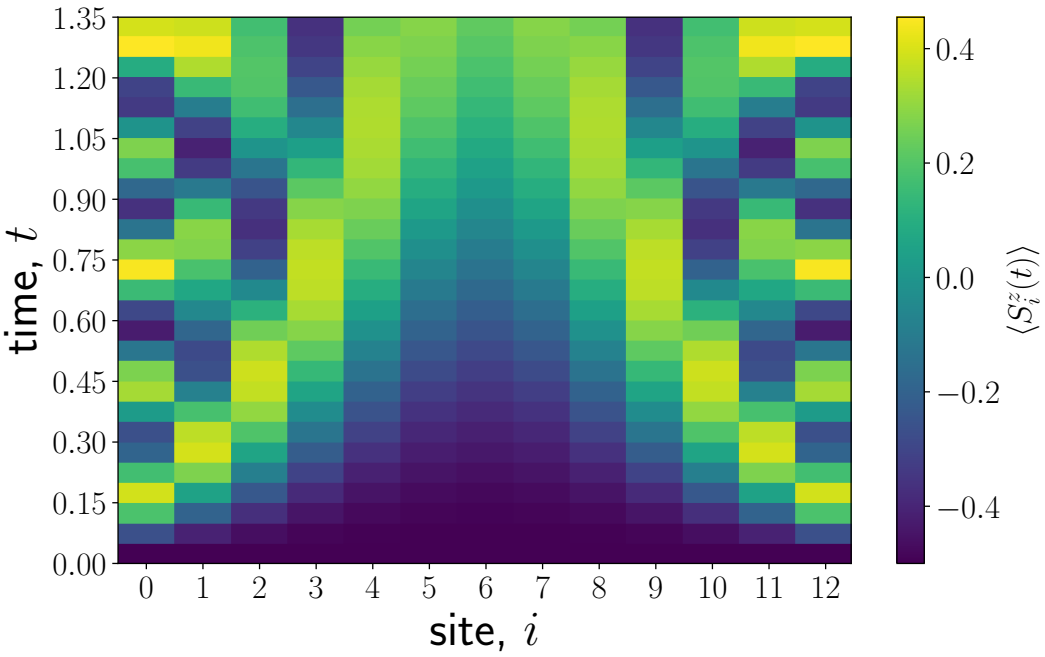

Figure 4.6: Trotter evolution of local magnetization $\langle S_i^z(t)\rangle$ with exact diagonalization. Parameters: $N = 13$, $J = 2.0$, $h = 1.05$, $l_{\max} = 3.0$.

choice for the Trotter step is different for local operators $\langle S_z^i\rangle$ at different sites. Thus, one constraint for choosing the optimal Trotter step $(\delta t)_{\text{optimal}}$ comes from the local couplings C_i. In NISQ-era devices, the other constraint comes from the maximum possible circuit depth $d_{\max}$ that can be simulated before the noise swamps the signal. Naively, we can use a maximum of $d_{\max}$ number of q-qubit gate before the information is completely lost

$$d_{\max} = \frac{\ln(1/2^q)}{\ln(\epsilon)},$$

due to the accumulation of gate errors of size ϵ. In practice, the practical circuit depth $d_{\text{practical}} << d_{\max}$ due to different sources of noise other than the gate errors. Hence we can not go beyond a maximum number of $n_{\max}$ Trotter steps in current devices. We found that a value of $(\delta t)_{\text{optimal}} \sim 0.2$ and $t_{\max} \sim 1.2$ is a good choice for time evolution of the magnetization. To see key features of an observable the optimal choice of the trotter step can depend on the type of the observable, and the parameters $(J, h, m, l_{\max})$. For the computation

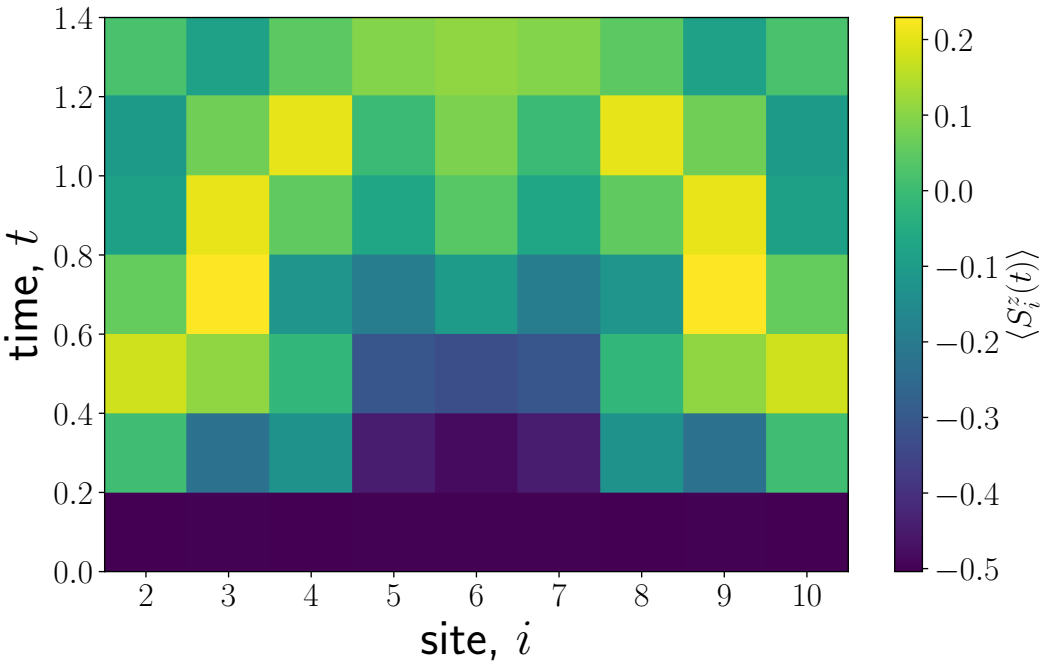

Figure 4.7: Trotter evolution of local magnetization $\langle S_i^z(t)\rangle$ computed using guadalupe Quantum Processing Unit (QPU). Parameters: $N = 13$, $J = 2.0$, $h = 1.05$, $l_{\max} = 3.0$. Magnetization data on the edges of the lattice chain are omitted due to the large Trotter-error associated with it. Note that the deformation strength is stronger on the edges.

of the local magnetization, the number of shots used is $N_{\text{shots}} = 1000$. See Appendix. 4.6.1 for a discussion of the statistical noise associated with different N_{shots}.

In Fig. 4.5, classical simulation results of the local magnetization with the TEBD algorithm are compared with the mitigated results obtained from the Guadalupe machine. The error-bars in the figures represent statistical errors associated with six different measurements. The measurements were performed on different days to demonstrate reliable systematic error on the current devices. Various error mitigation techniques were applied to obtain the results.

Dynamical Decoupling (DD) [139, 140] was applied to reduce the coherent noise and the M3 method [141] was used to reduce readout errors. We also created noise-scaled circuits with three-fold and five-fold amplification of the noise in comparison to the original circuit and applied the Zero Noise Extrapolation (ZNE) mitigation technique to reduce the inco-

herent noise [142, 143]. We used the built-in features of the IBM runtime system to apply DD and M3 while noise-scaled circuits were created by inserting an appropriate number of identity operators for each CNOT gate. This choice is justified for current IBM devices, where two-qubit gates have significantly larger errors than single-qubit rotation gates[†]. See Appendix. 4.6.3 for the discussion of how different error mitigation techniques improved our results.

After post-processing the data with different error mitigation techniques, we found that the magnetization results obtained from the Guadalupe machine Fig. 4.7 show good evidence of the warping expected for this geometry. For comparison purposes, the TEBD results are plotted in Fig. 4.6. The CNOT gate cost for computing time-evolution with first order Trotter approximation of a N-qubit quantum spin chain is $2(N-1)$ per Trotter-step and the circuit depth at Trotter step $n = 6$ is $d = 48$. The results from the QPU track the peak of the local magnetization quite well. The QPU results also demonstrate that the initial state with all-down spins is disrupted by the boundary at a slower rate as we move from the edge to the center of the lattice chain. While the quantum simulation results align qualitatively with tensor methods, it is clear that larger numbers of qubits would be needed to identify the warping effects in a greater detail. We have also explored a possible implementation of the real-time magnetization evolution on QuEra's analog quantum computers based on Rydberg arrays which can be seen in the next subsection.

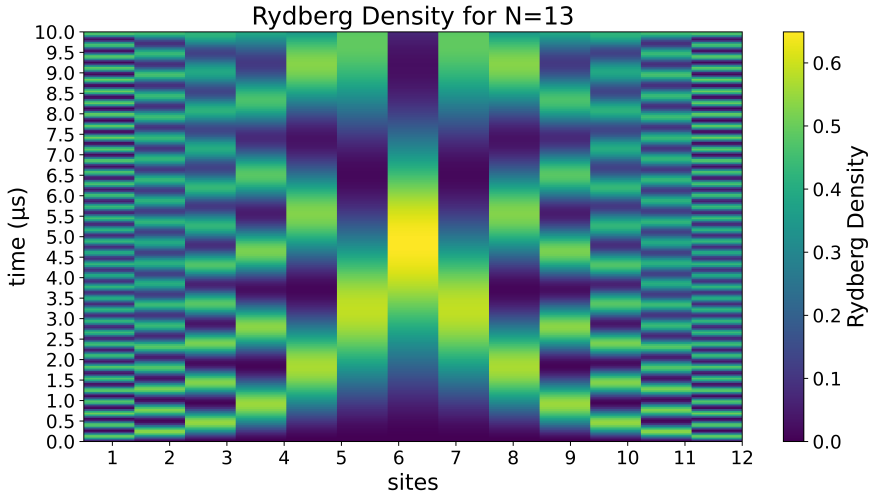

Figure 4.8: Time evolution of the Rydberg density

4.3.2 Magnetization results using Rydberg Arrays

In this subsection, we report on quantum simulations of this model using Rydberg arrays. The Hamiltonian that governs the Rydberg simulator can be written as,

$$\hat{H}_R(t) = \sum_j \frac{\Omega_j(t)}{2}(e^{i\phi_j(t)} |g_j\rangle \langle r_j| + e^{-i\phi_j(t)} |r_j\rangle \langle g_j|) - \sum_j \Delta_j(t)\hat{n}_j + \sum_{j<k} V_{jk}\hat{n}_j\hat{n}_k, \tag{4.9}$$

where, $\Omega_j(t)$ is the Rabi frequency, $\phi_j(t)$ denotes the laser phase, $\Delta_j(t)$ the detuning parameter at site j. Van der Walls interaction $V_{jk} = C_6/|r_j - r_k|^6$ is known as the Rydberg interaction term with $C_6 = 2\pi \times 862690\text{MHz}\mu\text{m}^6$ [144–146].

Different operators in the hyperbolic Ising Hamiltonian can be mapped to different op-

[†]For the Guadalupe machine, the ratio of the median-errors for the two-qubit and single-qubit gates is $\frac{\epsilon_{\text{CNOT}}}{\epsilon 1 qubit-gate} \sim 25$.

erators of the Rydberg Hamiltonian with the choice of zero laser phase $\phi_j(t)$ at all sites,

$$\hat{H}_R(t) = \sum_j \frac{\Omega_j(t)}{2} \underbrace{(|g_j\rangle\langle r_j| + |r_j\rangle\langle g_j|)}_{\sigma_j^x} - \sum_j \Delta_j(t) \underbrace{\hat{n}_j}_{(1-\sigma_j^z)} + \sum_{j<k} V_{jk} \underbrace{\hat{n}_j\hat{n}_k}_{(1-\sigma_j^z)(1-\sigma_k^z)} . \tag{4.10}$$

The Rydberg interaction potential, V_{jk} determines the position of the atoms to quantum simulate the hyperbolic Hamiltonian. Due to the hyperbolic deformation, it is expected that we need to position the atoms non-uniformly. This is achieved by placing the atoms starting at location $(0, 0)$ and using Eq. (4.11) to find the distances between successive spins:

$$\delta_{i+1} = (A/\eta_i)^{1/6} + r_i. \tag{4.11}$$

This equation is just the rearranged form of $\frac{A}{(r_{i+1}-r_i)^6} = \cosh l_i$ which is the form of the Rydberg potential. Here, $A = 2\pi \times 512$ is a constant for adjusting the scale, $\eta_i = J\cosh(l_i)$ is the hyperbolic deformation and r_i is the location for the i_{th} site. We set $J = 1$ for the rest of our discussion of Rydberg simulations.

Using this procedure we get the following locations for the Rydberg atoms for $l_{\max} = 3.0$ where the resulting distances between atoms range from 12.13µm, to 17.72µm with the furthest atom located at 180.77µm from the origin.

The form of Δ_j and Ω_j is then given by equating the coefficients to the form of the Rydberg potential between the atoms

$$\Delta_j = \Omega_j = \frac{10 \times C_6}{(r_{j+1} - r_j)^6}. \tag{4.12}$$

However, currently commercially available Rydberg machines are constrained to have only global laser parameters. Hence we have turned to the Bloqade Simulator developed by QuEra to perform simulations [147]. Fig. 4.8 shows a picture of the time evolution of the

Rydberg density (essentially $\langle S_z \rangle$). Notice that Fig. 4.8 exhibits similar warping effects to those seen in the TEBD simulations of the model. This shows us that our model can be simulated with Rydberg Arrays. We hope that in the future with advancements in the Rydberg array technologies, we will be able to probe information propagation in this model with Rydberg simulators. However even with a local detuning it might not be possible to probe the whole spectrum of the model due to limitations in chain length and largeness of the Rabi and detuning term.

4.4 Out-of-time-ordered Correlators

We now turn to the question of how information spreads in the model. To answer that, we computed an out-of-time-ordered-correlator (OTOC). This observable is known to capture information spread and scrambling in quantum systems [148–151] and can be thought of as a quantum mechanical counterpart of the Loschmidt echo [152]. To construct the OTOC, we use two operators $W_i(t)$ and V_j where $W(t) = \exp^{iHt} W(0) \exp^{-iHt}$. From these we construct the commutator of these operators

$$C(t) = \langle ||[W_i(t), V_j]||^2 \rangle = 2(1 - \mathrm{Re}[F_{ij}(t)]), \tag{4.13}$$

where $F_{ij}(t)$ is the the required out of time ordered correlator (OTOC)

$$F_{ij}(t) = \langle W_i(t)^\dagger V_j(0)^\dagger W_i(t).V_j(0) \rangle. \tag{4.14}$$

This equality is obtained under the assumption that W and V are unitary and that terms that correspond to local observables thermalize to a constant after a short time and hence can be omitted. The connection between $F_{ij}(t)$ and the information spread can be made clear by considering W as a simple local perturbation. Under time evolution this perturbation becomes more and more non-local. The growth of these non-local effects can be captured

by calculating the commutator of $W(t)$ with another local operator V. When the operators commute, C vanishes and F is one. So by measuring the double commutator or the OTOC we can track the propagation of $W(t)$ along the system.

The relationship between the double commutator and operator growth can be made clear by considering a simpler setup. Let's start by representing a unitary time evolution operator out of local two qubit unitaries. Using this representation we can obtain the Heisenberg time evolution for a local operator $A(t) = U^\dagger A U$.

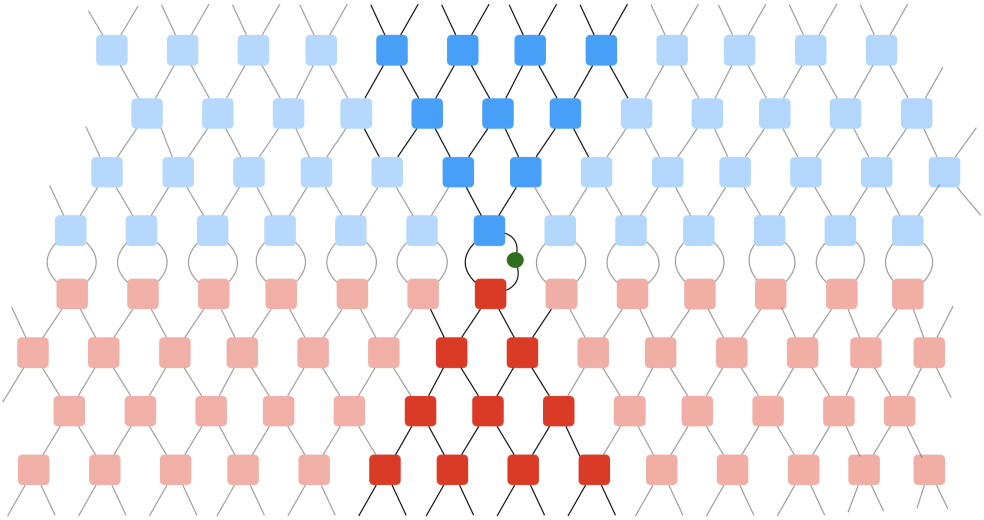

Figure 4.9: Heisenberg time evolution for a local operator.

Where in Fig. 4.9 blue and red boxes represent $U^\dagger$ and U while the green circle represents the operator A. One can clearly see from the above figure that any contraction that doesn't involve the operator A will be the identity so we can ignore those and focus on the contractions that involve the operator. This clearly shows us the lightcone for the operator growth in the Heisenberg picture and demonstrates that the OTOCs capture the characteristics of the operator spread in the system.

However, this general form of the OTOC is not the easiest to deal with in our simulations. Instead, we choose the following form for the OTOC operator which can be seen from Eq. 4.15

[128, 153]

$$O_i(t) = \frac{\mathrm{Tr}(\rho W(t)^{\frac{N+1}{2}} V_i^\dagger W(t)^{\frac{N+1}{2}} V_i)}{\mathrm{Tr}(\rho W(t)^2 V^\dagger V)}. \tag{4.15}$$

In our calculations, we take $W(t) = \sigma^z(t)$, $V = \sigma^z$ and fix the position of $W(t)$ operator at the center of the lattice chain. To see the effect of the interaction of two local operators, we then place the operator V at different lattice sites i. We have focused on the infinite temperature limit which corresponds to taking a density matrix $\rho \sim \mathbf{I}$ in Eq. 4.15. Infinite-temperature OTOCs bear the signature of entanglement growth after a quench is applied to an energy eigenstate [154] and are easier to compute. Furthermore, many of the protocols used in finite-temperature-OTOCs can be developed from the corresponding protocols used in the infinite temperature case [128, 155]. Additionally, the exponents computed from the infinite-temperature OTOCs are insensitive to slightly different OTOC definitions that exist in the literature, see the appendix in [155].

4.4.1 Classical Simulations of OTOCs

For computing the Out-of-Time-Ordered Correlators (OTOC) using classical methods, we utilize a Matrix product Operator (MPO) representation of the operators W and V. We consider Heisenberg time evolution representation of the W operator to obtain $W(t) = \exp(iHt)W\exp(-iHt)$ through the Time-Evolving Block Decimation (TEBD) algorithm. Fig. 4.10 illustrates the application of Heisenberg time evolution to a generic operator W for one Trotter step. In this figure, the blue blocks denote the MPO representation of the operator W, while the green blocks constitute the MPO representation of unitary evolution operator $e^{iH_{ij}\delta t}$, where i and j represent the neighboring site indices. Then the resulting time evolved operator $W(t)$ can be plugged into the OTOC calculation.

In the absence of deformation of the coupling paramters, the flat space transverse Ising model is recovered and a linear light cone is observed (Fig. 4.11). If we turn on the hyperbolic deformation by tuning $l_{\max}$ to a non-zero value, we observe that the system develops a warped

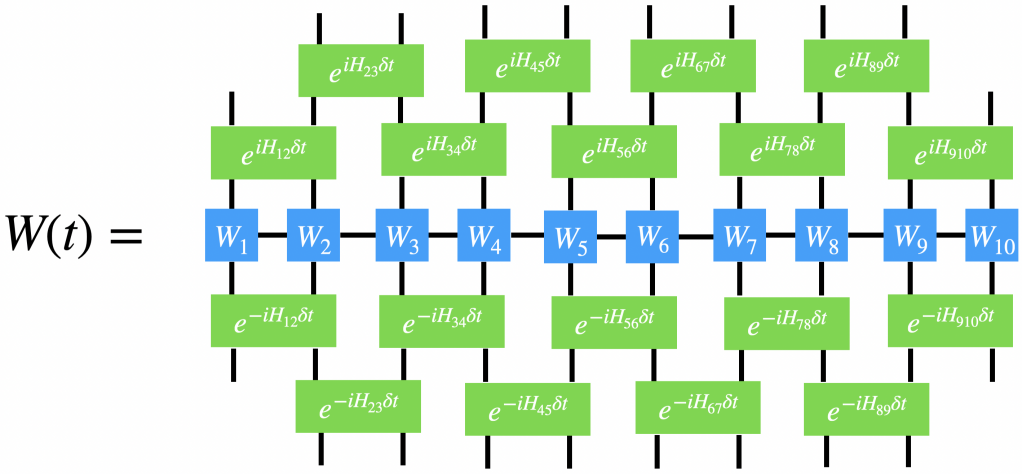

Figure 4.10: Heisenberg time evolution for an operator W(t).

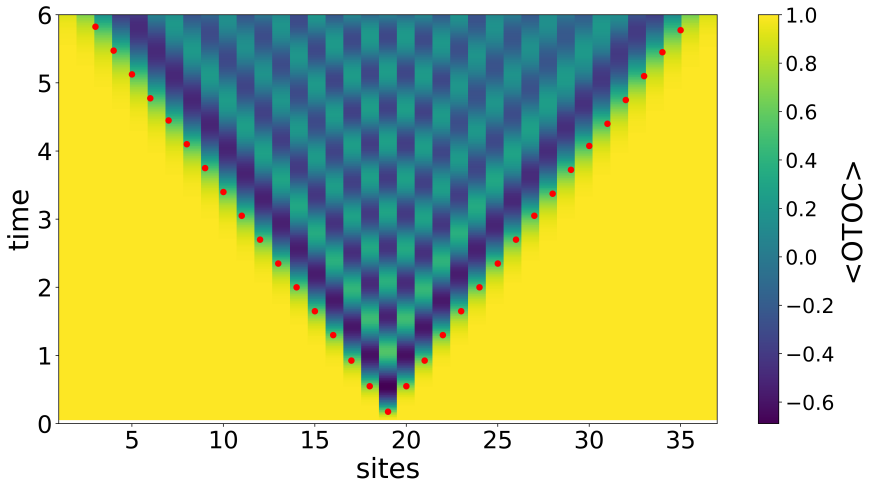

Figure 4.11: OTOC ($O_i(t)$) for the planar Ising model can be obtained by setting the deformation scale $l_{\max}$ to zero. Parameters: $J = 6.0$, $h = 3.05$, $m = 0.25$.

lightcone. In Fig. 4.11, Fig. 4.12 and the rest of the plots of OTOCs, the red dots in the out of time ordered correlator plotsrepresent the times where the OTOC at that lattice site first deviates from 1.0 by some amount $\epsilon = 0.25$. These resultant points trace out the lightcone shown in the plot. The purple line which is shown to guide the eye corresponds to a curve of the form

$$t = \log \left| x - \frac{N+1}{2} \right| + B,$$

where, B is a constant.

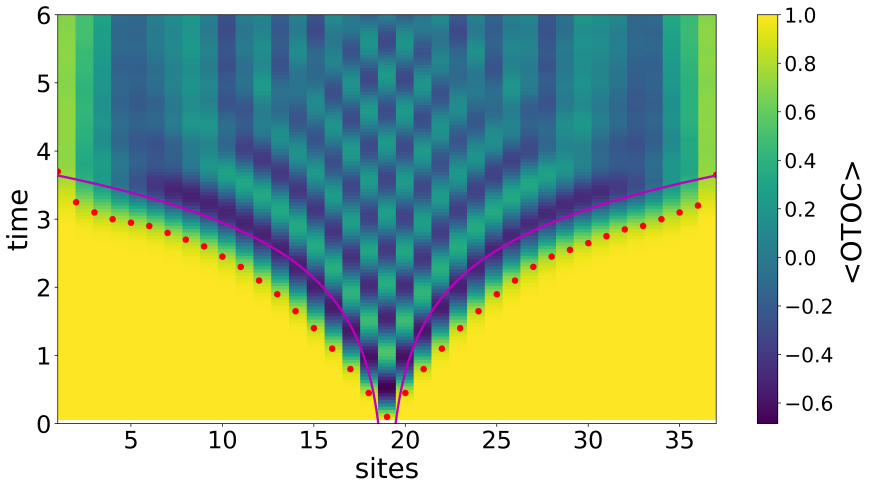

Figure 4.12: OTOC ($O_i(t)$) in the hyperbolic Ising model. Parameters: $l_{\max} = 3.0$, $J = 6.0$, $h = 3.05$, $m = 0.25$.

We found that to access the logarithmic regime of the model the physical couplings J and h need to be tuned to be close to their critical values. The remaining physical coupling m then controls the thermalization dynamics. In Fig. 4.14 we plot the time evolution of the half-chain von Neumann entropy which shows how m controls the thermalization. We can also look at the site-averaged OTOCs which are plotted in Fig. 4.13. This clearly show a power-law dependence on t as the system thermalizes.

Note that the value of m doesn't affect the structure of the light cone and only controls the thermalization time. In fact the shape of the lightcone is determined by the value of $l_{\max}$. For $N = 37$ we found four distinct behaviors for the lightcone. For $0.0 < l_{\max} < 1.0$ we find a linear lightcone. Then for $1.0 < l_{\max} < 2.0$ we see a power-law behavior while for $2.0 < l_{\max} \leq 3.0$ the light cone takes on a logarithmic behavior. Finally for $l_{\max} > 4.0$ the system confines and an excitation that has been initialized in the bulk never reaches the boundaries of the chain. We summarize this structure in the cartoon of the OTOC phase diagram of the model in Fig 4.15 and more figures that show these distinct propagation patterns can be seen in Appendix. 4.8

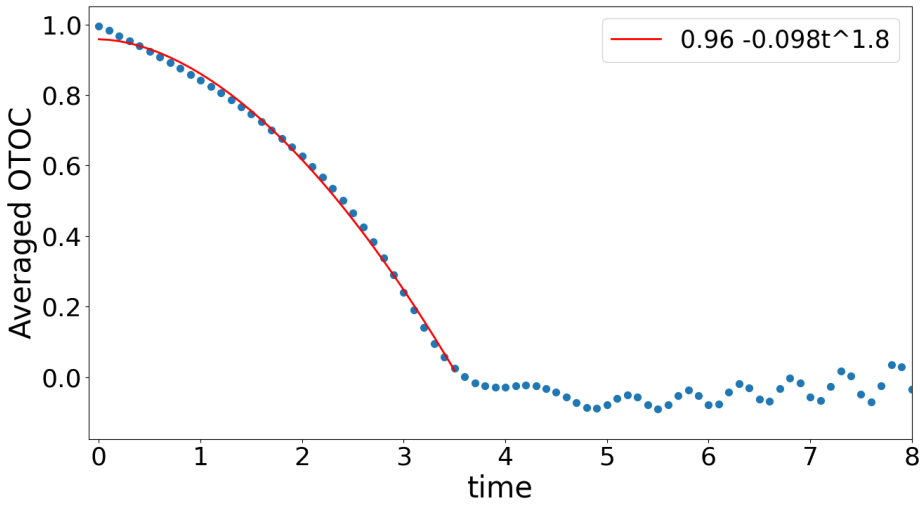

Figure 4.13: Site averaged OTOC for $J = 6, h = 3.05, m = 0.25, l_{\max} = 3.0$

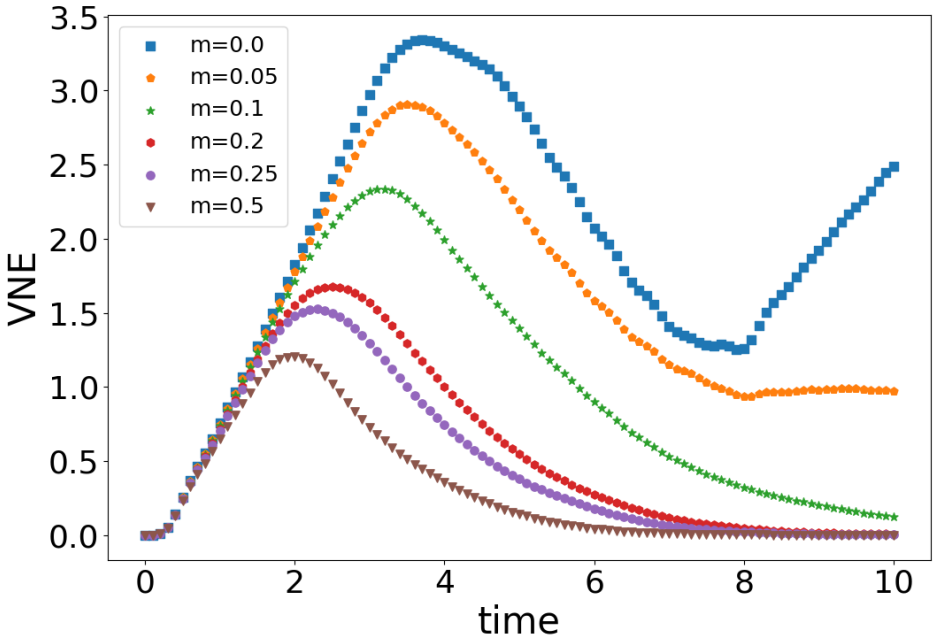

Figure 4.14: von Neumann entropy for $J = 6, h = 3.05, l_{\max} = 3.0$

The dependence on $l_{\max}$ can be clearly seen in Fig.4.16 where we plot the local light-cone time obtained from OTOC calculations vs the lattice site, starting from the middle of the chain and ending at the first site. The black curves show the logarithmic fits for $l \geq 3.0$. Error bars on the points are obtained by taking multiple cutoff values and averaging over

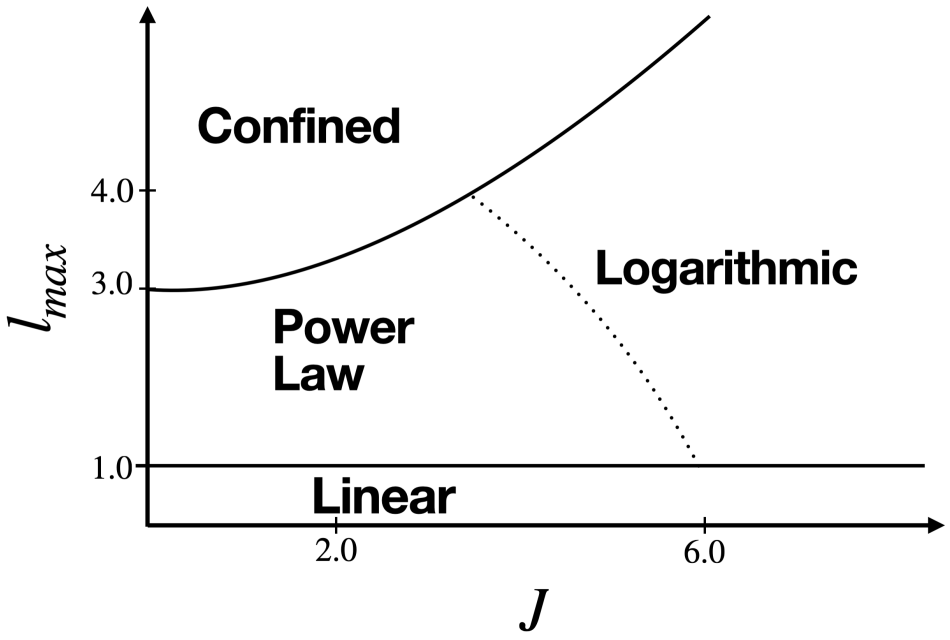

Figure 4.15: OTOC Phase Diagram for $N = 37$ lattice spins.

them.

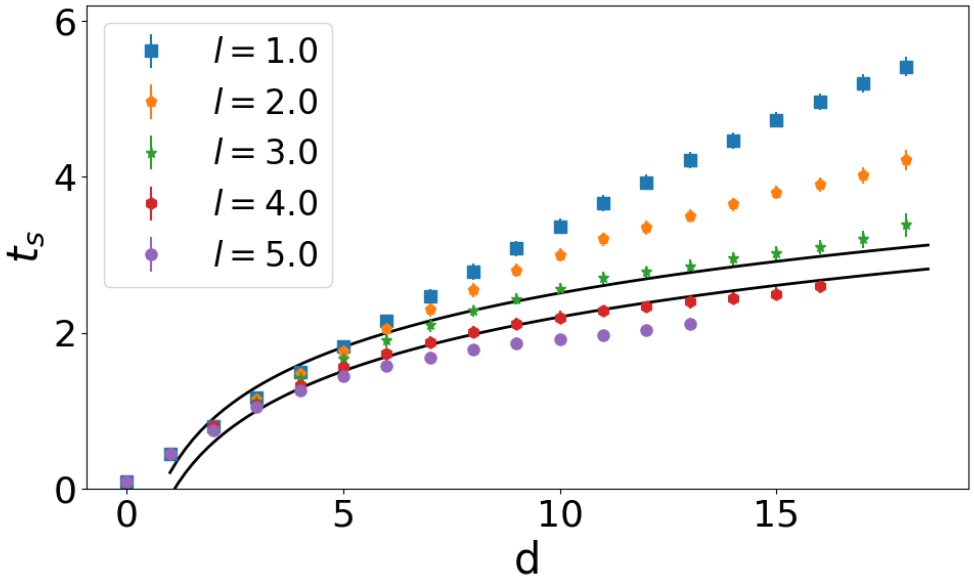

Figure 4.16: Curvature dependence of the propagation behavior of OTOC for $N = 37, J = 6.0, h = 3.05, m = 0.25$

Even though we focused solely on the choice of $W(t) = \sigma^z(t)$ and $V = \sigma^z$ for the

OTOC calculations, it is possible to choose other combinations of operators. One such choice corresponds to taking σ^x operators for both $W(t)$ and V operators which results in the plot shown in Fig. 4.17. We observe the shell-like structure of the XX-OTOC which is similar in behavior with the flat-space transverse Ising model analyzed by Lin and Motrunich in [149]. As can be seen from the Fig. 4.17, the points inside the light cone are significantly less prominent as compared to their ZZ-OTOC counterparts. The authors attributed this behaviour to the commutation structures of the time evolved operators [149].

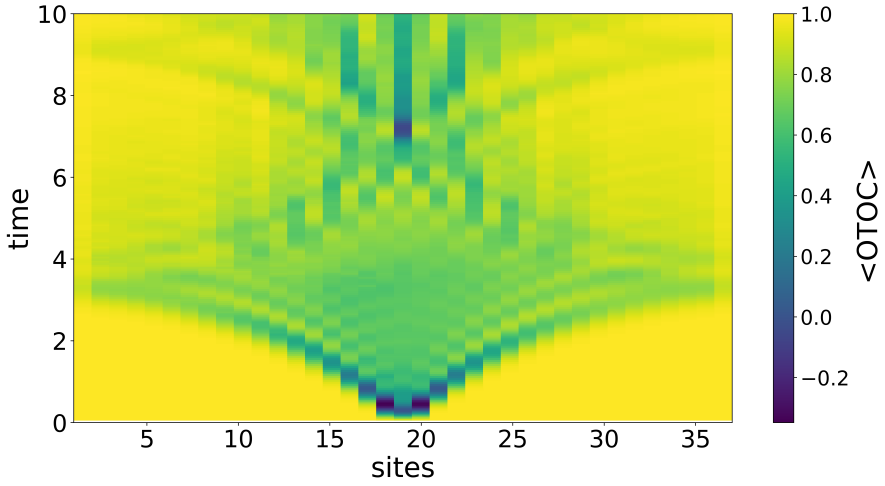

Figure 4.17: XX-OTOC for $N = 37, J = 6.0, h = 3.05, m = 0.25$

4.4.2 Quantum Simulation of OTOCs

In this subsection, the computation of the OTOC with digital quantum computers is discussed. First, let us write down an alternative definition of the OTOC for a N-qubit system

$$O_i^{\text{eig}}(t) = \frac{\langle\psi| \left(W(t)_{\frac{N+1}{2}} V_i^\dagger W(t)_{\frac{N+1}{2}} V_i\right) |\psi\rangle}{\langle\psi| \left(W_{\frac{N+1}{2}}(t)^2 V_i^\dagger V_i\right) |\psi\rangle}, \tag{4.16}$$

where $|\psi\rangle$ represents an arbitrary state. The schematic circuit diagram to compute this quantity is shown in the Fig 4.18. From this schematic diagram and the discussion of the Trotter evolution in the previous section, it is evident that to compute the OTOC with

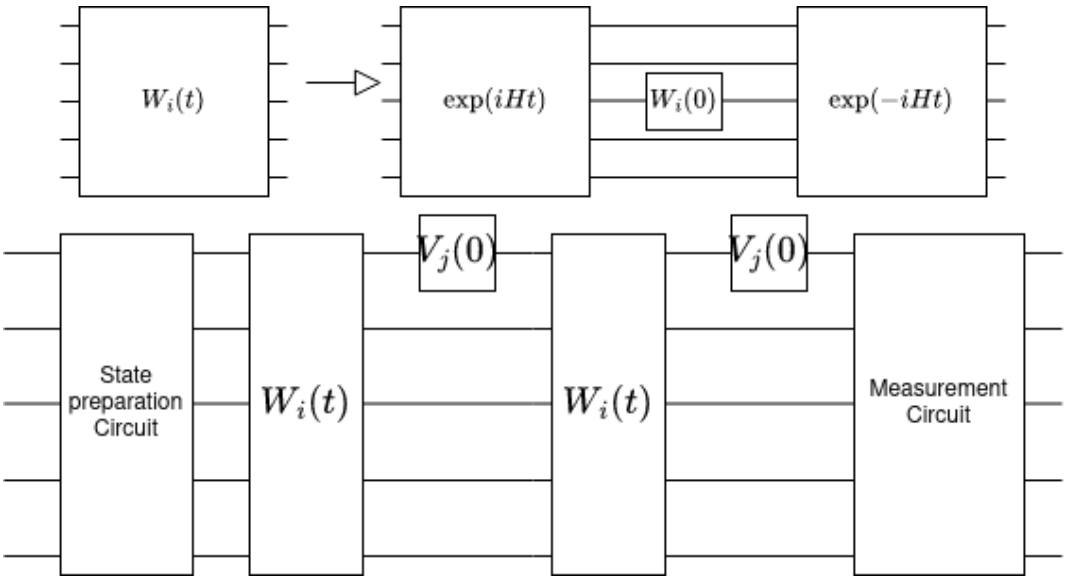

Figure 4.18: Schematic circuit diagram of OTOC using the definition at Eq. (4.16).

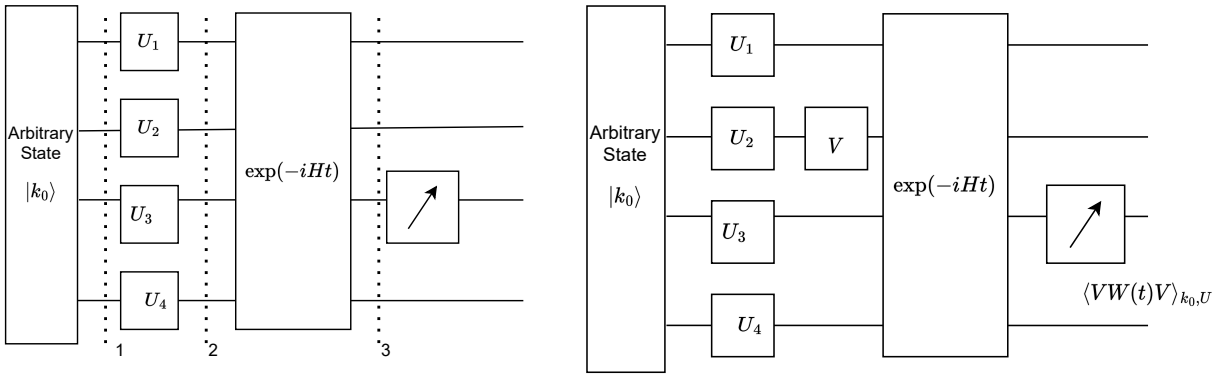

Figure 4.19: Modified OTOCs are computed from the correlation of the measurement of two different operators (a) $\langle W(t)\rangle$ and (b) $\langle V^\dagger W(t)V\rangle$. The same set of unitaries are required to find the correlation between the measurements. The procoess is repeated for many different sets of unitaries.

Trotterized evolution operator requires $8n(N-1)$ CNOT gates for the $\mathrm{n_{th}}$ Trotter step. In our work we considered a spin chain of length $N = 7$, and used a trotter step $\delta t = 0.5$ up to a maximum time $t_{\max} = 3.5$. This indicates that a quantum computation of the OTOC with a quantum circuit like that of Fig. 4.18 would require more that 200 CNOT gates in just four Trotter steps. Hence extracting any useful results would become impossible at early times due to coherent and incoherent noise in the device. Using a weaved Trotterization technique,

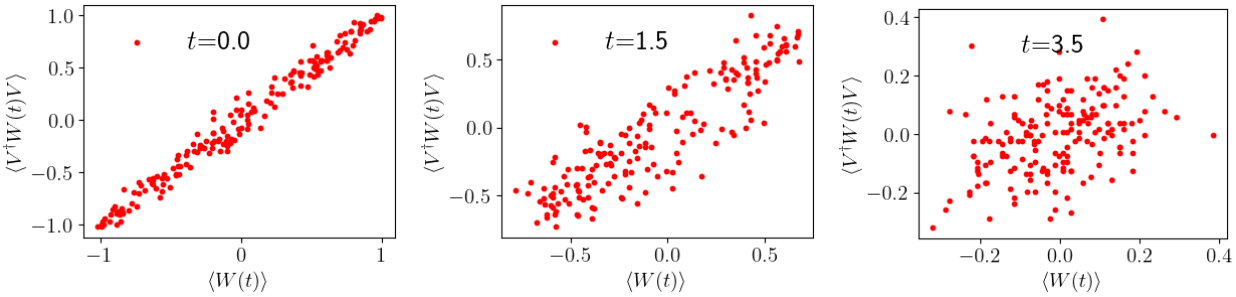

(a) (b) (c)

Figure 4.20: Change in correlation of the operators $\langle W(t)\rangle = \langle \sigma_3^z(t)\rangle$ and $\langle VW(t)V\rangle = \langle \sigma_2^z\sigma_3^z(t)\sigma_2^z\rangle$ over time. Parameters: $l_{\max} = 3.0$, $J = -0.5$, $h = -0.525$, $W(t) = \sigma_3^z(t)$, and $V = \sigma_2^z$.

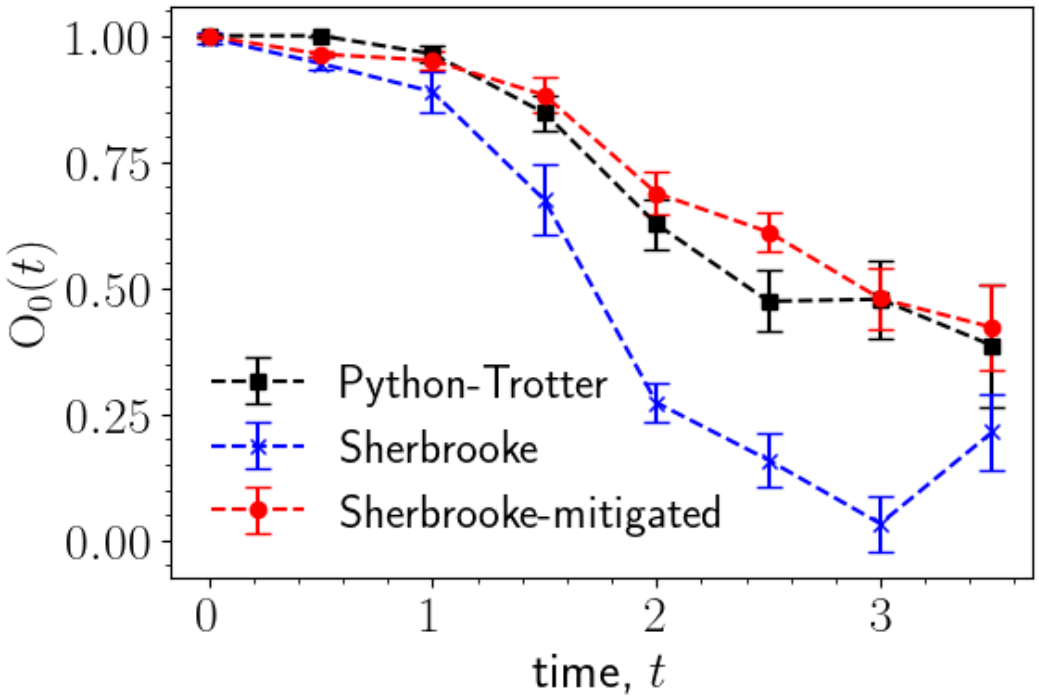

Figure 4.21: Modified OTOC of the zeroth order, $O_0(t)$ for $l_{\max} = 3.0$, $J = -0.5$, $h = -0.525$, $W(t) = \sigma_3^z(t)$, and $V = \sigma_2^z$.

similar circuits were implemented to compute OTOCs for a small system of four qubits in [156].

Our goal in this section is to investigate if we can extract the scrambling time at infinite temperature ($\rho \propto \mathbf{I}$) with the current IBM devices for a system with 7 spins. As for tensor network simulations we position the W operator at the center of the lattice chain and vary

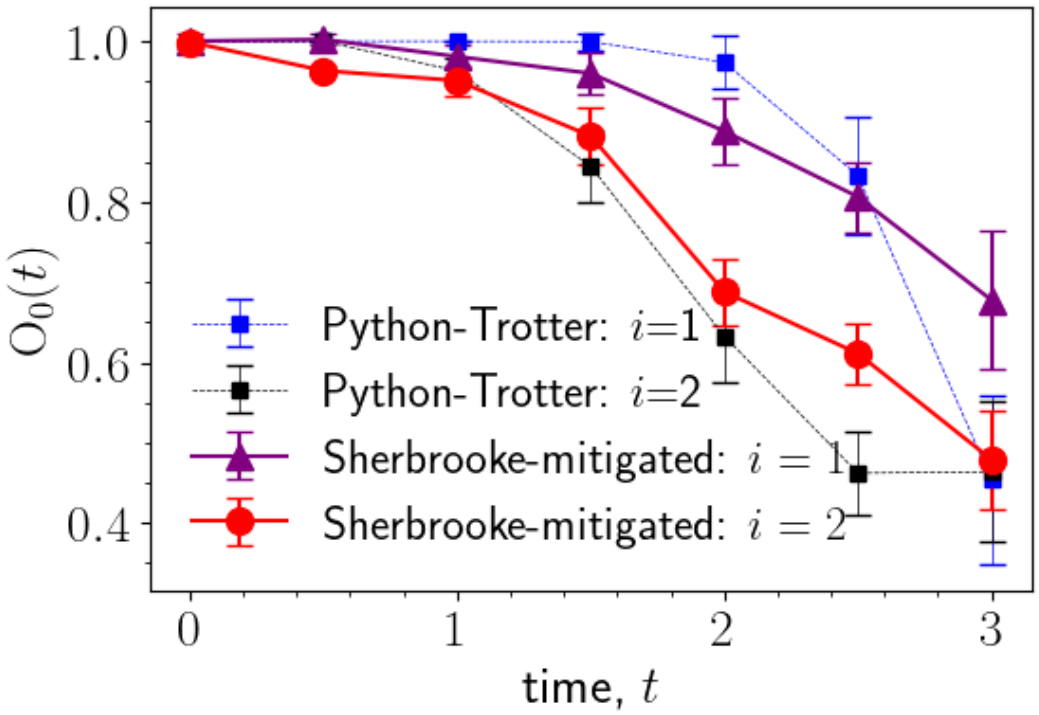

Figure 4.22: Modified OTOC as the position i of the V operator varies. Parameters: $l_{\max} = 3.0$, $J = -0.5$, $h = -0.525$, $W(t) = \sigma_3^z(t)$, and $V = \sigma_i^z$.

the position i of the V operator. Our choice for the W and V operators remains the same as that of the previous section. With quantum simulation, we also would like to see if the simulation can identify the difference in the scrambling time as we vary the position of the V operator. Many protocols for computing OTOCs have been proposed [128, 157–161] and many authors have also suggested some modified quantities that also contain scrambling information [156, 159]. For example, to reduce the computational cost the magnitude-squared of OTOC ($|F|^2$, see Eq. (4.14) for definition of F) can be computed ignoring the phases [159]. In this paper, we have used the protocol proposed by Vermersch *et. al.* to compute both the OTOC and the modified OTOC [162]. The gate cost per circuit for computing the modified OTOC of zeroth order using this protocol is $\sim 2n(N-1)$, which is significantly lower than the gate-count needed in the straightforward evaluation presented by Fig. 4.18. Also the protocol we have chosen does not require any ancilla qubits unlike some other OTOC computation protocols.

Vermersch *et. al.* [163] discussed a 'global protocol' to compute the OTOC and a 'local protocol' for computing modified OTOCs. Both protocols require state preparation of random states created from random unitary operators. The idea is to sample enough random states to mimic a thermalized scenario for the computation of the OTOC. Mathematically, the global protocol relies upon the following equation

$$\begin{aligned} &\mathrm{Tr}\left[W(t)V^{\dagger}W(t)V\right] \\ &= \frac{1}{\mathcal{D}(\mathcal{D}+1)}\overline{\langle W(t)\rangle_{u,k_0}\langle V^{\dagger}W(t)V\rangle_{u,k_0}}, \end{aligned} \tag{4.17}$$

where, $\mathcal{D}$ is the dimension of the Hilbert space. On the right hand side, the overline denotes an ensemble average of measurements over a set $U = \{u_0, u_1, \cdots u_{N_U}\}$ of random unitary operators and k_0 is an abitrary initial state. Each unitary in the set U is a N-qubit unitary. Implementation of the global protocol requires creating a N-qubit random unitary operator that is applied to an input state of N qubits. Decomposition of an N-qubit unitary is costly in terms of the entangling gates. Moreover, for a specific precision, the local protocol needs a smaller number of measurements [128]. As a result, we have found it convenient to implement the local protocol in Fig. 4.19 which requires just N random unitaries per run. Depending on the number of initial states $|k_i\rangle = \{k_0, k_1, \cdots k_{2^n}\}$ being used, the modified OTOCs of different orders n can be computed. The larger the order n of the modified OTOC, the better it approximates the original OTOC while the specific n needed is model dependent. Indeed, there is evidence that the modified OTOCs contain the needed information on entanglement spreading [128].

For numerical justification of the Eq. (4.17) and for the connection of the different OTOC definitions, readers are advised to consult Appendix 4.7. Here, for completeness, we outline the steps to compute the modified OTOC of zeroth order:

- We prepare an arbitrary initial state $|k_0\rangle$ (position 1 in Fig 4.19a). The initial state

preparation step can be avoided if the all-zero state $|\mathbf{0}\rangle = |0000000\rangle$ is chosen as the starting quantum state. Then, a set of unitary gates $u^i = \{U_0^i, U_1^i, \cdots, U_N^i, \}$ are applied to each qubit, which results in a random state $|\psi_1\rangle = U_0^i \otimes U_1^i \otimes \cdots \otimes U_N^i |\mathbf{0}\rangle$ at position 2 in the Fig. 4.19a.

- Next the time evolution of the random state is computed using the Trotterized evolution operator $U(n) = \left[\exp\left(-i\hat{H}\delta t\right)\right]^n$. This yields $|\psi_2\rangle = U(n)|\psi_1\rangle$ at position 3 in the Fig. 4.19a.
- The necessary gates are then applied to compute the observable W in the computational basis. In our case, since $W = \sigma_i^z$, projective measurements of qubit i allows us to compute $\langle W(t)\rangle = p_0 - p_1$, where $p_{0(1)}$ is the probability of measuring the qubit in the zero (one) state. We use $N_{\text{shots}} = 200$ for computing the expectation value of the operator.
- In a similar fashion, if we include the V operator after creating the random state $|\psi_1\rangle$ (Fig. 4.19b), the previous two steps can be applied to compute $\langle V^\dagger W(t) V\rangle$.
- The process is repeated $N_R = 180$ times. Thus, measuring $\langle W\rangle$ (or $\langle VWV\rangle$) requires generating a total of $N_U = N_R \times N$ unitary matrices of size 2×2, with each unitary matrix drawn randomly from the Circular Unitary Ensemble (CUE) [164]. CUE(n) represents a uniform distribution over the unitary square matrices of dimension n – the Haar measure of the unitary group $U(n)$.
- Finally, an ensemble average of the quantity $\overline{\langle W(t)\rangle_{u,\mathbf{k}_0}\langle VW(t)V\rangle_{u,\mathbf{k}_0}}$ is computed which is a measure of the modified OTOC of the zeroth order.

With the proper normalization, the modified OTOC of the zeroth order $O_0(t)$, can be described by the following equation

$$O_0(t) = \frac{\overline{\langle W(t)\rangle_{u,\mathbf{k}_0}\langle VW(t)V\rangle_{u,\mathbf{k}_0}}}{\overline{\langle W(t)\rangle_{u,\mathbf{k}_0}\langle W(t)\rangle_{u,\mathbf{k}_0}}}. \tag{4.18}$$

Using the steps described above, operator expectation values $\langle W(t)\rangle$ and $\langle VW(t)V\rangle$ are

computed with the same set of unitaries. Fig. 4.20 shows measurements of these operators. Initially the operators are correlated (Fig. 4.20a) while over time due to operator spreading the operators become decorrelated (Fig. 4.20c) which signifies a loss of memory of the initial state. As the resources required for the computation of higher order OTOCs is large we have only computed the zeroth order OTOC in this study corresponding to the plot in Fig 4.21. $N_U = 180 \times N$ unitaries were used for this simulation and each measurement required $N_M = 200$ shots. These numbers were chosen carefully using a noise model simulation so as to minimize the overall cost for implementing the protocol with current quantum devices. From the figure, it is seen that mitigated results with the IBM Sherbrooke machine compare well with results from exact diagonalization. Dynamical decoupling (DD) was used to compensate coherent noise and M3 was used for the readout error mitigation. Our studies show that applying noise mitigation techniques is important in recovering scrambling information with current NISQ-era devices.

The dependence of the speed of information spread on the position of the V operator can be seen in Fig. 4.22 where it is compared with classical Python-Trotter simulations. The error bars in the simulation indicate the jackknife error due to the choice of different sets of random unitaries. For a fixed number of unitaries N_U, the error can be reduced at the expense of increased computational resources, that is, by increasing the number of shots N_{shots}. On the other hand, increasing the number of unitaries N_U also reduces the error, allowing us to better approximate the trace in Eq. (4.17) with the ensemble average on the right-hand side. Clearly, the measured values obtained with the IBM device without mitigation deviate from the ideal Python Trotter results, indicating the presence of different sources of noise in the device. The mitigated results agree rather well and can depict the difference in speed due to the varied distance $d = |j - i|$ of the W_i and V_j operators. It would be intriguing to see in the future whether we can use more computational resources to compute higher-order modified OTOCs.

Additionally, investigating the scrambling time and quantum Lyapunov exponents with

quantum computers could be an exciting avenue for the future research.

4.5 Conclusion

In this chapter, we have investigated the transverse quantum Ising model discretized on two dimensional anti-de Sitter space. In practice this is implemented by using site dependent couplings which mock up the metric factors corresponding to a one dimensional hyperbolic space. We computed the time evolution and OTOCs of the model using both tensor network methods and quantum simulations using both gate based quantum computers as well as simulation on analog quantum computers that use Rydberg arrays. We showed that the time evolution and OTOCs obtained from the quantum simulations agree well with the tensor network calculations.

The use of new publicly available universal quantum computers and new mitigation techniques allowed reliable time-evolution calculations with up to 13 qubits. In previous work on related real time evolution of systems of comparable difficulty [136, 138, 165, 166], reliable 4 qubit calculations were reported but extensions to 8 qubits were unsuccessful. Additionally, to the authors' best knowledge, this is the first time a protocol to compute OTOCs has been implemented for a seven qubit system using an IBM QPU, superseding a previous attempt with four qubits. From this perspective, the results presented here give a sense of the progress in quantum hardware and software in the last few years. Nevertheless, this remains a relatively small number of qubits and the boundary effects are significant. These boundary effects are of potential interest [167–169] and could be studied in more detail for their own sake.

We found that depending on the parameters of the model it's possible to have different profiles for the light cones that describe the propagation of information in the system. Perhaps most intriguingly we find a regime of the critical system where the direction of the light cones in global coordinates displays a logarithmic dependence on bulk distance. This

behavior implies that the scrambling time characterizing thermalization in this system depends only logarithmically on the number of degrees of freedom. Such a behavior is usually seen in models with long or even infinite range interactions while our model has only nearest neighbor interactions. We believe that this makes this model a very interesting candidate for future studies of scrambling in quantum spin models.

4.6 Appendix-Digital Quantum Simulation of the Magnetization

In this appendix, we present some observations of the simulation with digital quantum computing processors which would be useful for investigation of quantum field theories with quantum computers for interested readers.

4.6.1 Statistical error

In this subsection, we discuss statistical errors associated with different number of shots. Fig. 4.23 shows magnetization results obtained from the Guadalupe quantum computer with 200, 500 and 1000 shots. With our choice of the parameters, we find that the information about the magnetization is completely lost after ~ 7 Trotter steps for some of the cases. As a result, for the followup discussion, we considered data up-to the sixth trotter step. Varying the number of shots (N_{shots}) reduces the statistical error (ϵ_{stat}) and is roughly consistent with the relation $\epsilon_{\text{stat}} \propto 1/\sqrt{N_{\text{shots}}}$. Statistical errors were computed from data obtained from the six measurement sessions at different times. It's noteworthy that we do not see significant differences in the central value of the measurements. The central value stabilizes with the increase in the number of sessions. From our analysis, we find that the systematic error is much larger than the shot noise error. Hence, it is necessary to develop error-correction routines to recover correct results. With the NISQ-era devices, fault-tolerant computation is not feasible due to conflicting requirements of low fidelity of the qubits and the large qubit

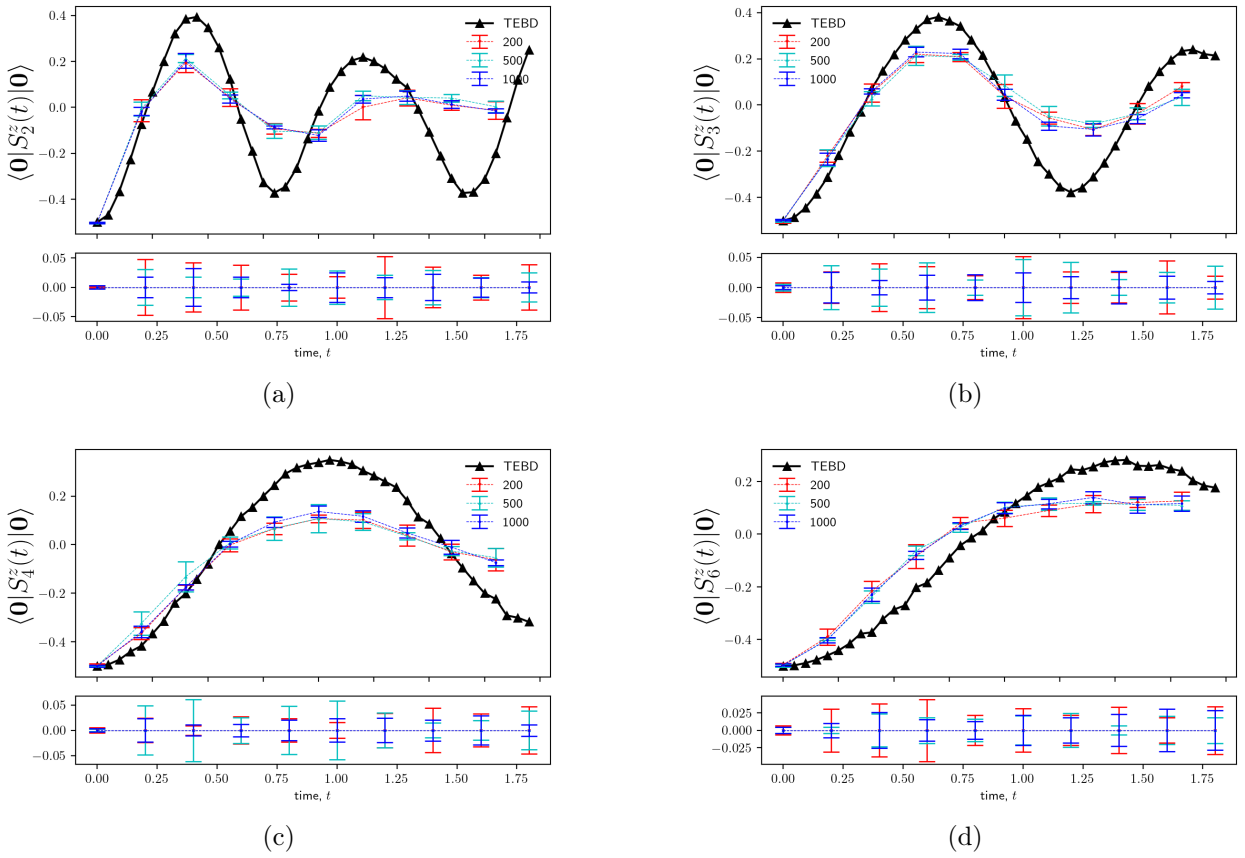

Figure 4.23: Shot noise analysis at Guadalupe machine is presented with local magnetization data. Shot noise associated for each trotter step is demonstrated in the bottom panel for the better visualization. The number in the labels denote the number of shots applied for measurements. Gap between the corresponding classical TEBD simulation results and QPU results indicate the presence of other coherent and incoherent sources of noise. Parameters: $J = 2.0$, $h = 1.05$, $l_{\max} = 3.0$.

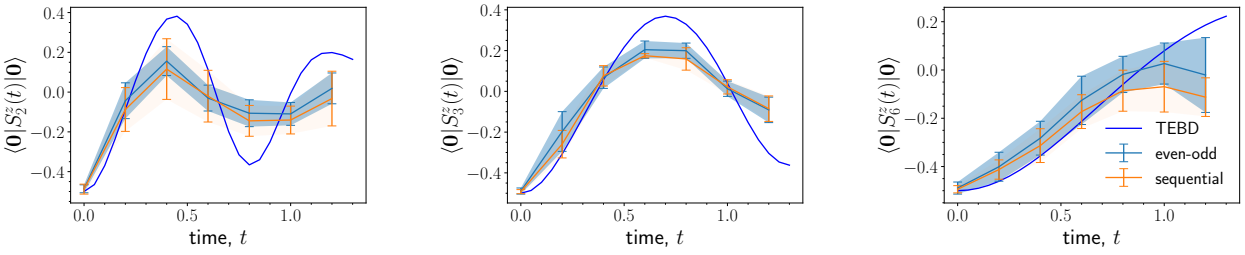

Figure 4.24: Comparison of Trotter evolution of magnetization results with different operator ordering. Parameters: $J = 2.0$, $h = 1.05$, $l_{\max} = 3.0$.

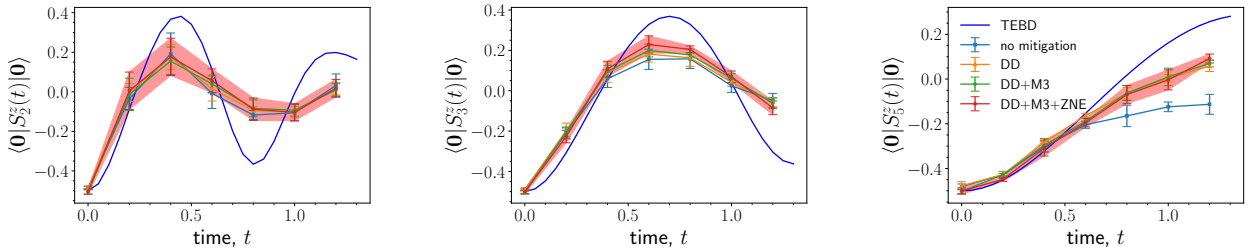

(a) (b) (c)

Figure 4.25: Comparison of magnetization results with different mitigation techniques and their combinations. Parameters: $J = 2.0$, $h = 1.05$, $l_{\max} = 3.0$.

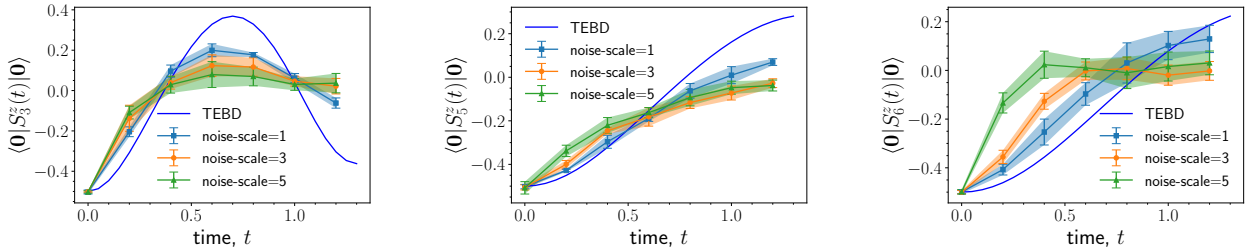

(a) (b) (c)

Figure 4.26: Comparison of Trotter evolution of magnetization results in different noise scaled circuits. Noise scale=n indicates n-fold noise compared to the original circuit for the Trotter evolution of the local magnetization. Parameters: $J = 2.0$, $h = 1.05$, $l_{\max} = 3.0$.

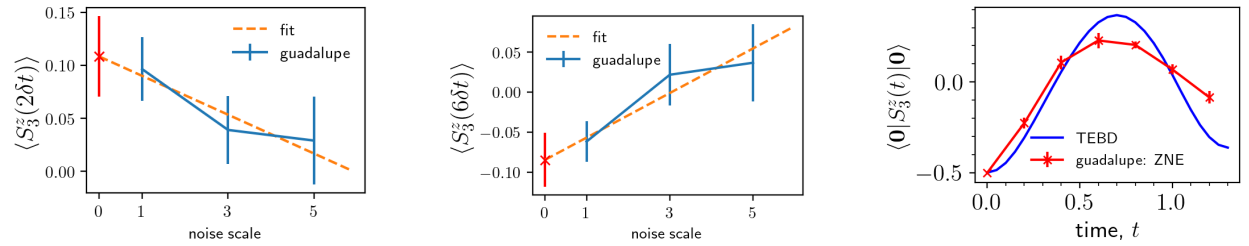

(a) (b) (c)

Figure 4.27: (a-b) Example of the extraction of the zero noise extrapolated data (red cross) at the second and the sixth trotter step, obtained from the measurements of the noise-scaled-circuits at guadalupe machine. (c) Extrapolated values are obtained for all trotter steps to plot ZNE data of the local magnetization. Parameters: $J = 2.0$, $h = 1.05$, $l_{\max} = 3.0$, $\delta t = 0.2$.

overhead for error-correction protocols. However, different error mitigation techniques can be applied to scale up the number of qubits for simulation in the current NISQ-devices. In the following section, we discuss the application of the different error mitigation techniques

to improve results obtained from the quantum processing units.

4.6.2 Operator ordering

Fig. 4.24 demonstrates how the local magnetization of $N = 13$ qubit lattice chain obtained from the Guadalupe QPU compares with different operator-ordering. To address the question of the operator-ordering we exclude mitigation techniques and circuit optimization techniques. Each data point was obtained from the average of six experiments each with 200 shots. Here, the label 'sequential' implies that the continuum evolution operator is approximated as

$$U_{\text{seq}} = \prod_{l} h^{l}_{\text{int}} \prod_{k} h^{k}_{x}, \tag{4.19}$$

whereas, the following ordering of operator denotes 'odd-even' ordering of operators

$$U_{\text{odd}-\text{even}} = \prod_{l,\,\text{even}} h^{l}_{\text{int}} \prod_{l,\,\text{odd}} h^{l}_{\text{int}} \prod_{k} h^{k}_{x}. \tag{4.20}$$

Local operators are defined as $h^{k}_{x} = \exp\big(-i\frac{h}{2}\eta_k\sigma^{x}_{k}\big)$ and $h^{l}_{\text{int}} = \exp\Big(i\frac{J}{4}\frac{(\eta_l+\eta_{l+1})}{2}\sigma^{z}_{l}\sigma^{z}_{l+1}\Big)$.

We did not find a particular choice of the operator ordering to be an important factor in the noisy Guadalupe device. Indeed, it is likely that the systematic errors will much larger than the differences in measurements associated with different choices of operator ordering in the current NISQ devices.

4.6.3 Error mitigation

In this subsection, we discuss the importance of different error mitigation techniques in the context of computations of the real time evolution of the magnetization of our model. We first analyze results obtained with dynamical decoupling (DD), then with a combination of dynamical decoupling and M3 (DD+M3) mitigation techniques, and finally with a combination of dynamical decoupling, M3 and Zero Noise Extrapolation (DD+M3+ZNE) techniques.

Further observation on the combined cases of error mitigation revealed that for some cases like $\langle S_3^z(t)\rangle$ in Fig 4.25a, local magnetization data did not improve the results much. In contrast, for some cases like Fig 4.25b, the results were significantly improved and for the rest (Fig 4.25c), it is found that the results were improved only for large trotter steps.

On top of the dynamical decoupling and readout error correction technique, we applied Zero Noise Extrapolation (ZNE) to mitigate incoherent noise. The first step in the process is to scale up the noise systematically by generating unitary gate-folding or pulse-stretching [‡]. We used unitary folding by mapping a two-qubit operator $U \rightarrow UU^{\dagger}U$. For pair of CX gates that are added one increases the noise-level by a factor of three. The second step is to perform measurements in the folded circuits and finally use these measurements with different noise levels to extrapolate a zero noise limit of the observables. Fig. 4.26 clearly demonstrates that increasing the noise by adding more unitaries causes the experimental values to deviate further away from the classically computed results with TEBD. The noise scaled values that are obtained for local magnetization $\langle S_i^z\rangle$ at a time t_0 are then used to extrapolate zero-noise value by linear extrapolations (Fig 4.27a,4.27b). Extrapolated values obtained at different trotter step are then combined to produce the time dependent magnetization curve Fig 4.27c.

4.7 Appendix-Digital Quantum Simulation: OTOC

In this section of the appendix, we will discuss some of the details of the OTOC computation with quantum simulators and quantum processing units.

Just like the magnetization, we need to pick a suitable Trotter step to observe physics with current NISQ era machines. Fig 4.28 demonstrates that $\delta t = 0.5$ is a suitable choice. As the OTOC drops from one to zero in four Trotter steps, the entangling gate-cost for the measurements of $\langle W\rangle$ and $\langle VWV\rangle$ (see Fig 4.19 in the main text) is manageable with

[‡]Pulse stretching needs pulse level access to device where the amount of noise introduced is controlled by the duration of the pulse applied to implement different gates.

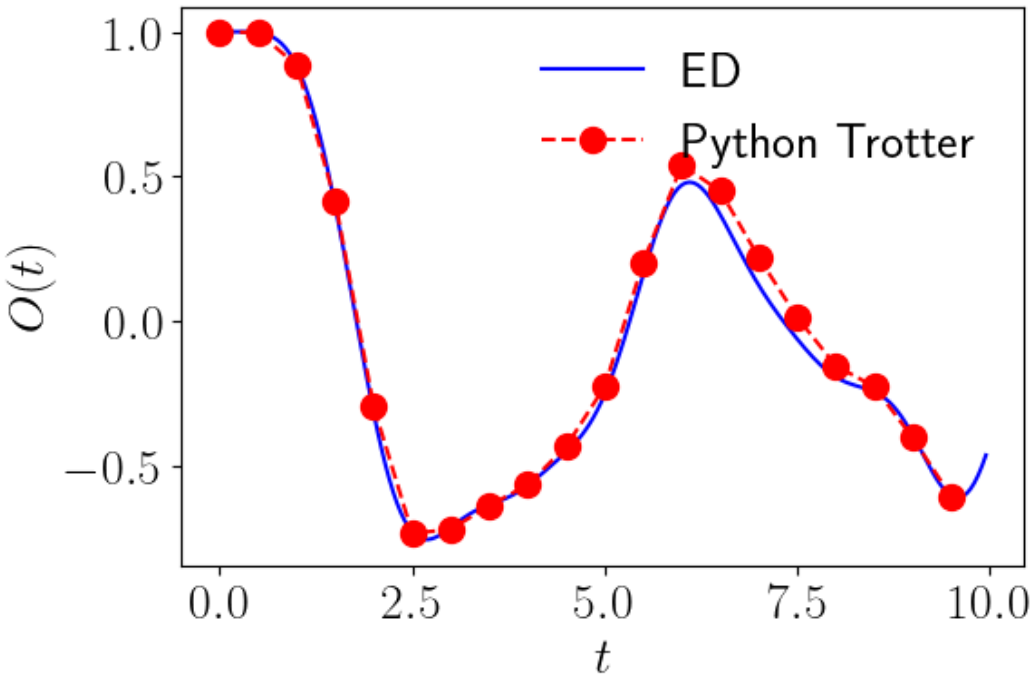

Figure 4.28: Choice of the Trotter step $\delta t \sim 0.5$ seems a good choice for the OTOC computation with our choice of parameters

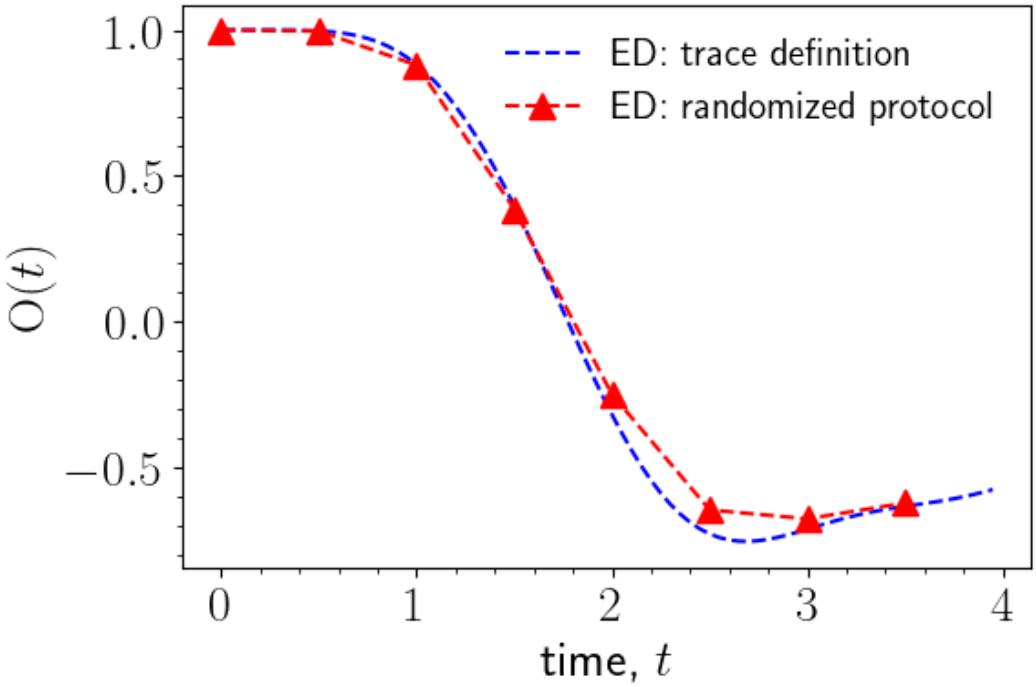

Figure 4.29: OTOC computed with the protocol with global unitaries match with traced data of products of operators.

current NISQ devices and a comparison of the Trotterized version (without shot noise) of the results and the exact-diagonalized results reveal that the Trotter error associated with the trotter step is not large enough to obscure the physics we are interested in (Fig 4.28).

We conclude this section of the appendix by justifying Eq. (4.17) numerically. In Fig 4.29, we compared the OTOC computed from the trace definition with the results obtained from the global protocol developed by Vermersch *et. al.* [128] with numerics . For a mathematical proof of the identity, please see the appendix in [170]. Higher order modified OTOCs computed from the local protocol yields the same result as that of global protocol [163].

4.8 Appendix-Examples of different propagation patterns of OTOCs

As shown in the cartoon phase diagram for the OTOCs in Fig. 4.15 there are many distinct characteristics for the propagation of the OTOCs. Here we give more examples for these different behaviours starting from the power law spreading.

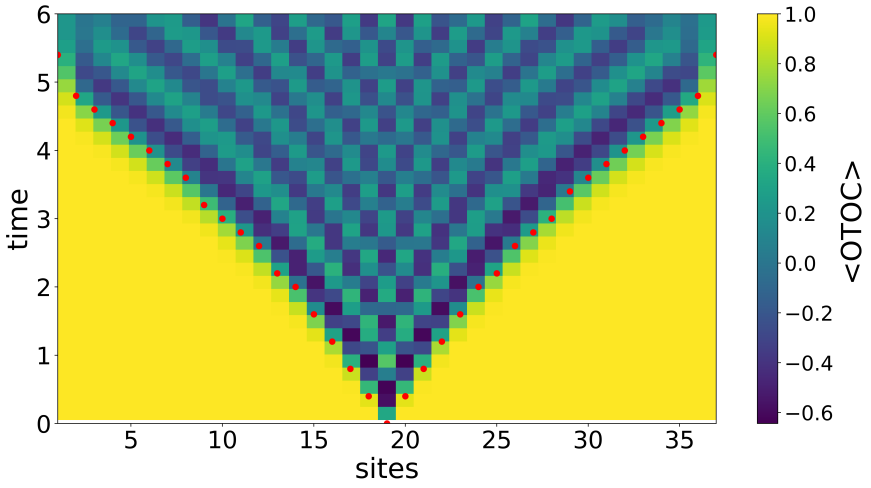

Figure 4.30: ZZ OTOC for $J = 6, h = 3.05, m = 0.25, l = 2.0$

And finally we also give an example for the confined behaviour of the OTOC propagation.

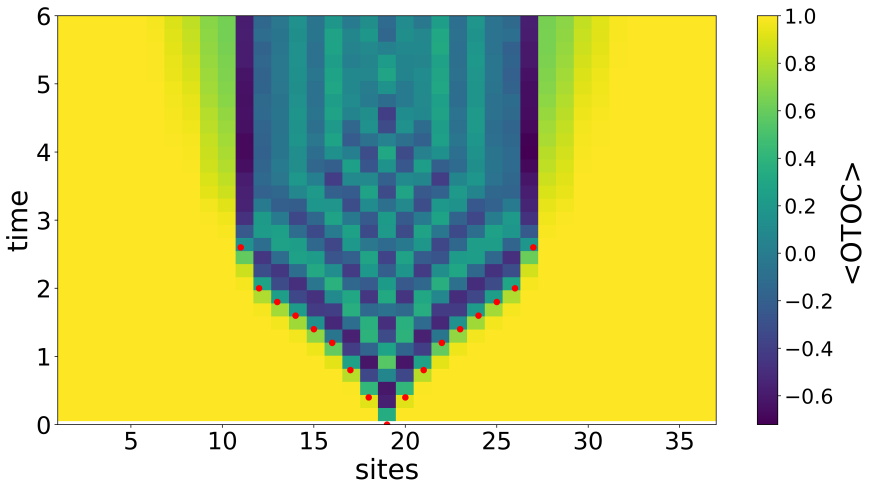

Figure 4.31: ZZ OTOC for $J = 6, h = 3.05, m = 0.25, l = 5.0$

Chapter 5

Conclusions

In this thesis, our main goal was to investigate holography and the AdS/CFT correspondence using both classical and quantum computational methods. For our classical computational studies, we have developed lattice simulations for the $\mathcal{N} = 4$ SYM model with a new term in the action that suppressed the well-known problems of the original action. This new action allowed us to simulate this model up to very strongly coupled regimes of the model where holographic predictions can be tested. We showed that the lattice model exists in a single phase with unbroken supersymmetry even at very strong coupling by calculating the Polayakov lines and Ward Identities. We also demonstrated that our lattice model is free of sign problems which can have catastrophic effects on Monte Carlo simulations.

To connect with holographic physics, we calculated the supersymmetric Wilson Loops for a $SU(2)$ and $SU(3)$ $\mathcal{N} = 4$ SYM model and showed that they exhibit the expected $\sqrt{\lambda}$ dependence from holography. We then calculated the correlators of smeared Polyakov lines to calculate the non Abelian potential for this model using $SU(3)$ $\mathcal{N} = 4$ SYM model. These correlators exhibited the expected $1/R$ dependence and the results of the fits for the $1/R$ dependence of these correlators also showed the expected $\sqrt{\lambda}$ dependence. These results constitute a very nontrivial check of the AdS/CFT correspondence using lattice simulations and open up the way to study $\mathcal{N} = 4$ SYM models wide array of non-perturbative features

such as anomalous dimension, corrections of stringy corrections to holography, and S-duality further in future studies.

In the final chapter of this thesis, we developed tensor network and quantum simulations for a transverse Ising Model that lives in AdS_2 space. We investigated this Ising model's ground state properties using DMRG and located the phase transition point. We also developed quantum simulations for this model for both universal and analog quantum computers. We ran our quantum circuit for the time evolution of this model on IBMQ-Guadalupe using 13 qubits (the longest chain that can be done with this architecture) and showed that after some error-mitigation they show excellent agreement with the expected results. This shows us that this model is suitable to simulate on current NISQ hardware. For the analog side of the quantum simulations, we developed a Rydberg construction for this model by carefully engineering the right interactions between Rydberg atoms and we tested our construction using a Rydberg simulator. We couldn't do actual Rydberg simulations of this model on quantum hardware due to current Rydberg computers not having access to the site dependent detuning factors. However, our the simulator results showed the expected behavior for the time evolution of the magnetization showing us that it's possible to use Rydberg arrays for quantum simulating this model in the future.

In the latter part of the Chapter. 4 we calculated OTOCs for this model using classical and quantum simulation techniques. These correlators are used to measure information propagation and scrambling in quantum systems. When we calculated OTOCs we saw a very interesting propagation pattern that changed with respect to the background curvature and the strength of nearest neighbor coupling. This dependence can be classified into 4 distinct regions where we have linear, power law, logarithmic, or confining propagation patterns depending on these two parameters. The most interesting region for this propagation is the logarithmic regime where models that exhibit such behavior are classified as fast scramblers. Previously, all models that were classified as fast scramblers were either all-to-all models like the SYK model or they have infinite or very long-range interactions. Our model with

only site-dependent couplings and a nearest-neighbor interaction managed to capture this interesting behavior which makes it a very interesting test bed to study scrambling and information propagation in quantum systems due to its natural implementation on quantum computers. We also implemented a randomized measurement algorithm to measure OTOCs on quantum computers that was developed by Vermersch et al. [163]. We implemented their algorithm on the IBMQ Sherbrooke and obtained excellent agreement for the OTOC operator compared to their classial counterparts using 7-qubits. An interesting of this $1+1d$ Ising model would be to consider the $2+1$ dimension and study the scrambling behavior and boundary boundary correlators again using tensor network and quantum computing methods.

Bibliography

[1] V. E. Hubeny, Class. Quantum Grav. **32**, 124010 (2015), ISSN 0264-9381, 1361-6382, arXiv:1501.00007 [gr-qc, physics:hep-th], URL `http://arxiv.org/abs/1501.00007`.

[2] A. Zaffaroni, Class. Quant. Grav. **17**, 3571 (2000).

[3] G. T. Horowitz and J. Polchinski, Approaches to quantum gravity pp. 169–186 (2009).

[4] J. B. Kogut, Rev. Mod. Phys. **51**, 659 (1979), URL `https://link.aps.org/doi/10.1103/RevModPhys.51.659`.

[5] M. Creutz, *Quarks, Gluons and Lattices* (Oxford University Press, 1983), ISBN 978-1-00-929039-5, 978-1-00-929038-8, 978-1-00-929037-1, 978-0-521-31535-7.

[6] K. G. Wilson, Phys. Rev. D **10**, 2445 (1974), URL `https://link.aps.org/doi/10.1103/PhysRevD.10.2445`.

[7] Z. Davoudi et al., in *Snowmass 2021* (2022), `2209.10758`.

[8] A. S. Kronfeld et al. (USQCD) (2022), `2207.07641`.

[9] P. Dondi and H. Nicolai, Il Nuovo Cimento A (1965-1970) **41**, 1 (1977).

[10] M. Kato, M. Sakamoto, and H. So, Journal of High Energy Physics **2008**, 057 (2008).

[11] A. D'Adda, N. Kawamoto, and J. Saito, Journal of High Energy Physics **2017**, 1 (2017).

[12] S. Catterall, D. B. Kaplan, and M. Unsal, Phys. Rept. **484**, 71 (2009), 0903.4881.

[13] S. Catterall, J. Giedt, and G. C. Toga, JHEP **12**, 140 (2020), 2009.07334.

[14] S. Catterall, J. Giedt, and G. C. Toga, JHEP **08**, 084 (2023), 2303.16025.

[15] C. W. Bauer et al., PRX Quantum **4**, 027001 (2023), 2204.03381.

[16] Y. Meurice, R. Sakai, and J. Unmuth-Yockey, Rev. Mod. Phys. **94**, 025005 (2022), 2010.06539.

[17] M. C. Bañuls, Ann. Rev. Condensed Matter Phys. **14**, 173 (2023), 2205.10345.

[18] M. C. Bañuls et al., Eur. Phys. J. D **74**, 165 (2020), 1911.00003.

[19] M. C. Banuls, K. Cichy, Y.-J. Kao, C. J. D. Lin, Y.-P. Lin, and D. T. L. Tan, PoS **LATTICE2018**, 229 (2018), 1810.12038.

[20] Y. Meurice, J. C. Osborn, R. Sakai, J. Unmuth-Yockey, S. Catterall, and R. D. Somma, arXiv preprint arXiv:2203.04902 (2022).

[21] J. Maldacena, International journal of theoretical physics **38**, 1113 (1999).

[22] G. T. Horowitz and A. Strominger, Nuclear Physics B **360**, 197 (1991).

[23] S. Weinberg and E. Witten, Physics Letters B **96**, 59 (1980).

[24] E. Witten, arXiv preprint hep-th/9802150 (1998).

[25] L. Susskind and E. Witten, arXiv preprint hep-th/9805114 (1998).

[26] E. D'HOKER and D. Z. Freedman, in *Strings, Branes and Extra Dimensions: TASI 2001* (World Scientific, 2004), pp. 3–159.

[27] P. Banerjee, *St4 lectures on assorted topics in ads3/cft2, lecture notes from* (2018).

[28] J. Kaplan, *Lectures on ads/cft from the bottom up* (2016).

[29] E. Witten, Communications in Mathematical Physics **118**, 411 (1988).

[30] N. Marcus, Nuclear Physics B **452**, 331 (1995).

[31] P. Becher and H. Joos, Zeitschrift für Physik C Particles and Fields **15**, 343 (1982).

[32] M. Asaduzzaman, S. Catterall, Y. Meurice, R. Sakai, and G. C. Toga (2023), 2312.16167.

[33] M. Asaduzzaman, S. Catterall, Y. Meurice, R. Sakai, and G. C. Toga, JHEP **01**, 024 (2023), 2210.03834.

[34] N. Butt, S. Catterall, and G. C. Toga, Symmetry **13**, 2276 (2021), 2111.01001.

[35] N. Butt, S. Catterall, A. Pradhan, and G. C. Toga, Phys. Rev. D **104**, 094504 (2021), 2101.01026.

[36] S. Catterall and A. Pradhan, Phys. Rev. D **106**, 014509 (2022), 2201.00750.

[37] N. Marcus, Nucl. Phys. **B452**, 331 (1995), hep-th/9506002.

[38] A. Kapustin and E. Witten, Commun. Num. Theor. Phys. **1**, 1 (2007), hep-th/0604151.

[39] S. Catterall, J. Giedt, and A. Joseph, JHEP **1310**, 166 (2013), 1306.3891.

[40] M. A. Nielsen and I. L. Chuang, *Quantum computation and quantum information*, vol. 2 (Cambridge university press Cambridge, 2001).

[41] D. Gottesman, arXiv preprint quant-ph/9807006 (1998).

[42] H. F. Trotter, Proceedings of the American Mathematical Society **10**, 545 (1959).

[43] M. Suzuki, Physics Letters A **180**, 232 (1993).

[44] U. Schollwöck, Reviews of modern physics **77**, 259 (2005).

[45] F. Verstraete, T. Nishino, U. Schollwöck, M. C. Bañuls, G. K. Chan, and M. E. Stoudenmire, Nature Reviews Physics **5**, 273 (2023).

[46] S. R. White, Physical review letters **69**, 2863 (1992).

[47] S. Paeckel, T. Köhler, A. Swoboda, S. R. Manmana, U. Schollwöck, and C. Hubig, Annals of Physics **411**, 167998 (2019).

[48] D. Bauernfeind and M. Aichhorn, SciPost Physics **8**, 024 (2020).

[49] R. Orus and G. Vidal, Physical Review B **78**, 155117 (2008).

[50] S. Catterall, E. Dzienkowski, J. Giedt, A. Joseph, and R. Wells, JHEP **1104**, 074 (2011), 1102.1725.

[51] S. Catterall, P. H. Damgaard, T. Degrand, R. Galvez, and D. Mehta, JHEP **1211**, 072 (2012), 1209.5285.

[52] S. Catterall, D. Schaich, P. H. Damgaard, T. DeGrand, and J. Giedt, Phys. Rev. D **90**, 065013 (2014), 1405.0644.

[53] D. Schaich, PoS **LATTICE2018**, 005 (2019), 1810.09282.

[54] K. N. Anagnostopoulos, M. Hanada, J. Nishimura, and S. Takeuchi, Phys. Rev. Lett. **100**, 021601 (2008), 0707.4454.

[55] M. Hanada, A. Miwa, J. Nishimura, and S. Takeuchi, Phys. Rev. Lett. **102**, 181602 (2009), 0811.2081.

[56] S. Catterall and T. Wiseman, Phys. Rev. D **78**, 041502 (2008), 0803.4273.

[57] S. Catterall and T. Wiseman, JHEP **04**, 077 (2010), 0909.4947.

[58] S. Catterall, A. Joseph, and T. Wiseman, JHEP **12**, 022 (2010), 1008.4964.

[59] M. Hanada, Y. Hyakutake, G. Ishiki, and J. Nishimura, Phys. Rev. D **94**, 086010 (2016), 1603.00538.

[60] E. Berkowitz, E. Rinaldi, M. Hanada, G. Ishiki, S. Shimasaki, and P. Vranas, Phys. Rev. D **94**, 094501 (2016), 1606.04951.

[61] S. Catterall, R. G. Jha, D. Schaich, and T. Wiseman, Phys. Rev. D **97**, 086020 (2018), 1709.07025.

[62] E. Rinaldi, E. Berkowitz, M. Hanada, J. Maltz, and P. Vranas, JHEP **02**, 042 (2018), 1709.01932.

[63] S. Catterall, J. Giedt, D. Schaich, P. H. Damgaard, and T. DeGrand, PoS **LATTICE2014**, 267 (2014), 1411.0166.

[64] S. Catterall and D. Schaich, JHEP **07**, 057 (2015), 1505.03135.

[65] W. Krauth, H. Nicolai, and M. Staudacher, Phys. Lett. B **431**, 31 (1998), hep-th/9803117.

[66] T. Eguchi and H. Kawai, Phys.Rev.Lett. **48**, 1063 (1982).

[67] J. Erickson, G. Semenoff, and K. Zarembo, Nucl. Phys. B **582**, 155 (2000), hep-th/0003055.

[68] N. Drukker and D. J. Gross, J. Math. Phys. **42**, 2896 (2001), hep-th/0010274.

[69] J. M. Maldacena, Phys. Rev. Lett. **80**, 4859 (1998), hep-th/9803002.

[70] S. Catterall, JHEP **0801**, 048 (2008), 0712.2532.

[71] A. G. Cohen, D. B. Kaplan, E. Katz, and M. Unsal, JHEP **08**, 024 (2003), hep-lat/0302017.

[72] A. G. Cohen, D. B. Kaplan, E. Katz, and M. Unsal, JHEP **12**, 031 (2003), hep-lat/0307012.

[73] D. B. Kaplan and M. Unsal, JHEP **09**, 042 (2005), hep-lat/0503039.

[74] S. Catterall, J. Giedt, R. G. Jha, D. Schaich, and T. Wiseman, Phys. Rev. D **102**, 106009 (2020), 2010.00026.

[75] M. A. Clark, PoS **LAT2006**, 004 (2006), hep-lat/0610048.

[76] M. Albanese, F. Costantini, G. Fiorentini, F. Flore, M. Lombardo, R. Tripiccione, P. Bacilieri, L. Fonti, P. Giacomelli, E. Remiddi, et al., Physics Letters B **192**, 163 (1987).

[77] S.-x. Chu, D. Hou, and H.-c. Ren, JHEP **08**, 004 (2009), 0905.1874.

[78] N. Beisert et al., Lett. Math. Phys. **99**, 3 (2012), 1012.3982.

[79] V. E. Hubeny, Class. Quant. Grav. **32**, 124010 (2015), 1501.00007.

[80] M. Asaduzzaman, S. Catterall, J. Hubisz, R. Nelson, and J. Unmuth-Yockey, Phys. Rev. D **102**, 034511 (2020), 2005.12726.

[81] R. C. Brower, C. V. Cogburn, A. L. Fitzpatrick, D. Howarth, and C.-I. Tan, Phys. Rev. D **103**, 094507 (2021), 1912.07606.

[82] M. Asaduzzaman, S. Catterall, J. Hubisz, R. Nelson, and J. Unmuth-Yockey, Phys. Rev. D **106**, 054506 (2022), 2112.00184.

[83] R. C. Brower, C. V. Cogburn, and E. Owen, Phys. Rev. D **105**, 114503 (2022), 2202.03464.

[84] B. Swingle, Physical Review D **86**, 065007 (2012).

[85] B. Swingle, arXiv preprint arXiv:1209.3304 (2012).

[86] M. Steinberg and J. Prior, Scientific Reports **12**, 532 (2022).

[87] A. Jahn, Z. Zimborás, and J. Eisert, Quantum **6**, 643 (2022).

[88] P. Basteiro, F. Dusel, J. Erdmenger, D. Herdt, H. Hinrichsen, R. Meyer, and M. Schrauth, Physical Review Letters **130**, 091604 (2023).

[89] M. Rigol, V. Dunjko, and M. Olshanii, Nature **452**, 854 (2008), URL https://doi.org/10.1038%2Fnature06838.

[90] M. Srednicki, Phys. Rev. E **50**, 888 (1994), URL https://link.aps.org/doi/10.1103/PhysRevE.50.888.

[91] A. M. Kaufman, M. E. Tai, A. Lukin, M. Rispoli, R. Schittko, P. M. Preiss, and M. Greiner, Science **353**, 794 (2016), URL https://doi.org/10.1126%2Fscience.aaf6725.

[92] J. D. Bekenstein, Phys. Rev. D **7**, 2333 (1973).

[93] J. D. Bekenstein, Contemp. Phys. **45**, 31 (2003), quant-ph/0311049.

[94] J. Eisert, M. Cramer, and M. B. Plenio, Rev. Mod. Phys. **82**, 277 (2010), 0808.3773.

[95] O. Aharony, S. S. Gubser, J. M. Maldacena, H. Ooguri, and Y. Oz, Phys. Rept. **323**, 183 (2000), hep-th/9905111.

[96] S. Xu and B. Swingle, Nature Physics **16**, 199 (2020), ISSN 1745-2473, 1745-2481, URL http://www.nature.com/articles/s41567-019-0712-4.

[97] Y. Kusuki and M. Miyaji, Journal of High Energy Physics **2019**, 63 (2019), ISSN 1029-8479, URL https://link.springer.com/10.1007/JHEP08(2019)063.

[98] D. Yuan, S.-Y. Zhang, Y. Wang, L.-M. Duan, and D.-L. Deng, Physical Review Research **4**, 023095 (2022), ISSN 2643-1564, URL https://link.aps.org/doi/10.1103/PhysRevResearch.4.023095.

[99] A. Bhattacharyya, L. K. Joshi, and B. Sundar, The European Physical Journal C **82**, 458 (2022), ISSN 1434-6052, arXiv:2111.11945 [hep-th, physics:quant-ph], URL http://arxiv.org/abs/2111.11945.

[100] S. Xu and B. Swingle, *Scrambling Dynamics and Out-of-Time Ordered Correlators in Quantum Many-Body Systems: a Tutorial* (2022), arXiv:2202.07060 [cond-mat, physics:hep-th, physics:quant-ph], URL http://arxiv.org/abs/2202.07060.

[101] N. Tsuji, T. Shitara, and M. Ueda, Phys. Rev. E **98**, 012216 (2018), 1706.09160.

[102] G. Bentsen, Y. Gu, and A. Lucas, Proc. Nat. Acad. Sci. **116**, 6689 (2019), 1805.08215.

[103] M. Campisi and J. Goold, Phys. Rev. E **95**, 062127 (2017), 1609.05848.

[104] S. Pappalardi, A. Russomanno, B. Žunkovič, F. Iemini, A. Silva, and R. Fazio, Phys. Rev. B **98**, 134303 (2018), URL https://link.aps.org/doi/10.1103/PhysRevB.98.134303.

[105] A. Bohrdt, C. B. Mendl, M. Endres, and M. Knap, New J. Phys. **19**, 063001 (2017), 1612.02434.

[106] A. Smith, J. Knolle, R. Moessner, and D. L. Kovrizhin, Physical Review Letters **123**, 086602 (2019).

[107] E. H. Lieb and D. W. Robinson, *The finite group velocity of quantum spin systems* (Springer, 2004).

[108] S. H. Shenker and D. Stanford, JHEP **03**, 067 (2014), 1306.0622.

[109] S. H. Shenker and D. Stanford, JHEP **05**, 132 (2015), 1412.6087.

[110] J. Maldacena, S. H. Shenker, and D. Stanford, JHEP **08**, 106 (2016), 1503.01409.

[111] I. L. Aleiner, L. Faoro, and L. B. Ioffe, Annals Phys. **375**, 378 (2016), 1609.01251.

[112] Y. Sekino and L. Susskind, Journal of High Energy Physics **2008**, 065 (2008), ISSN 1029-8479, arXiv:0808.2096 [hep-th, physics:quant-ph], URL http://arxiv.org/abs/0808.2096.

[113] N. Lashkari, D. Stanford, M. Hastings, T. Osborne, and P. Hayden, Journal of High Energy Physics **2013**, 22 (2013), ISSN 1029-8479, arXiv:1111.6580 [hep-th, physics:quant-ph], URL http://arxiv.org/abs/1111.6580.

[114] S. Sachdev and J. Ye, Physical review letters **70**, 3339 (1993).

[115] *Alexei Kitaev, Caltech & KITP, A simple model of quantum holography (part 1)*, URL https://online.kitp.ucsb.edu/online/entangled15/kitaev/.

[116] *Alexei Kitaev, Caltech, A simple model of quantum holography (part 2)*, URL https://online.kitp.ucsb.edu/online/entangled15/kitaev2/.

[117] J. Maldacena and D. Stanford, Phys. Rev. D **94**, 106002 (2016), URL https://link.aps.org/doi/10.1103/PhysRevD.94.106002.

[118] J. Polchinski and V. Rosenhaus, JHEP **04**, 001 (2016), 1601.06768.

[119] S. R. White and A. E. Feiguin, Physical review letters **93**, 076401 (2004).

[120] S. R. White, Phys. Rev. B **48**, 10345 (1993), URL https://link.aps.org/doi/10.1103/PhysRevB.48.10345.

[121] U. Schollwöck, Rev. Mod. Phys. **77**, 259 (2005), URL https://link.aps.org/doi/10.1103/RevModPhys.77.259.

[122] G. Vidal, Phys. Rev. Lett. **91**, 147902 (2003), URL https://link.aps.org/doi/10.1103/PhysRevLett.91.147902.

[123] F. Verstraete, J. J. Garcia-Ripoll, and J. I. Cirac, Physical review letters **93**, 207204 (2004).

[124] G. Vidal, Phys. Rev. Lett. **93**, 040502 (2004), URL https://link.aps.org/doi/10.1103/PhysRevLett.93.040502.

[125] M. Fishman, S. R. White, and E. M. Stoudenmire (2020), 2007.14822.

[126] Y. Huang, Y.-L. Zhang, and X. Chen, Annalen Phys. **529**, 1600318 (2017), 1608.01091.

[127] X. Chen, T. Zhou, D. A. Huse, and E. Fradkin, Annalen Phys. **529**, 1600332 (2017), 1610.00220.

[128] B. Vermersch, A. Elben, L. M. Sieberer, N. Y. Yao, and P. Zoller, Physical Review X **9**, 021061 (2019), ISSN 2160-3308, arXiv:1807.09087 [cond-mat, physics:hep-th, physics:physics, physics:quant-ph], URL http://arxiv.org/abs/1807.09087.

[129] M. Asaduzzaman, S. Catterall, J. Hubisz, R. Nelson, and J. Unmuth-Yockey, Physical Review D **106**, 054506 (2022).

[130] R. C. Brower, C. V. Cogburn, A. L. Fitzpatrick, D. Howarth, and C.-I. Tan, Physical Review D **103**, 094507 (2021).

[131] H. Ueda, H. Nakano, K. Kusakabe, and T. Nishino, Journal of the Physical Society of Japan **80**, 094001 (2011), ISSN 0031-9015, 1347-4073, arXiv:1102.0845 [cond-mat], URL http://arxiv.org/abs/1102.0845.

[132] H. Ueda, A. Gendiar, V. Zauner, T. Iharagi, and T. Nishino, *Transverse Field Ising Model Under Hyperbolic Deformation* (2010), arXiv:1008.3458 [cond-mat, physics:quant-ph], URL http://arxiv.org/abs/1008.3458.

[133] H. Ueda, H. Nakano, K. Kusakabe, and T. Nishino, Progress of Theoretical Physics **124**, 389 (2010), ISSN 0033-068X, 1347-4081, arXiv:1006.2652 [cond-mat, physics:quant-ph], URL http://arxiv.org/abs/1006.2652.

[134] M. Suzuki, Communications in Mathematical Physics **51**, 183 (1976).

[135] G. Vidal, Physical review letters **91**, 147902 (2003).

[136] E. Gustafson, P. Dreher, Z. Hang, and Y. Meurice, Quantum Science and Technology **6**, 045020 (2021).

[137] Y. Meurice, *Quantum Field Theory* (IOP Publishing, 2021).

[138] M. Asaduzzaman, G. C. Toga, S. Catterall, Y. Meurice, and R. Sakai, Physical Review D **106**, 114515 (2022).

[139] L. Viola and S. Lloyd, Physical Review A **58**, 2733 (1998).

[140] C. Charles, E. J. Gustafson, E. Hardt, F. Herren, N. Hogan, H. Lamm, S. Starecheski, R. S. Van de Water, and M. L. Wagman, arXiv preprint arXiv:2305.02361 (2023).

[141] P. D. Nation, H. Kang, N. Sundaresan, and J. M. Gambetta, PRX Quantum **2**, 040326 (2021).

[142] K. Temme, S. Bravyi, and J. M. Gambetta, Physical review letters **119**, 180509 (2017).

[143] Y. Li and S. C. Benjamin, Phys. Rev. X **7**, 021050 (2017), URL `https://link.aps.org/doi/10.1103/PhysRevX.7.021050`.

[144] I. Cong, H. Levine, A. Keesling, D. Bluvstein, S.-T. Wang, and M. D. Lukin, Phys. Rev. X **12**, 021049 (2022), `2105.13501`.

[145] S. Ebadi et al., Nature **595**, 227 (2021), `2012.12281`.

[146] A. Keesling et al., Nature **568**, 207 (2019), `1809.05540`.

[147] *Bloqade.jl: Package for the quantum computation and quantum simulation based on the neutral-atom architecture.* (2023), URL `https://github.com/QuEraComputing/Bloqade.jl`.

[148] B. Swingle, Nature Phys. **14**, 988 (2018).

[149] C.-J. Lin and O. I. Motrunich, Phys. Rev. B **97**, 144304 (2018), URL https://link.aps.org/doi/10.1103/PhysRevB.97.144304.

[150] I. García-Mata, R. A. Jalabert, and D. A. Wisniacki, Scholarpedia **18**, 55237 (2023), 2209.07965.

[151] A. Schuckert and M. Knap, SciPost Phys. **7**, 022 (2019), URL https://scipost.org/10.21468/SciPostPhys.7.2.022.

[152] A. Goussev, R. A. Jalabert, H. M. Pastawski, and D. Wisniacki, arXiv preprint arXiv:1206.6348 (2012).

[153] L. K. Joshi, A. Elben, A. Vikram, B. Vermersch, V. Galitski, and P. Zoller, Physical Review X **12**, 011018 (2022), ISSN 2160-3308, arXiv:2106.15530 [cond-mat, physics:hep-th, physics:nlin, physics:quant-ph], URL http://arxiv.org/abs/2106.15530.

[154] R. Fan, P. Zhang, H. Shen, and H. Zhai, Science bulletin **62**, 707 (2017).

[155] B. Sundar, A. Elben, L. K. Joshi, and T. V. Zache, New Journal of Physics **24**, 023037 (2022).

[156] M. R. Geller, A. Arrasmith, Z. Holmes, B. Yan, P. J. Coles, and A. Sornborger, Physical Review E **105**, 035302 (2022).

[157] N. Y. Yao, F. Grusdt, B. Swingle, M. D. Lukin, D. M. Stamper-Kurn, J. E. Moore, and E. A. Demler, arXiv preprint arXiv:1607.01801 (2016).

[158] M. K. Joshi, A. Elben, B. Vermersch, T. Brydges, C. Maier, P. Zoller, R. Blatt, and C. F. Roos, Physical Review Letters **124**, 240505 (2020).

[159] B. Swingle, G. Bentsen, M. Schleier-Smith, and P. Hayden, Physical Review A **94**, 040302 (2016).

[160] N. Y. Halpern, Physical Review A **95**, 012120 (2017).

[161] J. Dressel, J. R. González Alonso, M. Waegell, and N. Yunger Halpern, Phys. Rev. A **98**, 012132 (2018), URL https://link.aps.org/doi/10.1103/PhysRevA.98.012132.

[162] M. K. Joshi, A. Elben, B. Vermersch, T. Brydges, C. Maier, P. Zoller, R. Blatt, and C. F. Roos, Physical Review Letters **124**, 240505 (2020), ISSN 0031-9007, 1079-7114, URL https://link.aps.org/doi/10.1103/PhysRevLett.124.240505.

[163] B. Vermersch, A. Elben, L. M. Sieberer, N. Y. Yao, and P. Zoller, Physical Review X **9**, 021061 (2019).

[164] F. Mezzadri, arXiv preprint math-ph/0609050 (2006).

[165] E. Gustafson, Y. Zhu, P. Dreher, N. M. Linke, and Y. Meurice, Phys. Rev. D **104**, 054507 (2021), 2103.06848.

[166] E. Gustafson, P. Dreher, Z. Hang, and Y. Meurice, Quantum Sci. Technol. **6**, 045020 (2021).

[167] T. Takayanagi, Phys. Rev. Lett. **107**, 101602 (2011), 1105.5165.

[168] M. Fujita, T. Takayanagi, and E. Tonni, JHEP **11**, 043 (2011), 1108.5152.

[169] P. Dey and A. Söderberg, JHEP **07**, 013 (2021), 2012.11344.

[170] X. Chen, T. Zhou, and C. Xu, Journal of Statistical Mechanics: Theory and Experiment **2018**, 073101 (2018).

Goksu Can Toga

gctoga@syr.edu

Experience

- **Syracuse University, Physics Department** 2018 – Present
  Graduate Research Assistant *Syracuse, NY*
  - Participated in the development of quantum simulations of multiple physical models using both universal and analog quantum computers and benchmarked these multiple quantum platforms and error-correction techniques.
  - Created classical counterparts for quantum simulations using Tensor Networks to validate quantum results.
  - Contributed to the simulations of supersymmetric Yang-Mills models and strongly coupled fermionic models using Hybrid Monte Carlo techniques. Developed and modified the needed HMC codes in C/C++ and conducted data analysis using Python.
  - Worked as a Teaching Assistant for various courses, assisting with laboratory courses and grading exams. Received the Outstanding Teaching Assistant Award during my employment as a TA.
- **Gazi University, Physics Department** 2016 – 2018
  Graduate Teaching Assistant *Ankara, Turkey*
  - Led laboratory courses, including Electronics Lab and Introductory Physics Lab.

Education

- **Syracuse University** Syracuse, NY
  PhD in Physics *2018 – 2024*
- **Middle East Technical University** Ankara, Turkey
  MSc in Physics *2015 – 2018*
- **Middle East Technical University** Ankara, Turkey
  BSc in Physics *2011 –2015*

Publications

- Simulating Field Theories with Quantum Computers, M. Assaduzamman, S. Catterall, Y. Meurice, & G. C. Toga, (2024) e-Print arXiv:2401.01962
- Tensor network representation of non-abelian gauge theory coupled to reduced staggered fermions, M. Assaduzamman, S. Catterall, Y. Meurice, R. Sakai & G. C. Toga, (2023) e-Print arXiv:2312.16167
- Quantum Ising model on two dimensional anti-de Sitter space, M. Assaduzamman, S. Catterall, Y. Meurice, & G. C. Toga, (2023) e-Print arXiv:2309.04383
- Holography from lattice $\mathcal{N} = 4$ super Yang-Mills, M. Assaduzamman, S. Catterall, Y. Meurice, & G. C. Toga, JHEP **08**, 084 (2023), e-Print arXiv:2303.16025
- Improved coarse-graining methods on two dimensional tensor networks including fermions, M. Assaduzamman, S. Catterall, Y. Meurice, R. Sakai & G. C. Toga, JHEP **01** (2023), 024 e-Print arXiv:2210.03834
- Quantum Simulation of N-flavor Gross-Neveu Model, M. Assaduzamman, S. Catterall, Y. Meurice, R. Sakai & G. C. Toga, Phys. Rev. D **106** (2022) no.11, 114515 e-Print arXiv:2208.05906

- Symmetric Mass Generation in Lattice Gauge Theory, N.Butt, S. Catterall & G.C.Toga, Symmetry **13** (2021) no.12, 2276 e-Print arXiv:2111.01001
- Anomalies and symmetric mass generation for Kähler-Dirac fermions, S. Catterall, A. Pradhan, G. C. Toga, & N. Butt, Phys. Rev. D **104** (2021) no.9, 094504 e-Print arXiv:2101.01026
- Lattice $\mathcal{N}=4$ super Yang-Mills at strong coupling, S. Catterall, J. Giedt, & G. C. Toga JHEP **12** (2020), 140 e-Print arXiv:2009.07334
- Chaos from Equivariant Fields on Fuzzy S_4, Ü. Coşkun, S. Kürkcüoğlu, G.C. Toga, &G. Ünal, JHEP **12** (2018), 015 e-Print arXiv:1806.10524
- Quantum Hall effect on Odd spheres, Ü Coşkun, S. Kürkcüoğlu & G. C. Toga, Phys. Rev. D **95** (2017) no.6, 065021 e-Print arXiv:1612.03855

Presentations

- Quantum & Classical simulations of AdS_2 Ising Model, Boston University HEP Seminar, December 2023
- Holography from lattice $N = 4$ SYM, HU/DESY joint lattice seminar, November 2023
- Simulating Hyperbolic Ising Model, Lattice 2023, August 2023, Fermilab
- Fast Scrambling in Hyperbolic Ising Model, Tensor Networks in Many Body and Quantum Field Theory INT Workshop, April 2023, INT
- Towards Quantum Simulation of Hyperbolic Ising Model, QuLat Meeting, March 2023, online
- $N = 4$ Super Yang-Mills Model on Lattice, Cornell-Syracuse HEP Theory Meeting, November 2022, Syracuse
- Extracting Non-Abelian Coulomb Potential from $N = 4, SU(3)$ SYM Model, Lattice 2022, University of Bonn
- DMRG Construction of N flavor Gross-Neveu Model, QuLat Colloboration Meeting, July 2022, University of Iowa
- N=4 Lattice Super Yang Mills at Strong Coupling, Lattice 2021, MIT
- Quantum Hall Effect on Odd Spheres, 2017, Gazi University

Honors and Awards

- Syracuse University Graduate Fellowship (2023)
- Syracuse University Outstanding Teaching Assitant Award (2021)
- Syracuse University College of Arts and Sciences Summer Fellowship (2019)
- Syracuse University Henry Levinstein Fellowship (2018 & 2019)

Programming Skills

Languages:Python,Julia, C/C++, ITensor, Qiskit, bash,LaTeX

References

Prof. Simon Catterall, Prof. Yannick Meurice